# Robust Finite Element Implementation of Damage-based Cohesive Zone Models: Application to Composite Delamination and Hydrofracturing of Glaciers

By

Gourab Ghosh

Dissertation
Submitted to the Faculty of the
Graduate School of Vanderbilt University
in partial fulfillment of the requirements
for the degree of

DOCTOR OF PHILOSOPHY
in
Civil Engineering

May 14, 2021

Nashville, Tennessee

Approved:

Ravindra Duddu, Ph.D.
Chandrasekhar Annavarapu, Ph.D.
Caglar Oskay, Ph.D.
Prodyot K. Basu, Ph.D.
Haoxiang Luo, Ph.D.

*To My Ma (Mom) and Baba (Dad)*

# ACKNOWLEDGMENTS

I want to acknowledge and express my gratitude to a group of people who made a significant contribution in shaping my dream, although words will fall short to do so.

First and foremost, I would like to express my gratitude to my advisor Prof. Ravindra Duddu, for motivating and enlightening me in the journey of being a researcher. His guidance and enthusiasm throughout my Ph.D. pushed me to improve and expand my scientific knowledge. I feel fortunate for the opportunities he has provided me and for the many hours he spent providing feedback and answering my questions. I am eternally grateful for his encouragement and patience.

I am privileged to have worked closely with Prof. Chandrasekhar Annavarapu. I would like to thank him for co-advising me and sharing his knowledge on the stabilized Nitsche-based method which is a significant part of my dissertation. I would like to thank Prof. Caglar Oskay for providing me excellent suggestions on my work. I have enjoyed discussing and getting critical opinion from him during the weekly group meetings. Prof. P.K. Basu, has been always approachable for advice on both academic and non-academic matters. He has been encouraging and supportive throughout my stay at Vanderbilt University. I would like to thank Prof. Haoxiang Luo, for agreeing to serve as my committee member. I wish to extend my thanks to all the Professors at Vanderbilt University who have helped me gain a wealth of knowledge through their lectures.

The most suitable place for someone's work is the place where he/she can deliver his/her best. I have also been fortunate to work with some great colleagues. I would like to express my special thanks to Dr. Stephen Jiménez who has helped me to get started with the cohesive zone modeling. Throughout my journey as a Ph.D. student at Vanderbilt University, Dr. Xiangming Sun has been a great colleague and friend of mine. I wish to thank him for his help and support, whenever I needed it. I would also like to extend my thanks to Dr. Pranav Karve and Mr. Yuxiang Gao. I would like to thank Baig, Paromita Di, Kyle, Xiaoyu, Zhangxing, Ruize and other fellow graduate students at Vanderbilt University for making my stay here enjoyable. I am also grateful to the staff of Civil and Environmental Engineering department, Jackie, Karen, Beverly, and Charity for helping me with numerous things over the years.

On a personal level, I have met some amazing friends in Nashville, whose friendship I will cherish for the rest of my life. The weekend rendezvous with Deepayan, Purboday, Souhrid, Avishek, Rudra Da, Soumita Di, Karuna, Sandeep and many others made Nashville my home away from home. I also would like to thank my high school friends Anurup, Prithwiraj, Sayan, Bivas, who are part of my extended family. I am grateful to Prof. Shyamali Mukherjee for how she cared for me with great love and affection.

Once I read somewhere that, it is not possible for God to take care of each and every person always, that is why he created Parents to substitute him. As I am getting older, I am realizing how true that concept is. I am at a position to write this dissertation only because of their unequalled sacrifices, unconditional love and moral supports. I am greatly indebted to my younger brother for his support, encouragement, and for giving me the opportunity of realizing the duties of an elder brother. I would like to specially thank my fiancée Sampa for her love and continuous emotional support throughout this journey. Lastly, I am grateful to the Almighty for providing me strength in tough times and overcome difficulties to achieve my dreams.

# TABLE OF CONTENTS

# LIST OF TABLES

## LIST OF FIGURES

# Chapter 1

# INTRODUCTION

The purpose of this dissertation is to develop robust cohesive zone modeling approaches based on continuum damage mechanics to simulate mixed-mode fracture or delamination at anisotropic and/or dissimilar material interfaces in fiber-reinforced laminated composites, and hydrofracture in glaciers. In this work, a damage mechanics-based cohesive zone model has been implemented within the finite element framework, modified to include a stabilized Nitsche-based approach, and a poro-damage based augmented hydrofracture model.

Damage mechanics is the study of fracture initiation and propagation in materials undergoing mechanical loading. The fundamental concept is to characterize the presence of microscopic defects, such as micro-cracks or micro-voids, within the macroscopic material behavior. Consider, for example, a distribution of micro-voids within a material volume; during loading the voids can gradually grow in size, thus weakening the material until they coalesce into a macro-crack. From this perspective, damage is physically interpreted as the ratio of the area of micro-defects to the total area of material along its principal planes, that is, cross-sectional cuts of the material normal to each principal direction [6]. If the size scale of damage zone with respect to the system is small, the damage front can be represented as a sharp interface with zero thickness. The cohesive zone model (CZM), projects damage onto a sharp interface, and so damage is characterized as an area representing micro-cracks across the interface. In the CZM framework, the state of damaged or degraded material is generally characterized using a damage tensor $\mathbf{D}_s$, however in the simplified case of isotropic damage, a scalar variable $\mathrm{D}_s$ sufficiently describes the damaged material state. Thus, for undamaged material $\mathrm{D}_s = 0$, whereas for a fully damaged material $\mathrm{D}_s = 1$. Partially damaged material (i.e., where $0 < \mathrm{D}_s < 1$) becomes more stressed and compliant, which is accounted by the principle of effective stress [7, 8], and the hypothesis of strain equivalence [9] or energy equivalence [10]. In practice, damage-induced compliance is incorporated into a material's constitutive behavior by reducing the stiffness or viscosity with the factor (1-$D_s$). This implementation of damage is appropriate for modeling fracture evolution in sharp interfaces, which is demonstrated through the work presented in this dissertation.

Numerical simulation of fracture propagation in multi-dimensions is a challenging problem, in part due to mixed-mode interactions and stiff anisotropic cohesive response at arbitrarily shaped crack interfaces, particularly under compression. The cohesive zone modeling approach has been widely used to analyze and predict mixed-mode fracture or delamination propagation at anisotropic and/or dissimilar material interfaces, despite its limitations. Typically, cohesive zone models (CZMs) are implemented in conjunction with the finite element method by introducing zero-thickness interface elements along potential crack surfaces. The constitutive behavior of the interface is defined by a cohesive law that relates the traction with the separation across the crack surface. In general, there are two classes of cohesive laws, namely intrinsic or initially elastic cohesive laws, and extrinsic or initially rigid cohesive laws. On the one hand, the extrinsic cohesive zone models consistently describe fracture initiation, but are difficult to implement in a legacy finite element software (e.g., [11]). On the other hand, intrinsic CZMs are fairly straightforward to incorporate in a legacy finite element framework, but are plagued by numerical issues. Specifically, when using "stiff" cohesive laws or an anisotropic CZM (i.e., different normal and tangential cohesive stiffness), intrinsic CZMs suffer from ill-conditioned discrete systems that result in poor convergence and spurious oscillations in interfacial tractions [12, 13, 14]. It bears emphasis that these issues can also arise with extrinsic CZMs when analyzing stiff behavior under compressive loading or low-cycle fatigue loading, when the unloaded and reloaded in the early stages of the softening regime of the traction-separation law [15].

The first objective of this dissertation is to address these numerical problems by introducing a robust, stabilized formulation for treating cohesive laws with arbitrarily large stiffness within the finite element method. To this end, A stabilized formulation is proposed that generalizes Nitsche's method [16] for cohesive fracture problems. Nitsche's method can be viewed as a variationally consistent penalty method, with the advantage that the discrete system of equations are better conditioned provided the stabilization parameters are chosen appropriately. As a result of the pioneering work of [17], the method has become popular for a wide class of interface (contact) problems [18, 19, 20]. The proposed formulation is a novel extension of the formulation presented in [21] to fracture mechanics problems. It enables the implementation of extrinsic CZMs with the finite element framework of intrinsic CZMs.

The second objective of this dissertation is to demonstrate the robustness of the stabilized finite element method proposed by Ghosh *et al.* [22] for modeling delamination growth in laminated fiber-reinforced composite materials with transversely isotropic elastic behavior, which are widely used in the aerospace/automobile industry. To this end, the parametric uncertainties, numerical instability, mesh dependence, and computational efficiency issues associated with the commonly used standard finite element method for cohesive fracture/delamination is investigated. The advantages of using the stabilized method that address the issues with the standard method in the context of delamination analysis is illustrated. While the stabilized finite element method for cohesive fracture/delamination problems was fully developed in Ghosh *et al.* [22], it was tested only for isotropic linearly elastic media using simplified patch tests and benchmark problems to verify accuracy and illustrate convergence. Mode-I, mode-II, and mixed-mode crack growth in laminated cross-ply composites is simulated by choosing standardized test configurations and validated the results with experimental data, when available to achieve the second objective. Furthermore, the stability and accuracy of standard and stabilized methods with semi-structured or perturbed meshes for delamination analysis is explored.

The third objective of this dissertation is to develop a robust CZM approach for modeling hydrofracture and crevasse propagation in glaciers. The plausibility of rapid global sea-level rise predominantly due to mass loss from glaciers and ice sheets due to hydrofracturing of ice shelves and marine ice cliff instability highlights the urgent need for modeling and understanding fracture/failure mechanisms in glaciers. However, the fracture mechanisms associated with crevasse initiation and propagation, are complex and involve mechanical, thermal and hydraulic fracture processes [23, 24, 25, 26]. For instance, when melt-water infiltrates the surface crevasses or seawater infiltrates the basal crevasses, crevasse can propagate deeper into the glacier; this hydraulic-pressure-driven fracture is commonly referred to as hydro-fracture [27]. To simulate hydrofracturing of glacier crevasses, a poro-damage-based approach that accounts for the effect of hydrostatic water pressure inside the damaged ice by integrating principles of continuum damage mechanics and poro-mechanics is developed. In the proposed formulation, damage is interpreted to represent the ratio of isotropic void area to total area along the cohesive interface, assuming water can permeate the damaged material and exert hydrostatic pressure along the interface.

# Chapter 2

# A STABILIZED FINITE ELEMENT METHOD FOR ENFORCING STIFF ANISOTROPIC COHESIVE LAWS USING INTERFACE ELEMENTS

This chapter is adapted from "A stabilized finite element method for enforcing stiff anisotropic cohesive laws using interface elements" published in *Computer Methods in Applied Mechanics and Engineering* and has been reproduced with the permission of the publisher and my co-authors Ravindra Duddu and Chandrasekhar Annavarapu : Ghosh, G., Duddu, R., and Annavarapu, C. (2019). A stabilized finite element method for enforcing stiff anisotropic cohesive laws using interface elements, *Computer Methods in Applied Mechanics and Engineering*, 348: 1013-1038

## 2.1 Introduction

Numerical simulation of fracture propagation in multi-dimensions is a challenging problem, in part due to mixed-mode interactions and stiff anisotropic cohesive response at arbitrarily shaped crack interfaces, particularly under compression. The cohesive zone modeling approach has been widely used to analyze and predict mixed-mode fracture or delamination propagation at anisotropic and/or dissimilar material interfaces, despite its limitations. Typically, cohesive zone models (CZMs) are implemented in conjunction with the finite element method by introducing zero-thickness interface elements along potential crack surfaces. The constitutive behavior of the interface is defined by a cohesive law that relates the traction with the separation across the crack surface. There are broadly two classes of CZMs: intrinsic with initially elastic cohesive laws and extrinsic with initially rigid cohesive laws. Cohesive laws with large initial stiffness may be required for accurate fracture analysis and contact enforcement in the intrinsic approach; however, stiff cohesive laws may also need to be enforced during cycle-by-cycle fatigue analysis even in the extrinsic approach (see Fig. 1). It is well-known that the standard (penalty-like) method for enforcing stiff cohesive laws using interface elements suffers from a distinct numerical instability that is often manifested by spurious oscillations in crack-face tractions, which may cause inaccuracies and convergence issues. The purpose of this paper is to introduce a novel stabilized finite element method by generalizing Nitsche's method for enforcing stiff anisotropic cohesive laws that alleviates the numerical instability issue afflicting the standard method.

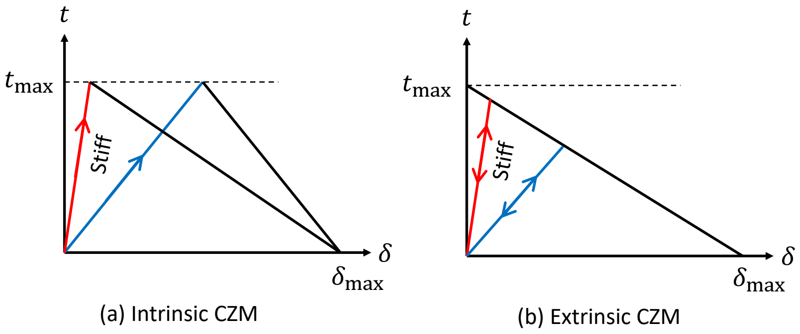

Figure 2.1: Illustration of stiff (red line) cohesive laws encountered in fracture analysis under monotonic and cyclic loading. (a) In intrinsic CZMs, stiff cohesive laws may be prescribed to define the linear elastic portion before damage initiation or no-interpenetration (contact) condition; (b) In extrinsic CZMs, stiff cohesive laws may be encountered during unloading/reloading immediately after damage initiation or contact enforcement during cyclic loading.

In an extrinsic CZM, it is assumed that the interface separates only after the cohesive traction exceeds a finite cohesive strength and then the maximum cohesive traction decreases monotonically with the increase in separation until an ultimate separation value is reached (see Fig. 2.1b). Since their introduction in the seminal paper by Camacho and Ortiz [28], the extrinsic CZM approach have been used to simulate dynamic fracture in a wide-range of engineering materials [e.g., 29, 30, 31, 32, 33, 34]. In practice, the extrinsic approach is implemented by adaptively inserting zero-thickness interface elements in a finite element mesh adjacent to the crack tip when a specified criterion for the onset of failure is met. Consequently, the numerical implementation of extrinsic CZMs is computationally efficient, but it requires sophisticated topology change algorithms to modify the associated finite element data structures consistently with the evolving fracture geometry, which increases algorithmic complexity. Despite several algorithmic advances [35, 36, 37, 38], numerical implementation of extrinsic CZMs in a legacy finite element framework remains non-trivial, compared to intrinsic CZMs that are much more straightforward to implement.

In intrinsic CZMs, it is assumed that the cohesive traction increases gradually with separation till it reaches a finite cohesive strength in the linear elastic regime, and then it decreases monotonically till the separation reaches an ultimate value, where complete decohesion occurs (see Fig. 2.1a). Xu and Needleman [39] pioneered the intrinsic approach using a potential-based traction-separation law to model dynamic fracture growth in brittle solids. Several phenomenological and potential-based intrinsic CZMs with bilinear [40], trapezoidal [41, 42], and polynomial shapes [43, 44] have been developed for specific applications. In practice, the intrinsic approach is implemented by inserting zero-thickness interface elements in a finite element mesh along all potential crack paths *a priori*. This approach has been extensively used to model both quasi-static and dynamic failure in a variety of applications including particle-matrix interface debonding in metal-based composites [45], delamination in laminated composite materials [46, 47, 48], and fiber-metal laminate failure [49]. The intrinsic approach is relatively straightforward to implement in a legacy finite element framework, but it has some shortcomings, including the well-known "artifical complicance" [13, 50] and increased computational cost.

Despite their differences, the implementation of both extrinsic and intrinsic approaches for stiff cohesive laws using the standard (penalty-like) method is prone to several numerical issues during dynamic and quasi-static fracture analysis. The stiffness of the cohesive law is often defined using a non-dimensional quantity $M = \alpha^0 h/E$, where $\alpha^0$ is the initial cohesive stiffness, $E$ is the elastic modulus and $h$ is the mesh size parameter [51]. For laminated composites, Turon et al. [52] suggested using the sub-laminate thickness $t$, instead of mesh size parameter $h$, to define the non-dimensional quantity $M$. For a given size-scale parameter (i.e., $h$ or $t$), choosing a large cohesive stiffness $\alpha^0$ relative to the elastic modulus $E$ leads to a stiff cohesive law with $M > 1000$. In dynamic fracture analysis, to avoid the artificial compliance issue, it is required to assume an adequately large value for the initial cohesive stiffness in intrinsic CZMs [13, 53, 51], but that can lead to ill-conditioning of the tangent stiffness matrices. This ill-conditioning issue may also arise in extrinsic CZMs under cyclic loading, if the interface is unloaded immediately after crack initiation when the elastic unloading/reloading slope could be large [28]. This issue can be resolved to some extent by restricting the time step in an explicit finite element scheme to an extremely small value [50, 31], but this will result in an impractically high computation cost. In quasi-static fracture analysis, intrinsic CZMs exhibit spurious traction oscillations along the cohesive interface, especially near crack tips, if a large initial cohesive stiffness is specified [54, 12, 55, 52], or if the cohesive interface has a curved geometry and its behavior under compressive loading is described by an anisotropic cohesive law with different values for normal and tangential stiffness [14]. It has been argued in [14] that the issue of spurious traction oscillations encountered in the standard (penalty-like) method for intrinsic CZMs with stiff cohesive laws (using full or reduced integration) arises due to the violation of the inf-sup or LBB condition.

In the traditional penalty method [56], a Dirichlet constraint at the interface is enforced by introducing a spring-like tie constraint at the interface. A better approximation of the Dirichlet constraint can be obtained by using a large value for the penalty parameter, which can be interpreted as the stiffness of the spring (i.e., initial slope of the traction separation law). Thus, the standard finite element method for implementing an intrinsic CZM is equivalent to the penalty method for stiff cohesive laws. Theoretically, the interfacial constraint of zero separation before crack initiation (i.e., extrinsic CZM) can be achieved if the initial cohesive stiffness approaches infinity, but using a very large cohesive stiffness leads to ill-conditioning and numerical instability issues. Lagrange-multiplier-based mixed formulations can alleviate instability issues associated with cohesive interface elements [57, 58] or with embedded contact interfaces in the extended finite element method (XFEM) [59, 60]. However, these approaches can be computationally costly and complicated to implement, because it is difficult and non-trivial to find a stable Lagrange multiplier space that alleviates traction oscillations [61]. Another alternative is Nitsche's method, which was originally introduced in [16] to weakly enforce Dirichlet boundary conditions. Later, it was extended to weakly enforce the continuity of the displacement field at the interior boundaries [62]. We note that the discontinuous Galerkin (DG) method essentially originated from Nitsche's method [11] and the latter has been referred to as the classical DG method [63]. A comprehensive review of Nitsche's method and its application to interface problems can be found in [64, 65].

The Nitsche's method can be interpreted as a variationally consistent penalty method for weakly enforcing interfacial constraints. This method can eliminate the instability issues associated with the penalty method by adding consistency terms [66, 67], and can yield oscillation-free traction profiles at embedded interfaces [18]. In the recent decades, Nitsche's method has been utilized for solving a wide range of interface problems in an efficient way [68, 69, 70, 71, 72, 73, 18, 74, 75, 76]. More recently, Nitsche-based methods have been developed for frictional-sliding on embedded interfaces [19, 77] and small-sliding contact on frictional surfaces, including stick-slip behavior [20]. In this chapter, we propose a stabilized finite element method for cohesive fracture problems, which is inspired by the Nitsche's method for general boundary conditions developed by Juntunen and Stenberg [78]. The proposed method ensures accurate recovery of crack-surface traction even for large values of cohesive stiffness (e.g., 8–16 orders of magnitude more than bulk stiffness). We further demonstrate the ability of the stabilized method to alleviate numerical instability associated with the implementation of stiff, anisotropic cohesive laws with different interface properties in the normal and tangential directions. The main novelty of this work is that it extends Nitsche's method for cohesive fracture so that it is applicable to both intrinsic and extrinsic approaches, including stiff elastic loading and unloading conditions. The rest of this chapter is organized as follows: in Section 2.2, we introduce the governing equations of the cohesive fracture problem and the weak forms corresponding to the standard and stabilized methods; in Section 2.3, we discuss the numerical implementation of the stabilized method in the commercial finite element software ABAQUS; in Section 2.4, we present several numerical examples to compare the standard and stabilized methods with a particular emphasis on the accuracy of evaluating crack-face tractions for stiff cohesive laws in quasi-static simulation, including mixed-mode fracture; in Section 2.5, we conclude with a summary and closing remarks.

## 2.2 Model Formulation

In this section, we present details of the stabilized finite element method for enforcing stiff cohesive laws. We first present the strong form of the governing equations followed by a brief description of the interface cohesive law for mixed-mode loading. We next derive the weak form for the standard (penalty-like) and stabilized (Nitsche-inspired) methods.

### 2.2.1 Strong Form

We consider the initial domain $\Omega \subset \mathbb{R}^{nd}$ containing a linearly elastic solid with $nd = 2$ in two dimensions, as shown in Fig. 2.2. The domain boundary $\Gamma \equiv \partial\Omega$ is partitioned into two disjoint parts such that $\partial\Omega = \Gamma_D \cup \Gamma_N$ with $\Gamma_D \cap \Gamma_N = \emptyset$, where the Dirichlet and Neumann boundary conditions are enforced. The domain $\Omega$ contains an internal cohesive interface $\Gamma_*$, which divides $\Omega$ into two non-overlapping sub-domains $\Omega^1$ and $\Omega^2$. The outward unit normal to the boundary $\partial\Omega$ is denoted by $\mathbf{n}_\mathrm{e}$, and the unit normal vector associated with the interface $\Gamma_*$ denoted by $\mathbf{n}$ points from $\Omega^2$ to $\Omega^1$. We use a rectangular Cartesian coordinate system and the total Lagrangian description for variables with $\mathbf{X}$ denoting the position of the material points. The displacement field $\mathbf{u}(\mathbf{X})$ is discontinuous across $\Gamma_*$, but continuous in $\Omega^1$ and $\Omega^2$; therefore, it can be represented by two continuous functions $\mathbf{u}^1(\mathbf{X})$ and $\mathbf{u}^2(\mathbf{X})$ in the respective sub-domains. For brevity, henceforth we will suppress the spatial dependence of variables. Assuming small displacements, the Cauchy stress tensor can be defined in $\Omega^1$ and $\Omega^2$ as

$$\boldsymbol{\sigma}^m = \mathbf{D}^m : \boldsymbol{\epsilon}^m, \quad m = \{1,2\}, \tag{2.1}$$

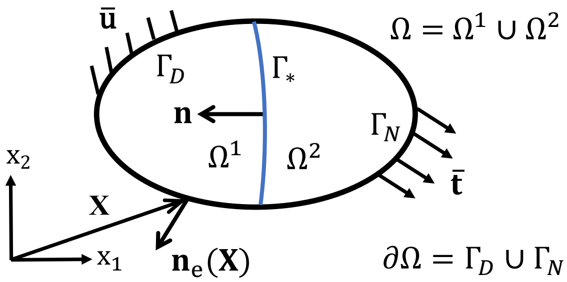

Figure 2.2: A schematic of the domain for the quasi-static cohesive fracture problem.

where $\mathbf{D}$ denotes the fourth-order elasticity tensor and the small strain tensor $\boldsymbol{\epsilon} = \frac{1}{2}(\boldsymbol{\nabla}\mathbf{u} + (\boldsymbol{\nabla}\mathbf{u})^T)$ is defined by the symmetric part of the displacement gradient tensor and $\boldsymbol{\nabla}$ is the spatial gradient operator with respect to the material coordinates $\mathbf{X}$. The strong form of the quasi-static boundary value problem in the absence of body force is:

$$\boldsymbol{\nabla} \cdot \boldsymbol{\sigma}^m = \mathbf{0} \text{ in } \Omega^m, \quad m = \{1,2\}, \tag{2.2}$$

$$\mathbf{u} = \bar{\mathbf{u}} \text{ on } \Gamma_D, \tag{2.3}$$

$$\boldsymbol{\sigma} \cdot \mathbf{n}_\mathrm{e} = \bar{\mathbf{t}} \text{ on } \Gamma_N, \tag{2.4}$$

$$\mathbf{t}_\mathrm{c}(\boldsymbol{\delta}) = \boldsymbol{\sigma} \cdot \mathbf{n}, \text{ on } \Gamma_*, \tag{2.5}$$

where $\bar{\mathbf{t}}$ is the prescribed traction or stress vector on the Neumann boundary $\Gamma_N$, $\bar{\mathbf{u}}$ is the prescribed displacement vector on the Dirichlet boundary $\Gamma_D$, and the traction on the cohesive interface $\mathbf{t}_\mathrm{c}$ is given by a function of the interface separation or displacement jump as

$$\boldsymbol{\delta} = [\![\mathbf{u}]\!] = \mathbf{u}^2 - \mathbf{u}^1 \tag{2.6}$$

Note that the traction $\mathbf{t}_\mathrm{c}$ is continuous across the cohesive interface $\Gamma_*$ and is related to the Cauchy stress tensor evaluated in the sub-domains $\Omega^1$ and $\Omega^2$ as

$$\mathbf{t}_c = \boldsymbol{\sigma} \cdot \mathbf{n} = -\boldsymbol{\sigma}^1 \cdot \mathbf{n}^1 = \boldsymbol{\sigma}^2 \cdot \mathbf{n}^2. \tag{2.7}$$

In the above two equations, we followed the notation convention used in [73] for defining the displacement jump and outward normal, and use it to establish the weak form in Section 2.2.3.

### 2.2.2 Intrinsic cohesive law

For simplicity, we consider the bilinear intrinsic cohesive law with an initial (increasing) linear elastic portion followed by a (decreasing) linear softening response. The corresponding relation between crack-face traction and interface separation can be defined using the damage mechanics framework as [47, 48, 79]

$$\mathbf{t}_{\mathrm{c}} = -\,\boldsymbol{\alpha}\,\boldsymbol{\delta}, \tag{2.8}$$

where $\boldsymbol{\alpha}$ is the cohesive stiffness matrix including the effect of damage. Note that the crack-face traction $\mathbf{t}_{\mathrm{c}}$ is the Newton's third law pair to the cohesive traction. Thus, the negative sign in the above equation indicates that $\mathbf{t}_{\mathrm{c}}$ causes a restoring force at the interface, which is equal and opposite to the deforming force. To represent the mixed mode-I and mode-II fracture behavior in two dimensions, we use the normal and tangential coordinate system. Accordingly, the tangential $t_\tau$ and normal $t_n$ components of the traction vector $\mathbf{t}_{\mathrm{c}}$ are related to the tangential $\delta_\tau$ and normal $\delta_n$ components of the interface separation $\boldsymbol{\delta}$ as

$$\begin{Bmatrix} t_\tau \\ t_n \end{Bmatrix} = -\begin{bmatrix} (1-D_s)\alpha_\tau^0 & 0 \\ 0 & (1-D_s)\alpha_n^0 \end{bmatrix} \begin{Bmatrix} \delta_\tau \\ \delta_n \end{Bmatrix}, \tag{2.9}$$

where $\alpha_n^0$ and $\alpha_\tau^0$ represent the initial cohesive stiffness in the normal and the tangential directions, respectively. The scalar damage variable $D_s$ describing interface degradation under quasi-static mixed-mode loading in two dimensions is given by

$$D_s = \begin{cases} 0 & \text{if} \quad \delta_e < \delta_e^c, \\ \dfrac{\delta_e^u(\delta_e - \delta_e^c)}{\delta_e(\delta_e^u - \delta_e^c)} & \text{if} \quad \delta_e^c \leq \delta_e < \delta_e^u, \\ 1 & \text{if} \quad \delta_e^u \leq \delta_e, \end{cases} \tag{2.10}$$

where $\delta_e = \sqrt{\delta_n^2 + \delta_\tau^2}$ is the equivalent separation, $\delta_e^c$ and $\delta_e^u$ are interface parameters corresponding to critical and ultimate separations, respectively, defined as [5]

$$\frac{1}{\delta_e^c} = \sqrt{\left(\frac{\alpha_n^0 \cos I}{\sigma_{\max}}\right)^2 + \left(\frac{\alpha_\tau^0 \cos II}{\tau_{\max}}\right)^2} \tag{2.11}$$

$$\frac{1}{\delta_e^u} = \left(\frac{\alpha_n^0 \delta_e^c (\cos I)^2}{2\, G_{IC}}\right) + \left(\frac{\alpha_\tau^0 \delta_e^c (\cos II)^2}{2\, G_{IIC}}\right) \tag{2.12}$$

where the direction cosines $\cos I = \delta_n/\delta_e$ and $\cos II = \delta_\tau/\delta_e$, $\sigma_{\max}$ and $\tau_{\max}$ are the pure mode I and mode II cohesive strengths, and $G_{IC}$ and $G_{IIC}$ are the pure mode I and mode II critical fracture energies (see Fig. 2.3a). For monotonic loading, when the equivalent interface separation $\delta_e$ is less than the critical separation $\delta_e^c$, there is no damage in the cohesive interface elements. After the critical separation is exceeded, damage starts to accumulate till the separation reaches the ultimate value $\delta_e^u$, when the cohesive elements are completely damaged (see Fig. 2.3b). The mixed-mode cohesive law described above was previously proposed by Jiang et al. [5], wherein quadratic damage initiation and mixed-mode failure criteria were used to obtain the equivalent critical and ultimate separations. If the parameter values of cohesive stiffness, cohesive strength and fracture energy are chosen to be the same for both normal and shear modes, then we get an isotropic cohesive law, else we get an anisotropic cohesive law. For non-monotonic (cyclic) loading, we can enforce irreversibility of damage evolution by ensuring that damage does not change during unloading and reloading cycles, until the previous maximum damage is exceeded [80, 79].

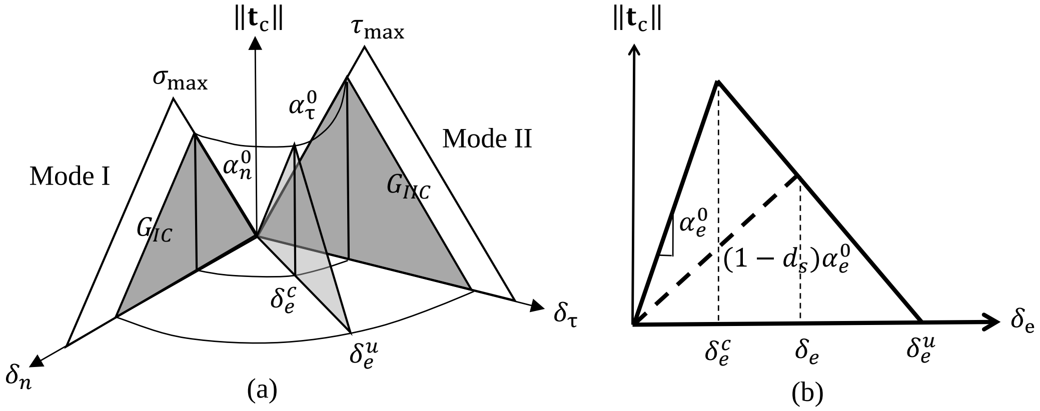

Figure 2.3: A schematic diagram of the mixed-mode bilinear cohesive law (redrawn from [4]): (a) the traction-separation relationship for any arbitrary mode-mix ratio is defined in terms of the pure mode I and mode II relationships; (b) the relationship between the static damage variable $d_s$ and the equivalent separation. The magnitude of the traction vector $\|\mathbf{t}_c\| = \sqrt{t_n^2 + t_\tau^2}$.

### 2.2.3 Weak Form

We follow the Galerkin method of weighted residuals to derive the weak forms corresponding to the standard and stabilized methods. We define the space of trial functions **U** and the space of test functions **W**, such that:

$$\mathbf{U} = \{\mathbf{u} \in H^1(\Omega), \mathbf{u} = \bar{\mathbf{u}} \text{ on } \Gamma_D\}, \tag{2.13}$$

$$\mathbf{W} = \{\mathbf{w} \in H^1(\Omega), \mathbf{w} = \mathbf{0} \text{ on } \Gamma_D\}. \tag{2.14}$$

By weighting Eq. (2.2) with the test function **w**, integrating by parts, applying the divergence theorem, and using the traction continuity condition at the interface in Eq. (2.7), and the constitutive relation in Eq. (3.1), we can derive the weak form as follows:

$$\int_\Omega \nabla^s \mathbf{w} : \mathbf{D} : \nabla^s \mathbf{u} \, d\Omega - \int_{\Gamma_*} (\mathbf{w}^2 \cdot \boldsymbol{\sigma}^2 \cdot \mathbf{n}^2 + \mathbf{w}^1 \cdot \boldsymbol{\sigma}^1 \cdot \mathbf{n}^1) \, d\Gamma - \int_{\Gamma_N} \mathbf{w} \cdot \bar{\mathbf{t}} \, d\Gamma = 0, \tag{2.15}$$

$$\int_\Omega \nabla^s \mathbf{w} : \mathbf{D} : \nabla^s \mathbf{u} \, d\Omega - \int_{\Gamma_*} [\![\mathbf{w}]\!] \cdot \mathbf{t}_c \, d\Gamma = \int_{\Gamma_N} \mathbf{w} \cdot \bar{\mathbf{t}} \, d\Gamma, \tag{2.16}$$

Note that in Eq. (2.15) we considered the integrals on the two sides of the cohesive interface, separately, and in Eq. (2.16) we defined the jump in the test function as $[\![\mathbf{w}]\!] = \mathbf{w}^2 - \mathbf{w}^1$.

#### 2.2.3.1 Standard method

Substituting the traction-separation relation in Eq. (2.8) into the weak form in Eq. (2.16) we get

$$\int_{\Omega} \nabla^{s}\mathbf{w} : \mathbf{D} : \nabla^{s}\mathbf{u} \, \mathrm{d}\Omega + \int_{\Gamma_*} [\![\mathbf{w}]\!] \cdot \, \boldsymbol{\alpha} \, \boldsymbol{\delta} \, \mathrm{d}\Gamma = \int_{\Gamma_N} \mathbf{w} \cdot \bar{\mathbf{t}} \, \mathrm{d}\Gamma. \tag{2.17}$$

Thus, in the standard method the cohesive tractions are enforced as a Neumann boundary condition on the interface. Because the cohesive tractions and separations are defined in the normal and tangential directions, the weak form is implemented as,

$$\int_{\Omega} \nabla^{s}\mathbf{w} : \mathbf{D} : \nabla^{s}\mathbf{u} \, \mathrm{d}\Omega + \int_{\Gamma_*} (1 - D_s) \left( [\![w_n]\!] \alpha_n^0 \delta_n + [\![w_\tau]\!] \alpha_\tau^0 \delta_\tau \right) \, \mathrm{d}\Gamma = \int_{\Gamma_N} \mathbf{w} \cdot \bar{\mathbf{t}} \, \mathrm{d}\Gamma. \tag{2.18}$$

If the initial cohesive stiffness parameters $\alpha_n^0$ and $\alpha_\tau^0$ are taken to be sufficiently large the standard method resembles the penalty method for enforcing displacement continuity across the interface. However, for stiff cohesive laws, that is, if cohesive stiffness is several orders of magnitude greater than the elastic modulus, the standard method becomes ill-conditioned leading to instability and/or convergence issues. In the limiting case where $\alpha_n^0 \to \infty$ and/or $\alpha_\tau^0 \to \infty$, that is, for a non-interpenetration (contact) constraint or an extrinsic cohesive law, the standard method is not well defined. To circumvent the above issues, discontinuous Galerkin or Nitsche-based methods have been proposed in [15, 76, 81, 82, 83] based on the extrinsic approach, wherein the interface is perfectly bonded until a certain stress threshold (i.e., interface separation tends to zero and cohesive stiffness tends to infinity). While in [15] interface bonding prior to separation was enforced using the interior penalty method, in [82] Riemann solutions were used to enforce interface conditions. In the following section, we will present an alternative stabilized finite element method for cohesive fracture that is applicable for the whole range of values cohesive stiffness $\alpha_n, \alpha_\tau > 0$, so that it is applicable to both intrinsic and extrinsic approaches.

#### 2.2.3.2 Stabilized method

The proposed method adopts the approach developed in [78, 73] and generalizes it to cohesive fracture problems. By multiplying both sides of Eq. (2.8) with a stabilization matrix $\mathbf{S}$ we obtain

$$\mathbf{S}\mathbf{t}_{\mathrm{c}} = -\mathbf{S}\,\boldsymbol{\alpha}\,\boldsymbol{\delta}. \tag{2.19}$$

After multiplying the above equation by the weighting function $\mathbf{w}$ and integrating over the cohesive interface $\Gamma_*$ we get

$$\int_{\Gamma_*} [\![\mathbf{w}]\!] \cdot \mathbf{S}\mathbf{t}_{\mathrm{c}}\, \mathrm{d}\Gamma = -\int_{\Gamma_*} [\![\mathbf{w}]\!] \cdot \mathbf{S}\boldsymbol{\alpha}\,\boldsymbol{\delta}\, \mathrm{d}\Gamma. \tag{2.20}$$

By adding the above equation to the weak form in Eq. (2.16), we obtain

$$\int_{\Omega} \nabla^{\mathrm{s}}\mathbf{w} : \mathbf{D} : \nabla^{\mathrm{s}}\mathbf{u}\, \mathrm{d}\Omega - \int_{\Gamma_*} [\![\mathbf{w}]\!] \cdot (\mathbf{I} - \mathbf{S})\mathbf{t}_{\mathrm{c}}\, \mathrm{d}\Gamma + \int_{\Gamma_*} [\![\mathbf{w}]\!] \cdot \mathbf{S}\boldsymbol{\alpha}\,\boldsymbol{\delta}\, \mathrm{d}\Gamma = \int_{\Gamma_N} \mathbf{w} \cdot \bar{\mathbf{t}}\, \mathrm{d}\Gamma, \tag{2.21}$$

where $\mathbf{I}$ is the identity matrix. The interface traction can be defined as

$$\mathbf{t}_{\mathrm{c}} = \langle \boldsymbol{\sigma} \rangle_{\gamma} \cdot \mathbf{n} \;\text{ on }\; \Gamma_*, \tag{2.22}$$

where the weighted average of the stress tensors on both sides of the interface is given by

$$\langle \boldsymbol{\sigma} \rangle_{\gamma} = (\gamma^1 \boldsymbol{\sigma}^1 + \gamma^2 \boldsymbol{\sigma}^2) \;\; \forall \;\; \gamma^1 + \gamma^2 = 1, \;\; \gamma^1 > 0, \;\; \gamma^2 > 0. \tag{2.23}$$

Choosing the weights $\gamma^1 = \gamma^2 = 0.5$, yields the mean of the stress tensors evaluated on both sides of the interface. To complete the formulation, we define the stabilization matrix $\mathbf{S}$ as

$$\mathbf{S} = \begin{bmatrix} \dfrac{\beta_\tau}{\alpha_\tau^0(1-D_s)+\beta_\tau} & 0 \\ 0 & \dfrac{\beta_n}{\alpha_n^0(1-D_s)+\beta_n} \end{bmatrix}, \tag{2.24}$$

where $\beta_\tau, \beta_n$ are the stabilization parameters.

The stabilization parameters $\beta_\tau, \beta_n$ and the weights $\gamma^1, \gamma^2$ play a key role in the numerical performance of the method. This so-called weighted Nitsche method [20] is particularly advantageous for dissimilar material interfaces with large contrast in material properties or for unstructured meshes with significant variations in mesh size. For constant strain triangular (CST) and tetrahedral elements, Annavarapu et al. [18] provided estimates for the stabilization parameters using a local coercivity analysis as given by

$$\beta_n = \beta_\tau = 2\left(\frac{|\mathbf{D}^1|(\gamma^1)^2}{\text{meas}(\Omega^1)} + \frac{|\mathbf{D}^2|(\gamma^2)^2}{\text{meas}(\Omega^2)}\right)\text{meas}(\Gamma_*) \tag{2.25}$$

where $|\mathbf{D}|$ denotes the two-norm of the elasticity tensor, $\text{meas}(\Omega)$ denotes the area of neighboring bulk element in 2D, and $\text{meas}(\Gamma_*)$ is the length of the interface element. With a judicious choice of the weights $\gamma^1, \gamma^2$, the stabilization parameters $\beta_\tau, \beta_n$ scale as $1/h$, where $h \approx \text{meas}(\Gamma_*)$ is the mesh/element size parameter. For all $h \in (0,\infty)$, both the initial cohesive stiffness $\alpha$ and the stabilization parameter $\beta$ scale as $1/h$; thus, the stabilized method provides a well-conditioned discrete system, irrespective of the mesh size, by ensuring that the cohesive stiffness terms and the bulk stiffness terms have the same scaling. For an elaborate discussion on the appropriate choice of weights, we refer the reader to Ref. [18]. Note that, in this study, we used the estimates given in (2.25) to calculate the stabilization parameters for bilinear quadrilateral elements; precise estimates can be derived as in [18], but such analysis is beyond the scope of this paper. Finally, the weak form for the stabilized method can be written as

$$\int_{\Omega} \nabla^{\mathrm{s}}\mathbf{w} : \mathbf{D} : \nabla^{\mathrm{s}}\mathbf{u} \, \mathrm{d}\Omega - \int_{\Gamma_*} [\![\mathbf{w}]\!] \cdot (\mathbf{I} - \mathbf{S}) \, \langle \boldsymbol{\sigma} \rangle_{\gamma} \cdot \mathbf{n} \, \mathrm{d}\Gamma + \int_{\Gamma_*} [\![\mathbf{w}]\!] \cdot \mathbf{S}\boldsymbol{\alpha} \, \boldsymbol{\delta} \, \mathrm{d}\Gamma = \int_{\Gamma_N} \mathbf{w} \cdot \bar{\mathbf{t}} \, \mathrm{d}\Gamma. \tag{2.26}$$

In the above equation, the second and third terms on the left hand side ensure consistency and stability of the proposed method, respectively. The stabilized method presented here is unsymmetric and resembles the incomplete interior penalty method [65, 84]. It can be proved that the displacement solution $\mathbf{u}$ of the strong form equations (2.2) – (2.5) is satisfied by the solution to the weak form equation (2.26), which establishes consistency for any value of cohesive stiffness; the mathematical procedure for proving this is similar to that described in [78, Lemma 2.1]. As $(1-D_s)\alpha_n^0, (1-D_s)\alpha_\tau^0 \to \infty$ (refer to Eq. (2.24)), we recover the Nitsche-based method for frictional contact as [19]

$$\int_{\Omega} \nabla^{\mathrm{s}}\mathbf{w} : \mathbf{D} : \nabla^{\mathrm{s}}\mathbf{u} \, \mathrm{d}\Omega - \int_{\Gamma_*} [\![\mathbf{w}]\!] \cdot \langle \boldsymbol{\sigma} \rangle_{\gamma} \cdot \mathbf{n} \, \mathrm{d}\Gamma + \int_{\Gamma_*} [\![\mathbf{w}]\!] \cdot \left(\beta_\tau [\![u_\tau]\!] + \beta_n [\![u_n]\!]\right) \, \mathrm{d}\Gamma = \int_{\Gamma_N} \mathbf{w} \cdot \bar{\mathbf{t}} \, \mathrm{d}\Gamma. \tag{2.27}$$

As $(1-D_s)\alpha_n^0, (1-D_s)\alpha_\tau^0 \to 0$, we recover the weak form for a traction-free crack surface as

$$\int_{\Omega} \nabla^{\mathrm{s}}\mathbf{w} : \mathbf{D} : \nabla^{\mathrm{s}}\mathbf{u} \, \mathrm{d}\Omega = \int_{\Gamma_N} \delta\mathbf{u} \cdot \bar{\mathbf{t}} \, \mathrm{d}\Gamma. \tag{2.28}$$

Thus, the stabilized method remains well-defined for any arbitrarily values of the cohesive stiffness terms, that is, for $(1-D_s)\alpha_n^0, (1-D_s)\alpha_\tau^0 \in [0, \infty)$. Comparing the weak forms in equations (2.16) and (2.26), we can obtain an alternative definition for crack-surface traction as

$$\mathbf{t}_{\mathrm{c}} = (\mathbf{I} - \mathbf{S}) \, \langle \boldsymbol{\sigma} \rangle_{\gamma} \cdot \mathbf{n} - \mathbf{S}\boldsymbol{\alpha} \, \boldsymbol{\delta}. \tag{2.29}$$

Thus, the key idea of the Nitsche-inspired stabilized method for cohesive fracture is to evaluate the crack surface traction in terms of the weighted average stress in the bulk material across the interface and the traction in the cohesive interface.

## 2.3 Numerical Implementation

In this section, we discuss the finite element approximation using matrix notation along with the expression for the residual and tangent matrices for the bulk and interface elements. We also present algorithms for implementing this stabilized method into the commercial software ABAQUS using user defined subroutines for two-dimensional plane strain analysis.

### 2.3.1 Finite element approximation

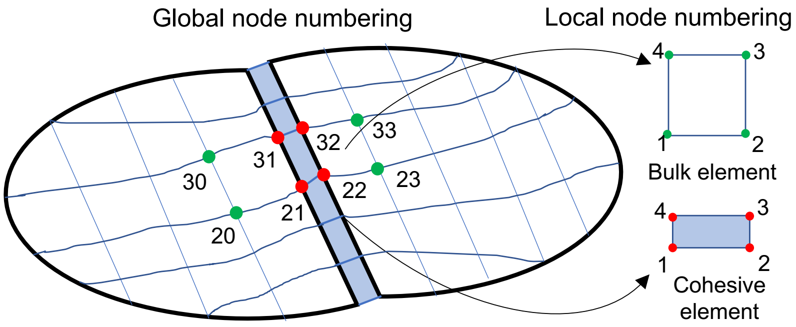

Figure 2.4: Finite element discretization with bulk and zero-thickness cohesive elements

The sub-domains $\Omega^1$ and $\Omega^2$ are discretized by four-noded plane strain quadrilateral bulk elements and zero-thickness four-noded interface elements are introduced at the cohesive interface $\Gamma_*$ (Fig. 2.4). The displacement field $\mathbf{u}^m_{2\times1}$ at any point $\mathbf{X}$ can be approximated as

$$\mathbf{u}^m(\mathbf{X}) = \mathbf{N}(\mathbf{X})\ \bar{\mathbf{u}}^m, \quad m = 1, 2, \tag{2.30}$$

where $\bar{\mathbf{u}}^m = \left[u_1^1, u_2^1, \ldots, u_1^4, u_2^4\right]_{8\times1}$ is the nodal displacement vector for a bulk element in the subdomain $\Omega^m$, $\mathbf{N}$ is the element shape function matrix given by

$$\mathbf{N} = \begin{bmatrix} N^1 & 0 & N^2 & 0 & N^3 & 0 & N^4 & 0 \\ 0 & N^1 & 0 & N^2 & 0 & N^3 & 0 & N^4 \end{bmatrix}_{2\times 8}, \tag{2.31}$$

and $N^J$ $(J = 1,2,3,4)$ are the standard finite element shape functions for the four-noded quadrilateral element. Using Voigt notation, the small-strain strain tensor $\boldsymbol{\epsilon}^m = [\varepsilon_{11}, \varepsilon_{22}, \varepsilon_{12}]^{\mathsf{T}}_{3\times 1}$ in the bulk element can be approximated as

$$\boldsymbol{\epsilon}^m = \mathbf{B}\,\bar{\mathbf{u}}^m, \;\; m = 1,2, \tag{2.32}$$

where the strain-displacement relationship matrix is defined as

$$\mathbf{B} = \begin{bmatrix} N^1_{,1} & 0 & N^2_{,1} & 0 & N^3_{,1} & 0 & N^4_{,1} & 0 \\ 0 & N^1_{,2} & 0 & N^2_{,2} & 0 & N^3_{,2} & 0 & N^4_{,2} \\ N^1_{,2} & N^1_{,1} & N^2_{,2} & N^2_{,1} & N^3_{,2} & N^3_{,1} & N^4_{,2} & N^4_{,1} \end{bmatrix}_{3\times 8}, \tag{2.33}$$

and $N^J_{,i}$ denotes the derivative of the shape function $N^J$ with respect to material coordinate $\mathrm{X}_i$ $(i = 1,2)$ in two dimensions. The normal and tangential components of the displacement jump or separation across the interface element can be approximated as

$$[\![\mathbf{u}]\!]_{2\times 1} = \boldsymbol{\delta}_{2\times 1} = \begin{Bmatrix} \delta_\tau \\ \delta_n \end{Bmatrix} = [\![\mathbf{N}]\!]\hat{\mathbf{u}}, \tag{2.34}$$

where $\hat{\mathbf{u}} = \left[\hat{u}^1_1, \hat{u}^1_2, ..., \hat{u}^4_1, \hat{u}^4_2\right]_{8\times 1}$ is the nodal displacement vector for the four-noded interface element in $\Gamma_*$ and $[\![\hat{\mathbf{N}}]\!]$ is the jump in the interfacial shape function matrix given by [85]

$$[\![\mathbf{N}]\!] = \begin{bmatrix} -C\hat{N}^1 & -S\hat{N}^1 & -C\hat{N}^2 & -S\hat{N}^2 & C\hat{N}^2 & S\hat{N}^2 & C\hat{N}^1 & S\hat{N}^1 \\ S\hat{N}^1 & -C\hat{N}^1 & S\hat{N}^2 & -C\hat{N}^2 & -S\hat{N}^2 & C\hat{N}^2 & -S\hat{N}^1 & C\hat{N}^1 \end{bmatrix}_{2\times 8}, \tag{2.35}$$

and $\hat{N}^J$ ($J = 1,2$) are the standard finite element shape functions for the one-dimensional linear element, and $C$ and $S$ represent the cosine and sine, respectively, of the angle $\theta$ that defines the orientation of the interface element with the global $\mathrm{x}_1$ coordinate axis (see Fig. 2.5). All the finite element shape functions are evaluated using the standard isoparametric concept.

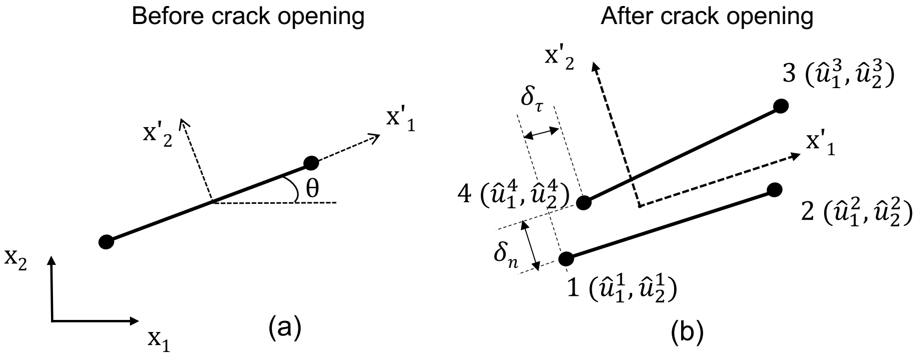

Figure 2.5: Four-noded linear cohesive element: (a) the orientation $\theta$ of the local (normal-tangential) coordinates with respect to the global Cartesian coordinates before crack opening; (b) the relation between nodal displacements in global coordinates and interface separations in local coordinates after crack opening.

### 2.3.2 Discretization and Linearization

By introducing the finite element approximation into the variational form in Eq. (2.26), we write the discretized form of the equilibrium equations as

$$\mathbf{R}(\mathbf{U}) = \mathbf{f}_{\mathrm{ext}} - (\mathbf{f}_{\mathrm{int}}^{\mathrm{b}}(\mathbf{U}) + \mathbf{f}_{\mathrm{int}}^{\mathrm{c}}(\mathbf{U})) = \mathbf{0}, \tag{2.36}$$

where $\mathbf{R}$ is the global residual vector, $\mathbf{U}$ is the global displacement vector, $\mathbf{f}_{\mathrm{ext}}$ and $\mathbf{f}_{\mathrm{int}}^{\mathrm{b}}$ are the global external and internal force vectors, respectively, assembled from all the bulk elements in the domain $\Omega$, and $\mathbf{f}_{\mathrm{int}}^{\mathrm{c}}$ is the internal force vector from all the cohesive elements on the interface $\Gamma_*$. The solution to Eq. (2.36) in the generalized case can be obtained an iterative solution procedure. Let ${}^{k+1}_{j+1}\mathbf{U}$ be the global (nodal) displacement vector at an applied load/displacement step $j+1$ and iteration $k+1$. Using a Taylor's expansion we can linearize the global displacement and the residual vectors as

$$\mathbf{R}\left({}^{k+1}_{j+1}\mathbf{U}\right) = \mathbf{0} = \mathbf{R}\left({}^{k}_{j+1}\mathbf{U} + {}^{k}_{j+1}\Delta\mathbf{U}\right) = \mathbf{R}\left({}^{k}_{j+1}\mathbf{U}\right) + \left[\frac{\partial\mathbf{R}\left({}^{k}_{j+1}\mathbf{U}\right)}{\partial{}^{k}_{j+1}\mathbf{U}}\right]{}^{k}_{j+1}\Delta\mathbf{U}. \tag{2.37}$$

Rewriting the above equation into a fully discretized and linearized system of equation, we obtain

$$ {}^{k}_{j+1}\mathbf{K}\,{}^{k}_{j+1}\Delta\mathbf{U} = \mathbf{R}\left({}^{k}_{j+1}\mathbf{U}\right) \tag{2.38}$$

where $\mathbf{K}$ is the algorithmically consistent tangent matrix obtained by assembling the contributions of the bulk ($\mathbf{K}^{\mathrm{b}}$) and cohesive ($\mathbf{K}^{\mathrm{c}}$) tangent matrices as

$$\mathbf{K} = -\frac{\partial\mathbf{R}}{\partial\mathbf{U}} = \frac{\partial\mathbf{f}^{\mathrm{b}}_{\mathrm{int}}}{\partial\mathbf{U}} + \frac{\partial\mathbf{f}^{\mathrm{c}}_{\mathrm{int}}}{\partial\mathbf{U}} = \mathbf{K}^{\mathrm{b}} + \mathbf{K}^{\mathrm{c}}, \tag{2.39}$$

### 2.3.3 Bulk elements

The internal bulk force vector $\mathbf{f}^{\mathrm{b}}_{\mathrm{int}}$ is assembled as

$$\mathbf{f}^{\mathrm{b}}_{\mathrm{int}} = \sum_e \int_{\Omega^m_e} \mathbf{B}^{\mathsf{T}}\boldsymbol{\sigma}^m = \sum_e \int_{\Omega^m_e} \mathbf{B}^{\mathsf{T}}\mathbf{D}^m\mathbf{B}\,\bar{\mathbf{u}}^m \, \mathrm{d}\Omega_e \quad \text{for} \quad m = \{1,2\}, \tag{2.40}$$

where $\sum\limits_e$ indicates the matrix (or vector) assembly of the global system from the element matrices (or vectors) in the entire computational domain, $\mathbf{B}$ is the strain-displacement relationship matrix defined in Eq. (2.33), $\boldsymbol{\sigma}^m = [\sigma_{11}, \sigma_{22}, \sigma_{12}]^{\mathsf{T}}_{3\times1}$ is the stress tensor in Voigt notation containing only the in-plane components, and $\mathbf{D}^m$ is the $3\times3$ plane strain elasticity matrix in Voigt notation. The corresponding bulk tangent matrix is

$$\mathbf{K}^{\mathrm{b}} = \sum_e \int_{\Omega^m_e} \mathbf{B}^{\mathsf{T}}\mathbf{D}^m\mathbf{B}\,\mathrm{d}\Omega_e \quad \text{for} \quad m = \{1,2\}, \tag{2.41}$$

Neglecting body forces, $\mathbf{f}_{\text{ext}}$ is obtained by assembling the element contributions from any applied traction on the Neumann boundary

$$\mathbf{f}_{\text{ext}} = \sum_e \int_{\Gamma_{ne}} \mathbf{N}^{\mathsf{T}} \bar{\mathbf{t}} \, \mathrm{d}\Gamma_e \tag{2.42}$$

Note that ABAQUS automatically handles the evaluation of $\mathbf{f}_{\text{ext}}$, so simple traction boundary conditions need not be defined using user defined subroutines.

### 2.3.4 Interface elements

The cohesive internal force vector $\mathbf{f}^{\text{c}}_{\text{int}}$ has contributions from both the consistency and stabilization terms in the variational form in Eq. (2.26) and can be assembled as

$$\mathbf{f}^{\text{c}}_{\text{int}} = \mathbf{f}^{\text{consistency}} + \mathbf{f}^{\text{stabilized}} = \sum_e \int_{\Gamma_{*e}} [\![\mathbf{N}]\!]^{\mathsf{T}} (\mathbf{I} - \mathbf{S}) \mathbf{T} \boldsymbol{\sigma}_{\gamma} \, \mathrm{d}\Gamma_e + \sum_e \int_{\Gamma_{*e}} [\![\mathbf{N}]\!]^{\mathsf{T}} \mathbf{S} \boldsymbol{\alpha} \, \boldsymbol{\delta} \, \mathrm{d}\Gamma_e, \tag{2.43}$$

where $[\![\mathbf{N}]\!]$ is the jump in shape function matrix in Eq. (2.35); $\mathbf{S}$, $\boldsymbol{\alpha}$, $\mathbf{I}$ are the $2 \times 2$ stabilization, cohesive stiffness and identity matrices, $\boldsymbol{\sigma}_{\gamma} = [\langle \sigma_{11} \rangle_{\gamma}, \langle \sigma_{22} \rangle_{\gamma}, \langle \sigma_{12} \rangle_{\gamma}]^{\mathsf{T}}_{3\times 1}$ is the weighted Cauchy stress for in-plane components in Voigt notation, and the $2 \times 3$ stress transformation matrix is

$$\mathbf{T} = \begin{bmatrix} -CS & CS & C^2 - S^2 \\ S^2 & C^2 & -2CS \end{bmatrix} \tag{2.44}$$

Thus, the matrix $\mathbf{T}$ defines the relation between the Cauchy stress tensor at any point on a bulk element edge and the traction vector at that point on the cohesive interface based on its orientation. The interface element's tangent stiffness matrix consists of both the consistency and stabilized terms and can be assembled as

$$\mathbf{K}^{\text{c}} = \mathbf{K}^{\text{consistency}} + \mathbf{K}^{\text{stabilized}} = \sum_e \int_{\Gamma_{*e}} [\![\mathbf{N}]\!]^{\mathsf{T}} (\mathbf{I} - \mathbf{S}) \mathbf{T} \mathbf{D} \mathbf{B}_{\gamma} \, \mathrm{d}\Gamma_e + \sum_e \int_{\Gamma_{*e}} [\![\mathbf{N}]\!]^{\mathsf{T}} \mathbf{S} \boldsymbol{\alpha} [\![\mathbf{N}]\!] \, \mathrm{d}\Gamma_e. \tag{2.45}$$

where $\mathbf{B}_\gamma$ denotes the weighted shape function gradient matrix defined as,

$$\mathbf{B}_\gamma = \begin{bmatrix} \gamma^2\mathbf{B}^2 & \gamma^1\mathbf{B}^1 \end{bmatrix}_{3\times 16}. \tag{2.46}$$

In the above equation, $\mathbf{B}^1$ and $\mathbf{B}^2$ are matrices containing the gradient of the shape functions calculated from the adjacent bulk elements at the position of an interface Gauss point of the cohesive element. Note, by setting the matrix $\mathbf{S} = \mathbf{I}$ in Eq. (2.45) we can revert to the standard method.

### 2.3.5 ABAQUS Implementation

The proposed method is implemented in the commercial software ABAQUS, as illustrated in Figure 2.6. All the element force and stiffness matrices described in Section 2.3.3 and Section 2.3.4 have been evaluated via the user-element-material (UELMAT) and user-element (UEL) subroutines for 4-noded bulk and 4-noded interface elements, respectively. The bulk element force vector $\mathbf{f}^{\mathrm{b}}_{\mathrm{int}}$ and the tangent matrix $\mathbf{K}^{\mathrm{b}}$ are computed using the UELMAT subroutine, because it allows for the usage of in-built constitutive models via the `material_lib_mech` function. The cohesive element force vector $\mathbf{f}^{\mathrm{c}}_{\mathrm{int}}$ and the corresponding tangent matrix $\mathbf{K}^{\mathrm{b}}$ are computed using the UEL subroutine, according to Eqs. (2.43) and (2.45). Recall that $\mathbf{f}^{\mathrm{c}}_{\mathrm{int}}$ and $\mathbf{K}^{\mathrm{c}}$ contain the weighted average of stress $\boldsymbol{\sigma}_\gamma$ and shape function derivative matrix $\mathbf{B}_\gamma$, which are calculated using the nodal displacement vectors and shape function matrices of the two neighboring bulk elements. To avoid repetition of computations in our implementation, we calculate $\boldsymbol{\sigma}_\gamma$ and $\mathbf{B}_\gamma$ at the cohesive element Gauss points lying on the bulk element edges in the UELMAT subroutine and pass them to the UEL subroutine using global modules. The tangent matrix $\mathbf{K}^{\mathrm{c}}$ is unsymmetric owing to the consistency term $\mathbf{K}^{\mathrm{consistency}}$ in our formulation, whereas the stabilization term $\mathbf{K}^{\mathrm{stabilized}}$ is symmetric. The matrix $\mathbf{B}_\gamma$ defined in Eq. (2.46) has the dimension of $8 \times 16$, where the number of rows correspond to the interfacial degrees of freedoms (DoFs) and the number of columns correspond to the interfacial and adjacent bulk element DoFs (see Fig. 2.7). However, the UEL subroutine for the cohesive interface element allows access to only its four nodes (i.e., eight DoFs), so we can only assemble an $8 \times 8$ element stiffness matrix. To assemble the $8 \times 16$ element stiffness matrix computed in the UEL subroutine into the global stiffness matrix, we create "dummy" elements in the mesh (elements IV-VII in Fig. 2.7). We partition the $8 \times 16$ element stiffness matrix as,

$$\left[\mathbf{K}^{\text{consistency,e}}\right]_{8\times16} = \left[\begin{array}{c|c|c} \left[\mathbf{K}^{\text{IV}}\right]_{4\times4} & & \left[\mathbf{K}^{\text{V}}\right]_{4\times4} \\ & \left[\mathbf{K}^{\text{III}}\right]_{8\times8} & \\ \left[\mathbf{K}^{\text{VI}}\right]_{4\times4} & & \left[\mathbf{K}^{\text{VII}}\right]_{4\times4} \end{array}\right]. \tag{2.47}$$

and assemble the $8 \times 8$ matrix through the cohesive element and the four $4 \times 4$ matrices through the dummy elements using global modules into the global stiffness matrix. Note that the dummy elements are only used for matrix assembly.

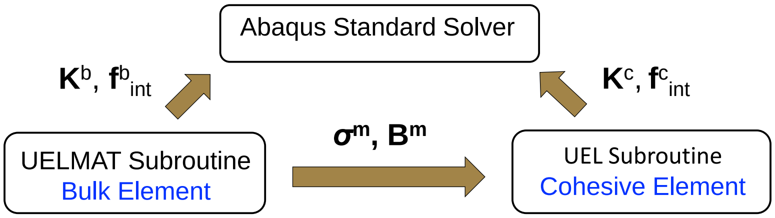

Figure 2.6: Flow chart showing the interaction between UELMAT and UEL subroutines and the ABAQUS standard solver for implementing the stabilized method through user-defined bulk and cohesive/interface elements.

Although the above implementation with dummy elements for the cohesive stiffness matrix assembly seems convoluted, it is efficient and may even be advantageous when interface elements are inserted along all element edges. This is because all bulk stress and shape function matrices at interface Gauss points are computed once in the UELMAT sub-

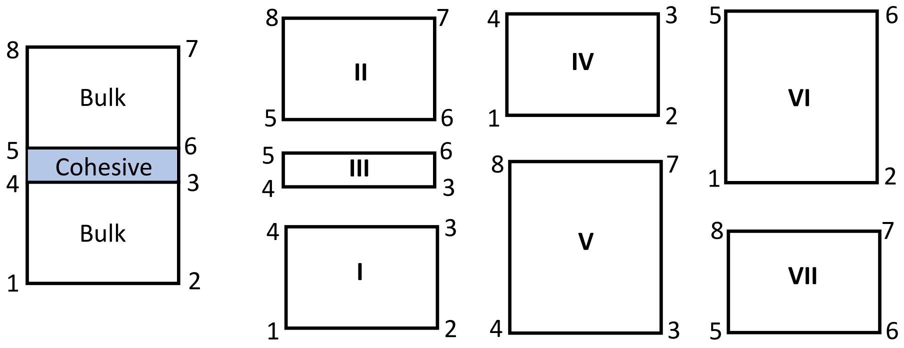

Figure 2.7: Assembly of the cohesive element matrix $\mathbf{K}^{\text{consistency,e}}$ defined in Eq. (2.47) into the global tangent matrix in ABAQUS requires the creation of four dummy elements (IV-VII) for each cohesive element (III).

routine and stored in global modules, instead of recomputing it wherever needed in the UEL subroutine. We found that our implementation of the stabilized method did not increase the wall clock time of computation (compared to standard method) in all the numerical examples presented in Section 2.4. However, we note that alternative implementations of the stabilized method in existing finite element codes are possible. For example, Versino et al. [81] used ABAQUS UEL subroutine for a 8-noded interface element in 2D to implement a discontinuous Galerkin based extrinsic cohesive zone model. This implementation may be more advantageous when interface elements are inserted along simple (straight) interfaces between laminate plies in composite materials.

The UELMAT and UEL subroutines are detailed in Algorithms 1 and 2, respectively. As discussed in [79], we formulate the bilinear cohesive zone model within the damage mechanics framework that allows us to automatically handle the unloading/reloading conditions based on a previous maximum damage (history variable). Despite the bilinear shape of the cohesive law, the damage variable is a nonlinear function of interface separation and this nonlinearity is handled by Abaqus/Standard outside of the user subroutines. As detailed in the Abaqus manual [86, Chapter 7: Analysis Solution and Control], Abaqus/-Standard combines incremental and iterative (Newton-Raphson) procedures for solving nonlinear problems. The total load/displacement is applied incrementally as smaller increments (pseudo-time steps) and the user typically suggests the size of the first increment and Abaqus/Standard automatically chooses the size of the subsequent increments. Within each increment, Abaqus/Standard automatically performs iteration to find an equilibrium solution based on a user-defined criteria for residual force and displacement correction. We note that, in cohesive fracture simulations, the Abaqus/Standard default criteria may be too small that numerical convergence may not be attainable. Therefore, we increase these tolerances appropriately so as to attain convergence and maintain adequate accuracy, to obtain the results in Section 2.4.4 and Section 2.4.5.

---

**Algorithm 1** : ABAQUS UELMAT subroutine for the bulk element

Given all the variables at the previous iteration of the current increment, at the next iteration:

1. Compute the shape function derivative matrix $\mathbf{B}$ according to Eq. (2.33)
2. Determine the $3 \times 3$ plane strain elasticity tensor $\mathbf{D}$ via the `material_lib_mech` function
3. Compute and assemble the bulk element contributions to the tangent matrix and the internal force vector using four-point Gauss integration
4. Determine $\boldsymbol{\sigma}^{\mathrm{m}}$ and shape function derivatives $\mathbf{B}^{\mathrm{m}}$ at the two interface Gauss integration points and store them in global modules

---

## 2.4 Numerical examples

In this section, we present four examples to demonstrate the numerical stability and accuracy of the proposed stabilized method in two-dimensions. For all the simulations we assumed bilinear quadrilateral plane strain elements with four-point Gauss integration scheme and four-noded linear cohesive elements with two-point Gauss integration scheme. Currently, the user element subroutines are written only for 2D plane-strain and plane-stress elements in Abaqus software. Additional patch tests and benchmark problems have

**Algorithm 2** : ABAQUS UEL subroutine for the cohesive element

Given all the variables at the previous iteration of the current increment, at the next iteration:

1. Compute the jump in the interfacial shape function matrix $[\![\mathbf{N}]\!]$ according to Eq. (2.35) and the interface separation vector $[\![\mathbf{u}]\!]$ using Eq. (2.34)

2. Calculate equivalent separation $\delta_e$, and equivalent critical $\delta_e^c$ and maximum $\delta^u$ separations according to Eq. (2.12), and static damage $D_s$ using Eq. (2.10)

3. Calculate the stabilization matrix $\mathbf{S}$ according to Eq. (2.24)

4. Calculate the weighted stress $\langle \boldsymbol{\sigma} \rangle_\gamma$ and shape function derivative matrix $\mathbf{B}_\gamma$, according to Eqs. (2.46) and using the information passed from the UELMAT subroutine

5. Compute and assemble the cohesive element contributions corresponding to the stabilized part of the tangent matrix and the internal force vector using two-point Gauss integration

6. Define the $3 \times 3$ plane strain elasticity tensor $\mathbf{D}$ and the stress transformation matrix $\mathbf{T}$.

7. Compute the cohesive element contributions corresponding to the consistency part of the tangent matrix and the internal force vector using two-point Gauss integration

8. Partition $\left[\mathbf{K}^{\text{consistency},e}\right]_{8\times 16}$ into one $8 \times 8$ matrix $\left[\mathbf{K}^{\text{III}}\right]$ and four $4 \times 4$ matrices $\left[\mathbf{K}^{\text{IV}}\right], \left[\mathbf{K}^{\text{V}}\right], \left[\mathbf{K}^{\text{VI}}\right], \left[\mathbf{K}^{\text{VII}}\right]$, as described in Eq. (2.47).

9. Assemble partitioned matrices into the global stiffness matrix using the cohesive element (III) and four dummy elements (IV–VII) (see Fig. 2.7).

been presented in [87, 88].

### 2.4.1 Square plate with horizontal interface

In this example, we assess the accuracy of the stabilized method in recovering normal traction on a straight, horizontal interface with isotropic CZMs using a constant strain patch test [89]. We consider a square plate of side length $L = 1$ mm with a horizontal interface at mid-height (see Fig. 2.8a). Both vertical and horizontal displacements are constrained at the bottom edge of the plate, whereas a uniform vertical displacement $\Delta = 0.1$ mm is applied at the top edge of the plate, and traction-free conditions are specified on the left and right edges of the square plate. The Young's modulus and Poisson's ratio of the isotropic linearly elastic material in the bulk elements are assumed as $E = 1$ N/mm$^2$ and $\nu = 0.2$, respectively. We use a $10 \times 10$ structured square mesh with an element size of 0.1 mm and the stabilization parameters $\beta_n = \beta_\tau = 14$ N/mm$^3$. The analysis is conducted under the assumption of small deformations and no interface damage (i.e., $d_s = 0$), although the bulk applied strain is 10%. The normal traction profile along the horizontal interface obtained from the standard and stabilized methods for different cohesive stiffness values is shown in Fig. 2.9. For the smaller cohesive stiffness value of 100 N/mm$^3$ both methods yield oscillation-free traction profile at the cohesive interface. For the larger stiffness value of $10^{16}$ N/mm$^3$, the standard method exhibits instability resulting in spurious traction oscillations; whereas, the stabilized method does not exhibit any instability.

To demonstrate the accuracy of stabilized method for stiff cohesive laws, we report the relative $l^2$-error (vector norm) in normal traction and separation for different values of initial cohesive stiffness in Table 2.1. The relative $l^2$-errors are calculated as

$$\frac{||\varepsilon_{t_n}||_2}{||t_n^*||_2} = \frac{\sqrt{\sum_{i=1}^{N_{\text{GP}}} \left(t_n^i - t_n^{*i}\right)^2}}{\sqrt{\sum_{i=1}^{N_{\text{GP}}} \left(t_n^{*i}\right)^2}}; \quad \frac{||\delta_n||_2}{||u_n^*||_2} = \frac{\sqrt{\sum_{i=1}^{N_{\text{GP}}} \left(\delta_n^i\right)^2}}{\sqrt{\sum_{i=1}^{N_{\text{GP}}} \left(u_n^{*i}\right)^2}} \tag{2.48}$$

where $N_{\text{GP}}$ is the total number of Gauss (integration) points on the cohesive interface,

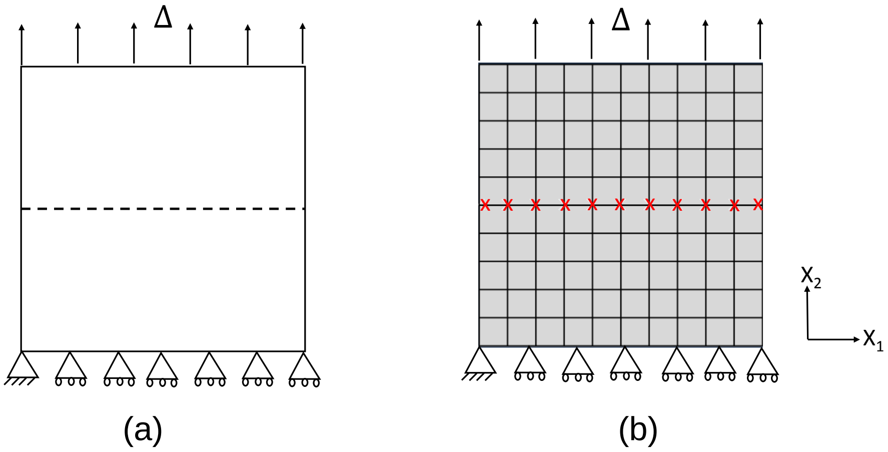

Figure 2.8: Square plate with horizontal interface: (a) schematic diagram; (b) finite element mesh

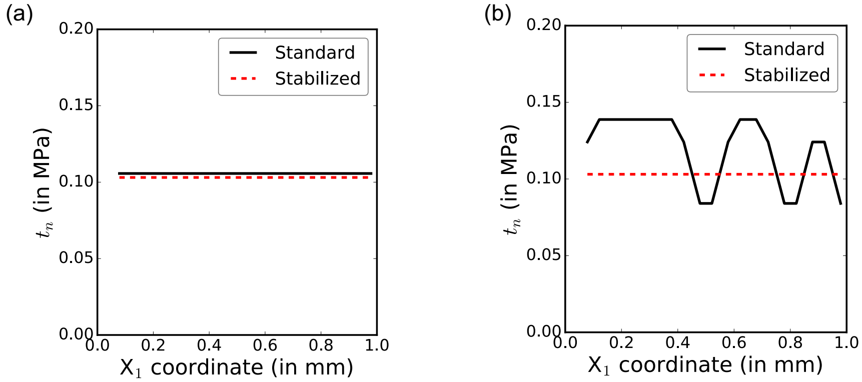

Figure 2.9: Square plate with a horizontal interface: normal traction profiles obtained from the standard and stabilized methods with (a) $\alpha_n^0 = \alpha_\tau^0 = 10^2$ N/mm$^3$ and (b) $\alpha_n^0 = \alpha_\tau^0 = 10^{16}$ N/mm$^3$ .

interface separation $\delta_n$ and traction $t_n$ are evaluated using equations (2.6) and (2.29) respectively, and the reference values of the traction $t_n^*$ and displacement $u_n^*$ at the horizontal interface are calculated for the perfectly bonded interface case under the plane strain linear elastic assumption as

$$t_n^* = \left(\frac{\Delta}{L}\right)\frac{E}{(1-\nu^2)}; \quad u_n^* = \frac{\Delta}{2}. \tag{2.49}$$

In the above equation, the normal traction is calculated based on the engineering strain (defined with respect to the initial length) under the assumption of small deformations and $E/(1-\nu^2)$ is the plane strain elastic modulus [90]. From Table 2.1 it is evident that the

Table 2.1: Square plate with a horizontal cohesive interface: relative $l^2$-error in normal traction and separations from the standard and stabilized finite element methods for different cohesive stiffness. The bilinear isotropic CZM is used, wherein the tangential and normal cohesive stiffness are taken to be equal.

| Cohesive Stiffness (N/mm$^3$) | Standard FEM | | Stabilized FEM | |
|---|---|---|---|---|
| | $\frac{\|\|\varepsilon_{t_n}\|\|_2}{\|\|t_n^*\|\|_2}$ | $\frac{\|\|\delta_n\|\|_2}{\|\|u_n^*\|\|_2}$ | $\frac{\|\|\varepsilon_{t_n}\|\|_2}{\|\|t_n^*\|\|_2}$ | $\frac{\|\|\delta_n\|\|_2}{\|\|u_n^*\|\|_2}$ |
| $10^2$ | 1.4% | $2.1\times10^{-2}$ | 1% | $2.1\times10^{-2}$ |
| $10^8$ | 2.5% | $2.2\times10^{-8}$ | $1\times10^{-8}$ | $2\times10^{-8}$ |
| $10^{15}$ | 4.6% | $2.2\times10^{-15}$ | $3.7\times10^{-15}$ | $2\times10^{-15}$ |
| $10^{16}$ | 25.7% | $1.3\times10^{-16}$ | $1.8\times10^{-17}$ | $2.4\times10^{-16}$ |

Table 2.2: Square plate with a horizontal cohesive interface: relative $l^2$-error in normal traction and separations from the standard and stabilized finite element methods for different mesh resolutions. The bilinear isotropic CZM is used, wherein the tangential and normal cohesive stiffness are taken to be $10^{8}$ N/mm$^3$.

| Mesh size (mm) | Standard FEM | | Stabilized FEM | |
|---|---|---|---|---|
| | $\frac{\|\|\varepsilon_{t_n}\|\|_2}{\|\|t_n^*\|\|_2}$ | $\frac{\|\|\delta_n\|\|_2}{\|\|u_n^*\|\|_2}$ | $\frac{\|\|\varepsilon_{t_n}\|\|_2}{\|\|t_n^*\|\|_2}$ | $\frac{\|\|\delta_n\|\|_2}{\|\|u_n^*\|\|_2}$ |
| 0.1 | 2.5% | $2.2\times10^{-8}$ | $1\times10^{-8}$ | $2\times10^{-8}$ |
| 0.04 | 2.5% | $2.2\times10^{-8}$ | $1\times10^{-8}$ | $2\times10^{-8}$ |
| 0.02 | 2.5% | $2.2\times10^{-8}$ | $1\times10^{-8}$ | $2\times10^{-8}$ |

stabilized method ensures accurate recovery of interface traction compared to the standard method. As the cohesive stiffness is increased to a large value the interface separation tends to zero (to machine precision) in both the standard and stabilized methods, but the error in interface traction tends to zero (to machine precision) only in the stabilized method. We also notice that the computational time with the standard and stabilized method is comparable. We next investigate the effect of mesh refinement on the accuracy of traction evaluation for structured meshes. For an initial cohesive stiffness of $10^8$ N/mm$^3$, we see that the traction error does not change with mesh refinement in both methods, as given in Table 2.2. This further illustrates that the improvement in accuracy with the stabilized method ensues from the consistent weak formulation in Eq. (2.26).

### 2.4.2 Square plate with inclined interface

In this example, we assess the accuracy of the stabilized method in recovering normal and tangential tractions on an straight, inclined interface with isotropic and anisotropic CZMs using the constant strain patch test [89]. We consider a square plate of side length $L = 1$ mm with a straight interface inclined at an initial angle of 140.4° with the global $x_1$ (i.e., horizontal) axis, as shown in Fig. 2.10. We use a $13 \times 18$ semi-structured mesh so that the interface is divided into 13 elements. The support conditions, loading and material properties are identical to those discussed in Section 2.4.1, and the stabilization parameters $\beta_n = \beta_\tau = 30$ N/mm$^3$. The analysis is conducted under the assumption of small deformations and no interface damage (i.e., $d_s = 0$). The normal and tangential tractions along the inclined interface obtained from the standard and stabilized methods for different cohesive stiffness values are shown in Fig. 2.11. For the smaller cohesive stiffness value of 100 N/mm$^3$ both methods yield oscillation-free traction profiles at the cohesive interface. For the larger stiffness value of $10^{16}$ N/mm$^3$, the standard method exhibits instability resulting in spurious traction oscillations; whereas, the stabilized method does not exhibit such an instability.

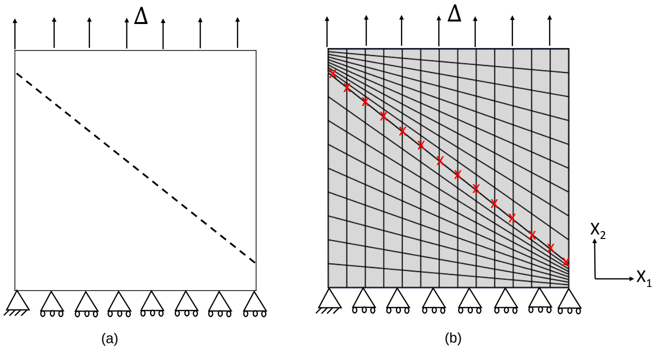

Figure 2.10: Square plate with inclined interface: (a) schematic diagram; (b) finite element mesh

To illustrate the accuracy of the stabilized method for stiff isotropic CZMs, we report the relative $l^2$-error in normal and tangential tractions for different values of initial cohesive stiffness using the isotropic bilinear CZM in Table 2.3. The reference value of the normal

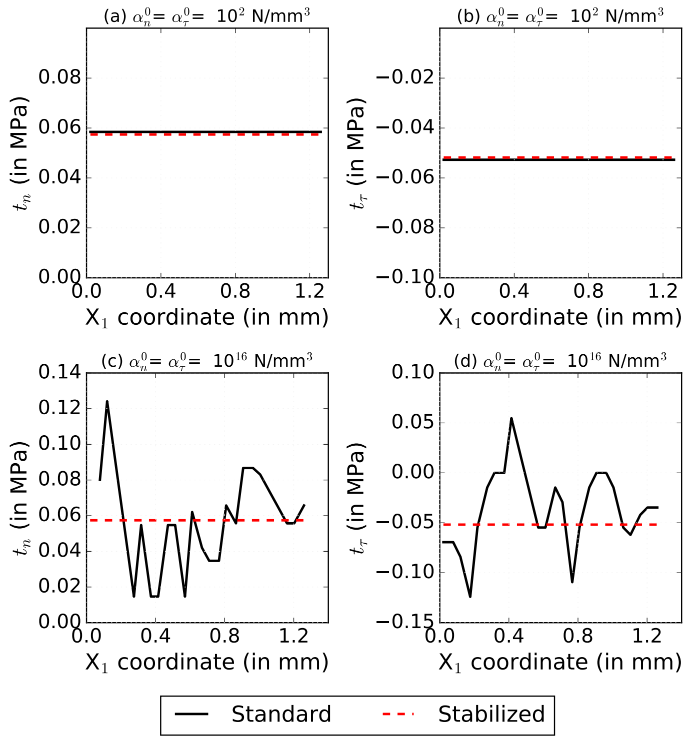

Figure 2.11: Square plate with an inclined interface: traction profiles obtained from the standard and stabilized methods for isotropic cohesive zone models for two different cohesive stiffness values.

and tangential tractions $t_n^*$ and $t_\tau^*$ under the plane strain and perfectly bonded interface assumptions can be evaluated as

$$t_n^* = \left(\frac{\Delta}{L}\right) \frac{E}{(1-\nu^2)} \sin^2\theta; \quad t_\tau^* = \left(\frac{\Delta}{L}\right) \frac{E}{(1-\nu^2)} \sin\theta\cos\theta, \tag{2.50}$$

where $\theta = 140.4°$ is the angle that the inclined interface makes with the global x$_1$ axis in the undeformed (initial) configuration. From Table 2.3, it is evident that the stabilized method ensures accurate recovery of interface traction for large values of cohesive stiffness; whereas, in the standard method the interface traction error increases with the cohesive stiffness.

We next examine the performance of the standard and stabilized methods for anisotropic CZMs, wherein the normal and tangential cohesive stiffness values are not equal. It can

Table 2.3: Square plate with inclined interface: relative $l^2$-error in normal and tangential tractions from the standard and stabilized finite element methods for different cohesive stiffness. The bilinear isotropic CZM is used, wherein the tangential and normal cohesive stiffness are taken to be equal.

| Cohesive Stiffness (N/mm$^3$) | Standard FEM $\frac{\|\|\varepsilon_{t_n}\|\|_2}{\|\|t_n^*\|\|_2}$ | $\frac{\|\|\varepsilon_{t_\tau}\|\|_2}{\|\|t_\tau^*\|\|_2}$ | Stabilized FEM $\frac{\|\|\varepsilon_{t_n}\|\|_2}{\|\|t_n^*\|\|_2}$ | $\frac{\|\|\varepsilon_{t_\tau}\|\|_2}{\|\|t_\tau^*\|\|_2}$ |
|---|---|---|---|---|
| $10^2$ | 1.7% | 1.8% | 0.7% | 0.8% |
| $10^8$ | 2.6% | 2.6% | $1.1\times10^{-7}$ | $3.4\times10^{-8}$ |
| $10^{14}$ | 3.0% | 2.6% | $8.3\times10^{-10}$ | $1.1\times10^{-10}$ |
| $10^{16}$ | 64.9% | 80.2% | $9.3\times10^{-11}$ | $9.1\times10^{-11}$ |

Table 2.4: Square plate with inclined interface: relative $l^2$-error in normal and tangential tractions from the standard and stabilized finite element methods for different cohesive stiffness. The bilinear anisotropic CZM is used, wherein the tangential and normal cohesive stiffness are taken to be different from each other.

| Cohesive Stiffness (N/mm$^3$) | Standard FEM $\frac{\|\|\varepsilon_{t_n}\|\|_2}{\|\|t_n^*\|\|_2}$ | $\frac{\|\|\varepsilon_{t_\tau}\|\|_2}{\|\|t_\tau^*\|\|_2}$ | Stabilized FEM $\frac{\|\|\varepsilon_{t_n}\|\|_2}{\|\|t_n^*\|\|_2}$ | $\frac{\|\|\varepsilon_{t_\tau}\|\|_2}{\|\|t_\tau^*\|\|_2}$ |
|---|---|---|---|---|
| $\alpha_n^0= 10^5$, $\alpha_\tau^0= 10^2$ | 2.2% | 2.2% | 0.3% | 0.3% |
| $\alpha_n^0= 10^{11}$, $\alpha_\tau^0= 10^7$ | 2.6% | 2.6% | $1.1\times10^{-7}$ | $4.9\times10^{-8}$ |
| $\alpha_n^0= 10^{15}$, $\alpha_\tau^0= 10^{11}$ | 10.5% | 2.6% | $8.3\times10^{-10}$ | $1.1\times10^{-10}$ |

be seen from Fig. 2.12, that the standard method yields an oscillation-free traction profile for smaller stiffness values, but it suffers from instability for larger values with spurious oscillations in the normal traction profile. In contrast, the stabilized method yields an oscillation-free traction profile regardless of the choice of cohesive stiffness. In Table 2.4 we report the accuracy of the stabilized and standard methods for the anisotropic CZM. We observe that for the assumed normal and tangential stiffness values, the stabilized method recovers crack-surface traction more accurately compared to the standard method; the error in traction decreases close to machine precision in the stabilized method as the stiffness is increased to a very large value.

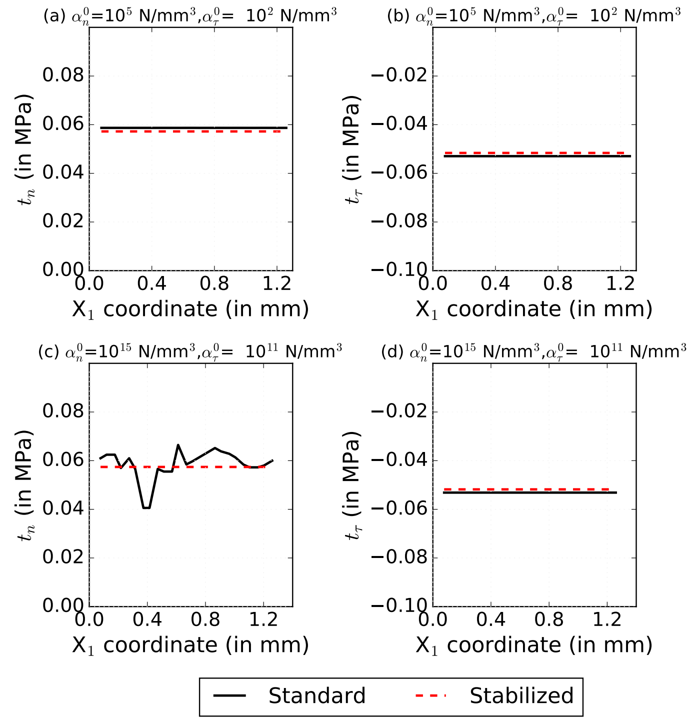

Figure 2.12: Square plate with an inclined interface: traction profiles obtained from the standard and stabilized methods for anisotropic cohesive zone models for different cohesive stiffnesses.

### 2.4.3 Square plate with semicircular interface

In the previous examples, we considered constant strain patch tests with straight interfaces described by isotropic and anistropic CZMs; in these cases traction oscillations do not appear if full Gauss integration is used with the standard method, except if the initial cohesive stiffness values is assumed to be very large (i.e., $\alpha_n^0 \geq 10^{15}$ N/mm$^3$). However, Svenning [14] has shown that spurious tractions oscillations can appear with curved interfaces described by an anisotropic CZM under compression, even for moderately large values of cohesive stiffness (e.g., 2–4 orders of magnitude more than the Young's modulus). Therefore, in this example, we demonstrate the ability of the stabilized method to alleviate traction oscillations on a semicircular interface with an anisotropic CZM. We consider a square plate of side length $L = 100$ mm with a cohesive interface of diameter 60 mm, as shown in Fig. 2.13. A horizontal compressive displacement of $\Delta = 1$ mm is applied

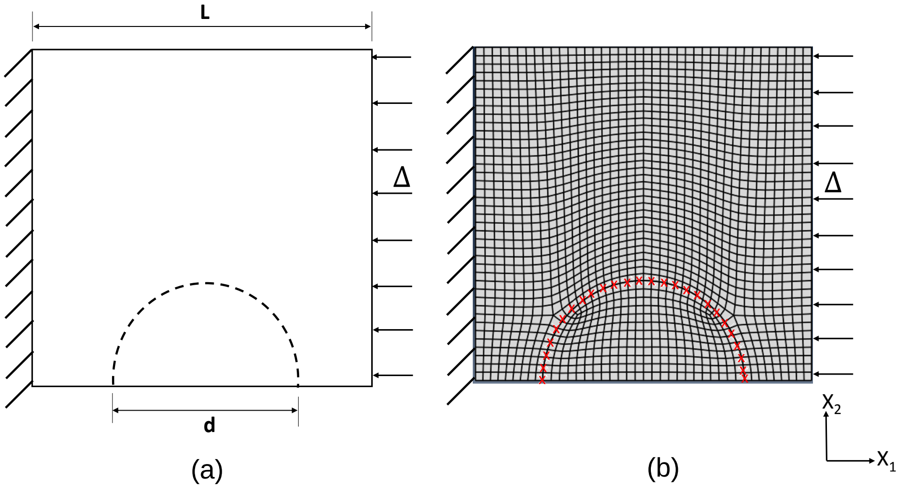

Figure 2.13: Square plate with semicircular interface: (a) schematic diagram; (b) finite element mesh.

on the right edge of the plate, the displacement at the left edge is constrained in both directions, and traction-free condition is specified for the top and bottom edges of the plate. We assume the plane strain condition and a linear elastic bulk material with a modulus of elasticity $E = 20$ GPa, and a Poisson's ratio $\nu = 0.2$, following the example in [14]. The analysis is conducted under the assumption of small deformations and no interface damage (i.e., $d_s = 0$).

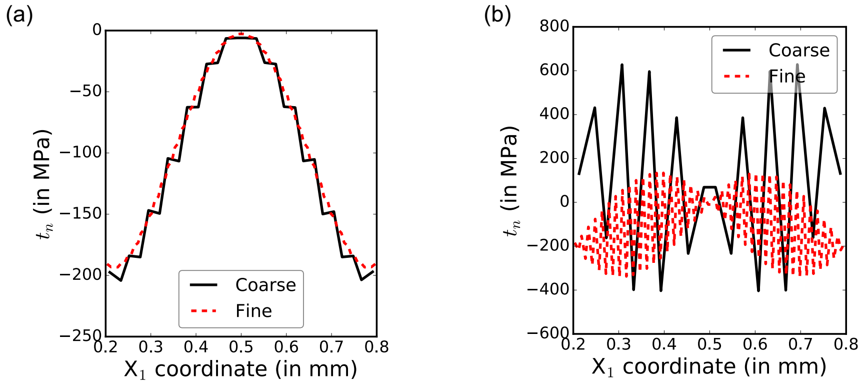

Figure 2.14: Square plate with semicircular interface: effect of mesh refinement on normal traction profiles predicted by the standard method. (a) $\alpha_n^0$= $\alpha_\tau^0$= $10^{11}$ N/mm$^3$ and (b) $\alpha_n^0$= $10^{11}$ N/mm$^3$ and $\alpha_\tau^0$= $10^9$ N/mm$^3$.

We first examine the performance of the standard method for isotropic and anisotropic

CZMs using unstructured meshes. We consider a coarse mesh with 240 elements and a fine mesh with 1780 elements with bilinear quadrilateral elements. For the isotropic CZM we take normal and tangential cohesive stiffnesses $\alpha_n^0 = \alpha_\tau^0 = 10^{11}$ N/mm$^3$ and for the anisotropic CZM we take $\alpha_n^0$= $10^{11}$ N/mm$^3$ and $\alpha_\tau^0$= $10^9$ N/mm$^3$. Fig. 2.14 shows the normal traction profiles along the cohesive interface obtained from the standard method. Fig. 2.14(a) indicates that the standard method yields a smooth traction profile with the isotropic CZM if the mesh is adequately refined. However, mesh refinement cannot alleviate spurious traction oscillations with the anisotropic CZM, as evident from Fig. 2.14(b). This issue with the standard (penalty-like) method for anisotropic CZMs was previously reported in [14].

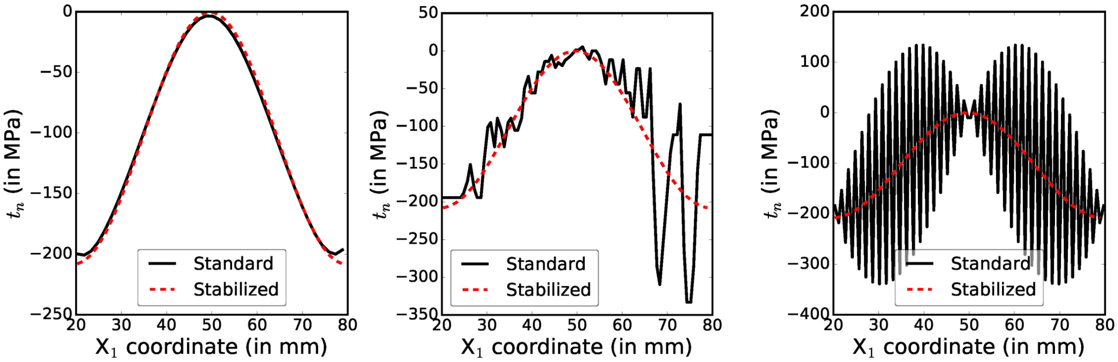

(a) (b) (c)

Figure 2.15: Square plate with semicircular interface: Normal traction profiles obtained from the standard and stabilized method for different cohesive stiffness. (a) isotropic CZM with $\alpha_n^0 = \alpha_\tau^0 = 10^{11}$ N/mm$^3$, (b) isotropic CZM $\alpha_n^0 = \alpha_\tau^0 = 10^{18}$ N/mm$^3$ and (c) anisotropic CZM $\alpha_n^0 = 10^{11}$ N/mm$^3$ and $\alpha_\tau^0 = 10^9$ N/mm$^3$

In Figure 2.15, we compare the performance of the standard and stabilized methods for isotropic and anisotropic CZMs using the fine mesh (with 1780 elements). According to Eq. (2.25), we take the stabilization parameters $\beta_n = \beta_\tau = 2 \times 10^5$ N/mm$^3$. Figure 2.15(a) and (b) show that for isotropic CZMs the standard method suffers from numerical instability only for very large values of cohesive stiffness (i.e., $10^{18}$ N/mm$^3$); whereas, the stabilized method yields an oscillation-free traction profile. Figure 2.15(c) shows that the stabilized method is able to alleviate the spurious oscillations in normal traction observed

Table 2.5: Square plate with semicircular interface: accuracy of the standard and stabilized finite element methods. We consider both isotropic and anisotropic CZMs and relative $l^2$-error in normal tractions is reported.

| Cohesive Stiffness (N/mm$^3$) | Standard FEM $\frac{\|\|\varepsilon_{t_n}\|\|_2}{\|\|t_n^*\|\|_2}$ | Stabilized FEM $\frac{\|\|\varepsilon_{t_n}\|\|_2}{\|\|t_n^*\|\|_2}$ |
|---|---|---|
| $\alpha_n^0$=$\alpha_\tau^0$= $10^8$ | 2.9% | $4.3\times10^{-8}$ |
| $\alpha_n^0$=$\alpha_\tau^0$= $10^{11}$ | 2.9% | $4.3\times10^{-8}$ |
| $\alpha_n^0$= $10^8$, $\alpha_\tau^0$= $10^6$ | 117.1% | $4.2\times10^{-8}$ |
| $\alpha_n^0$= $10^{11}$, $\alpha_\tau^0$= $10^9$ | 117.6% | $1.3\times10^{-7}$ |

with the standard method for the anisotropic CZM with $\alpha_n^0 = 10^{11}$ N/mm$^3$ and $\alpha_\tau^0 = 10^9$ N/mm$^3$. These results illustrate that the standard method is not robust when dealing with stiff anisotropic cohesive laws, unlike the stabilized method.

We next evaluate the relative $l^2$-error in interface traction from the standard and stabilized methods. Assuming that the interface is perfectly bonded for large values of cohesive stiffness $\alpha_n^0 > 10^8$ N/mm$^3$, $\alpha_\tau^0 > 10^6$ N/mm$^3$, the exact value of the normal and tangential tractions $t_n^*$ and $t_\tau^*$ at interface Gauss points can be calculated using Eq. (2.50), wherein $\theta$ is the local orientation of the interface element that varies along semicircular interface. Table 2.5 shows that the stabilized method ensures the accurate recovery of normal traction at the interface for both isotropic and anisotropic CZMs, unlike the standard method. Even if the cohesive stiffness $\alpha_n^0 = 10^8$ N/mm$^3$ and $\alpha_\tau^0 = 10^6$ N/mm$^3$ are 2–4 orders of magnitude larger than the Young's modulus $E = 20 \times 10^3$ N/mm$^3$, we see that the standard method performs quite poorly with 117 % error in normal traction and exhibits spurious oscillations (results are identical to Fig. 2.14 (b)). Noting that in mode II fracture analysis, an anisotropic cohesive laws with $\alpha_n^0 > \alpha_t^0$ is typically used to enforce the no inter-penetration condition at the crack surface, the stabilized method can offer a significant advantage owing to its stability and accuracy.

### 2.4.4 Asymmetric double cantilever beam

In all the previous examples, we conducted linear elastic analysis under the assumption of small deformations and no interface damage (i.e., $d_s = 0$) to illustrate the accuracy of the stabilized method in recovering crack-surface traction. In this example, we will examine the accuracy of the stabilized method for analyzing mixed-mode delamination crack growth in composite materials using the asymmetric double cantilever beam (DCB). While the specimen geometry and test set-up shown in Fig. 2.16 resembles that in [91, 92], we altered the applied load configuration. The fixed boundary condition is applied at the right end of the beam, and vertical displacements $\Delta_1$ and $\Delta_2$ are applied at the upper and lower nodes at the left end (with $\Delta_2/\Delta_1 = 0.095$), to initiate the delamination process. Thus, using a displacement-controlled simulation, we capture the softening portion of the load-displacement curve due to the evolution of damage $d_s$ in the interface elements; however, the mode-mix ratio between mode I and mode II fracture is not a constant, because the applied loads are not constant. We now perform numerical convergence studies using a structured square mesh with an element size of 0.125 mm, so that the cohesive process zone is adequately resolved according to the guidelines described in [3]. The material properties and cohesive parameters assumed for this test are listed in Table 2.6, and the stabilization parameters $\beta_n = \beta_\tau = 2 \times 10^6$ N/mm$^3$.

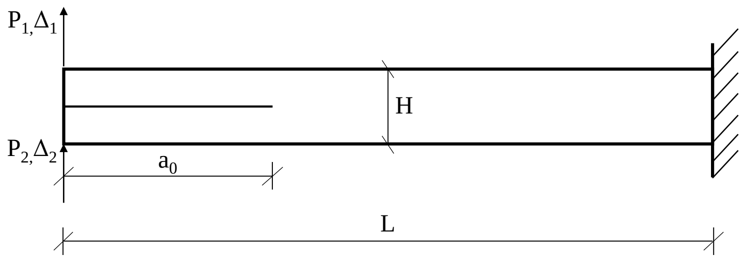

Figure 2.16: Geometry and boundary conditions for the asymmetric double cantilever beam test. The dimensions are: L = 100 mm, H = 4 mm and $a_0$ = 25 mm

To solve this nonlinear quasi-static fracture problem, we need to linearize the dis-

Table 2.6: Material properties and cohesive parameters for the asymmetric double cantilever beam. The cohesive parameters are assumed from [1] for mixed-mode loading conditions.

| E ($N/mm^2$) | $\nu$ | $G_{IC}$ (N/mm) | $G_{IIC}$ (N/mm) | $\sigma_{max}$ ($N/mm^2$) | $\tau_{max}$ ($N/mm^2$) |
|---|---|---|---|---|---|
| $10^5$ | 0.35 | 4.0 | 4.0 | 57 | 57 |

cretized equilibrium equation using the Taylor series expansion (see Eq. (2.37)) at a given iteration and applied load/displacement step; in order to ensure accuracy it is necessary to take the applied displacement increment small enough within a load/displacement step [93]. In ABAQUS, this can be achieved by prescribing a small displacement increment $\dot{\Delta}$ within the default quasi-static pseudo-time stepping algorithm. Because the weak form and the corresponding discretized equilibrium equation from standard and stabilized methods are different, we investigate their accuracy in relation to the choice of displacement increment along with the cohesive stiffness. In Fig. 2.17, we plot the load-displacement responses for two different displacement rates (0.005 mm/step and 0.001 mm/step) and cohesive stiffness values ($\alpha_n^0 = \alpha_\tau^0 = 10^8$ N/mm$^3$ and $\alpha_n^0 = \alpha_\tau^0 = 10^{12}$ N/mm$^3$). For the smaller stiffness of $10^8$ N/mm$^3$ (see Fig. 2.17a), the standard and stabilized methods predict the same load-displacement curve for $\dot{\Delta} = 0.001$ mm/step; however, both methods are slightly inaccurate for $\dot{\Delta} = 0.005$ mm/step. We also used a smaller displacement increment $\dot{\Delta} = 0.0005$ mm/step (results not shown) and observed that the load-displacement curves match exactly with those obtained with $\dot{\Delta} = 0.001$ mm/step. For the larger stiffness of $10^{12}$ N/mm$^3$ (see Fig. 2.17b), the standard and stabilized methods predict the same load-displacement curve for $\dot{\Delta} = 0.001$ mm/step, but the standard method is significantly inaccurate for $\dot{\Delta} = 0.005$ mm/step and shows oscillations in the softening portion of the load-displacement curve. In contrast, the load-displacement curve obtained from the stabilized method for $\dot{\Delta} = 0.005$ mm/step is reasonably accurate without any oscillations in the softening portion.

To further explore the reason behind the inaccuracy in load-predictions for larger displacement rates, we plot the crack versus displacement curves in Fig. 2.18 for two cohesive stiffness values considered above. For the smaller stiffness of $10^8$ N/mm$^3$ (see Fig. 2.18a), the standard and stabilized methods predict the same crack growth behavior for the two displacement rates. However, for the larger stiffness of $10^{12}$ N/mm$^3$ (see Fig. 2.18b), the standard method predicts slower crack growth for $\dot{\Delta} = 0.005$ mm/step, which leads to the inaccurate prediction of softening portion of the load-displacement response. In contrast, the stabilized method predicts reasonably similar crack growth behavior for the two displacement rates. We next examine the normal and tangential traction profiles along the cohesive interface predicted by the standard and stabilized methods for the larger cohesive stiffness of $10^{12}$ N/mm$^3$. In Fig. 2.19, we plot the traction versus interface length at an applied displacement $\Delta = 6.4$ mm for $\dot{\Delta} = 0.005$ mm/step and 0.001 mm/step. In Fig. 2.19(a), the normal traction profiles from both methods match well for $\dot{\Delta} = 0.001$ mm/step; but the profile predicted by the standard method for $\dot{\Delta} = 0.005$ mm/step shows traction oscillations near the tension peak and plateau region near the compression peak. Because the crack length predicted by the standard method is smaller, the corresponding traction profile lags behind the other profiles. The tangential traction profiles in Fig. 2.19(b) also show similar behavior. Notably, oscillations in tangential traction can be observed even for $\dot{\Delta} = 0.001$ mm/step in the standard method. In summary, this study illustrates that the accurate recovery of crack-surface traction by the stabilized method can enable computationally-efficient and reliable prediction of delamination crack propagation and load-displacement curves.

### 2.4.5 Double cantilever beam

In this example, we investigate the accuracy of the stabilized method in recovering crack-face traction for mode-I delamination crack growth using the double cantilever beam (DCB). We also examine the sensitivity of load-displacement curves to interface cohesive strength and mesh/element size. The specimen geometry and test set-up are identical to that in the previous example shown in Fig. 2.16, except for the applied load configu-

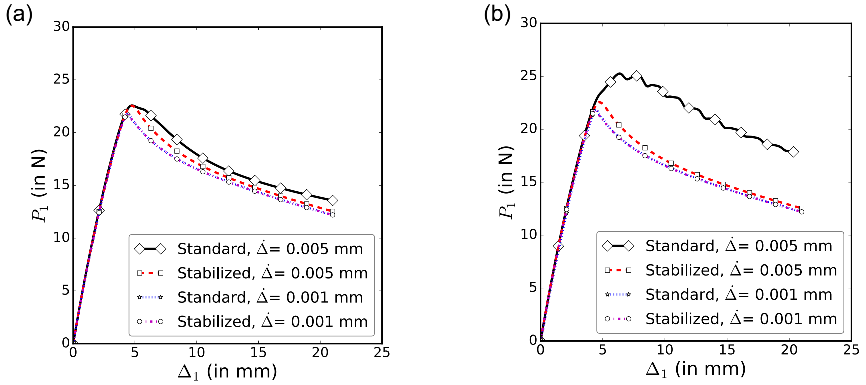

Figure 2.17: Load versus displacement curves for the asymmetric double cantilever beam test: (a) $\alpha_n^0$= $\alpha_\tau^0$= $10^8$ N/mm$^3$ and (b) $\alpha_n^0$= $\alpha_\tau^0$= $10^{12}$ N/mm$^3$

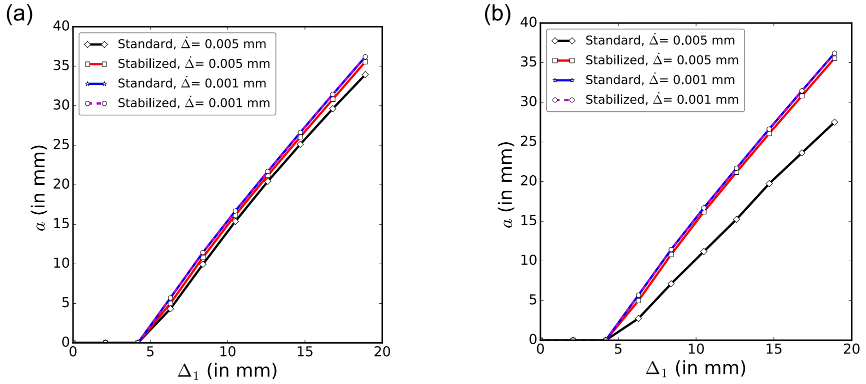

Figure 2.18: Crack versus displacement curves for the asymmetric double cantilever beam test: (a) $\alpha_n^0$= $\alpha_\tau^0$= $10^8$ N/mm$^3$ and (b) $\alpha_n^0$= $\alpha_\tau^0$= $10^{12}$ N/mm$^3$

ration. Specifically, at the left end of the beam we apply vertical displacements $\Delta_1$ and $\Delta_2$ on the upper and lower nodes with $\Delta_1/\Delta_2 = -1$ to initiate the delamination process. Thus, using a displacement-controlled simulation, we capture the softening portion of the load-displacement curve due to the evolution of damage $d_s$ in the interface elements. The material properties and cohesive parameters assumed for this test are listed in Table 2.7. We choose the displacement increment $\dot{\Delta} = 0.0001$ mm/step, cohesive stiffness $\alpha_n^0$= $10^8$ N/mm$^3$, and and the stabilization parameters $\beta_n = \beta_\tau = 2 \times 10^6$ N/mm$^3$ for all the simulations.

In Fig. 2.20, we plot the load-displacement responses for different interface strengths and mesh sizes along with the linear elastic analytical solution given in [1]. For the fine

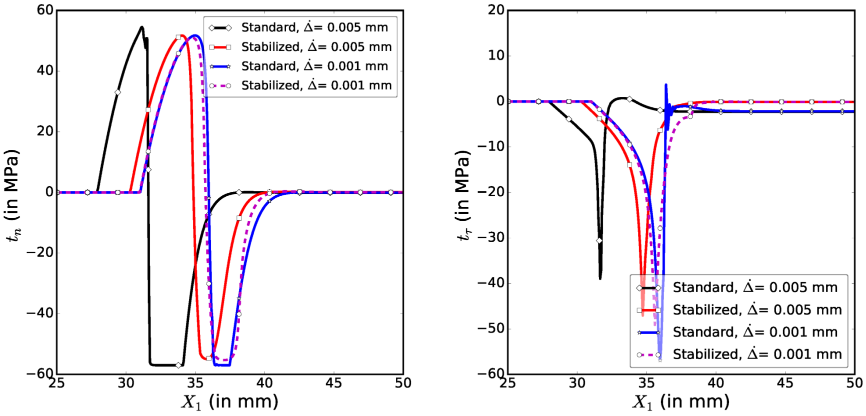

(a) (b)

Figure 2.19: Traction versus interface length curves for the asymmetric double cantilever beam test for $\alpha_n^0$= $\alpha_\tau^0$= $10^{12}$ N/mm$^3$: (a) normal traction and (b) tangential traction.

Table 2.7: Material properties and model parameters for the double cantilever beam. The cohesive parameters are assumed from [1] for mode I loading conditions.

| E (N/mm$^2$) | $\nu$ | G$_{IC}$ (N/mm) | $\sigma_{max}$ (N/mm$^2$) |
|---|---|---|---|
| $10^5$ | 0.35 | 0.28 | 57 |

mesh with 0.125 mm × 1 mm rectangular elements, Fig. 2.20(a) shows that the cohesive strength effects the peak load prediction, and it is important to take the cohesive strength adequately large to ensure a better match with the analytical solution. For smaller cohesive strengths, the reduced peak load prediction is a consequence of crack initiation and propagation at smaller applied displacements. Beyond a certain value of the interface strength ($\sigma_{max} = 57$ N/mm$^2$) there is little effect from increasing the cohesive strength, as the load-displacement curve converges to the analytical solution. However, increasing the cohesive strength decreases the cohesive process zone size, so a smaller element size is required to accurately recover the crack-face traction. Fig. 2.20(b) depicts the effect of mesh size on the load-displacement response for cohesive strength $\sigma_{max} = 57$ N/mm$^2$. Choosing a coarse mesh (e.g., $h = 1$ mm) yields a noisy load-displacement curve due to inaccuracies in crack-face traction and episodic crack growth. Our study suggests that the interface element size $h = \text{meas}(\Gamma_*)$ should be chosen smaller than 0.25 mm to better capture the softening portion of the load-displacement curve. This is consistent with the guidelines described in [3] that the the cohesive process zone needs to be resolved with at least three interface elements to ensure sufficient accuracy. We next compare the normal traction profile along the cohesive interface obtained from the standard and the stabilized method at an applied displacement $\Delta = 0.67$ mm for coarse and fine meshes. In Fig. 2.21, the traction profile obtained from the standard method shows spurious oscillations, whereas that obtained from the stabilized method is free of oscillations. We also observe that the peak traction in the coarse mesh ($h = 1$ mm) is less that the cohesive strength $\sigma_{max} = 57$ N/mm$^2$, whereas that in the fine mesh ($h = 0.125$ mm) it is equal to the cohesive strength, which illustrates that a finer mesh is required to accurately capture the crack-face traction. Thus, this study demonstrates the superior stability of the Nitsche-based, stabilized method compared to the standard method.

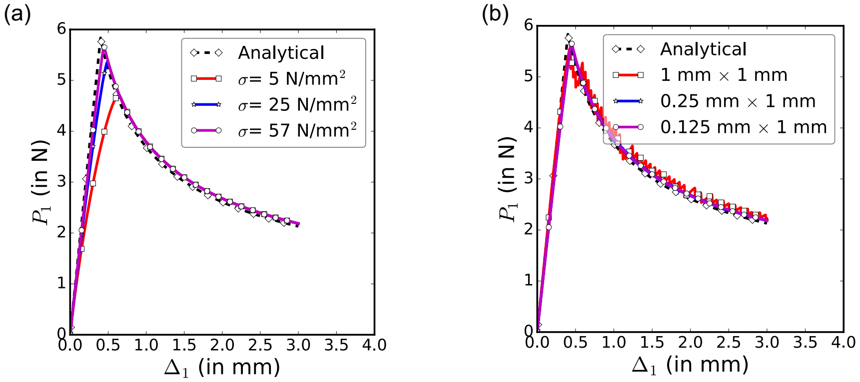

Figure 2.20: Load versus displacement curves for the symmetric double cantilever beam test: (a) different cohesive interface strength and (b) different mesh size

## 2.5 Conclusion

In this chapter, we proposed a stabilized finite element method for enforcing stiff isotropic and anisotropic cohesive laws using zero-thickness interface elements. The stabilized method generalizes Nitsche's method to cohesive fracture problems and the key advan-

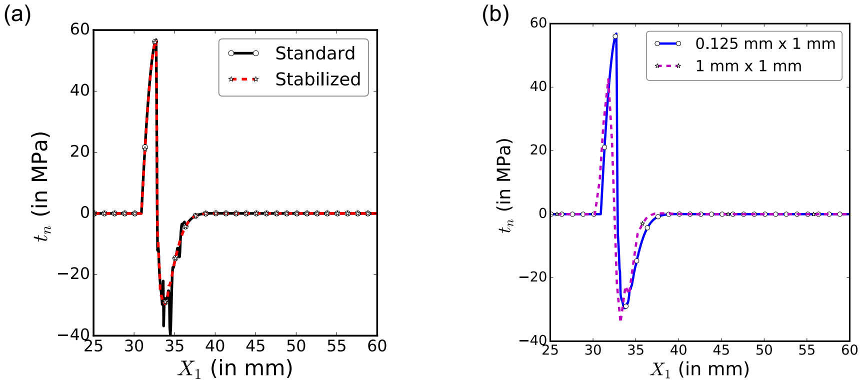

Figure 2.21: Normal traction versus interface length curves from the standard and stabilized methods for the double cantilever beam test for $\alpha_n^0$= $\alpha_\tau^0$= $10^8$ N/mm$^3$: (a) fine mesh ($h =$ 0.125 mm) and (b) coarse mesh ($h = 1$ mm).

tage is that our method remains well defined for any arbitrarily large value of cohesive stiffness. We presented several numerical examples demonstrating the stability and accuracy of the proposed method over the standard (penalty-like) method in two-dimensions. We first determined the numerical accuracy of the stabilized method in recovering crack surface traction at straight and semi-circular interfaces using constant strain patch tests. We demonstrated that the traction error in the stabilized method (measured with respect to the analytical solution for perfectly-bonded interface) approaches machine precision for large values of cohesive stiffness; whereas, the error increased in the standard method as the cohesive stiffness was increased. We next evaluated the numerical stability of the proposed method in alleviating spurious traction oscillations along the interface for stiff isotropic and anisotropic cohesive laws (i.e, with equal and unequal normal and tangential stiffnesses). Our numerical results clearly showed the presence of spurious traction oscillations in the standard method when enforcing anisotropic cohesive laws on curved interfaces under compression and sliding fracture; whereas, the stabilized method yielded oscillation-free traction profiles and ensured accurate recovery of crack surface traction, regardless of the choice of cohesive stiffness.

We next simulated mixed-mode delamination crack growth in an isotropic material using the asymmetric double cantilever beam test configuration. For stiff isotropic cohesive laws, we investigated the sensitivity of load-displacement curves predicted by the standard and stabilized methods to applied displacement increment (or load step size) and cohesive stiffness. If the displacement increment is taken small enough ($\dot{\Delta} = 0.001$ mm/step), then both the standard and stabilized methods predict the same load-displacement curve. However, for the larger cohesive stiffness and displacement increment of $\dot{\Delta} = 0.005$ mm/step, the standard method is less accurate compared to the stabilized method (see Fig. 2.17). Our results indicate that this discrepancy in the standard method potentially arises from the inaccurate prediction of crack growth behavior (see Fig. 2.18) and crack surface traction (see Fig. 2.19). In contrast, the stabilized method is sufficiently accurate in predicting peak load and crack growth even for the larger displacement increment $\dot{\Delta} = 0.005$ mm/step. Thus, this study illustrated that stabilized method can improve computational efficiency by allowing the use of larger displacement rates in mixed-mode fracture simulation. Finally, we investigated the effect of cohesive interface strength and mesh refinement on the load-displacement response using the mode I double cantilever beam test. We illustrated that the cohesive strength parameter affects the peak-load prediction and choosing a larger value ($\sigma_{max} = 57$ N/mm$^2$) ensures a better match with the linear elastic analytical solution obtained from beam theory. We also show that it is necessary to choose the interface element size small enough (according to the criteria in [52, 3]), in order to obtain accurate load-displacement curve and crack-face traction profiles. These cohesive fracture simulation studies clearly illustrate the superior stability of the proposed Nitsche-based, stabilized finite element method compared to the standard finite element method.

## Chapter 3

# ON THE ROBUSTNESS OF THE STABILIZED FINITE ELEMENT METHOD FOR DELAMINATION ANALYSIS OF COMPOSITES USING COHESIVE ELEMENTS

This chapter is adapted from "On the robustness of the stabilized finite element method for delamination analysis of composites using cohesive elements" published in *International Journal for Computational Methods in Engineering Science and Mechanics* and has been reproduced with the permission of the publisher and my co-authors Ravindra Duddu and Chandrasekhar Annavarapu : Ghosh, G., Duddu, R., and Annavarapu, C. (2021). On the robustness of the stabilized finite element method for delamination analysis of composites using cohesive elements, *International Journal for Computational Methods in Engineering Science and Mechanics*, DOI: 10.1080/15502287.2021.1896607

## 3.1 Introduction

In laminated fiber-reinforced composites, delamination is one of the most dominant failure mechanisms, which involves progressive damage accumulation and fracture along interlaminar interfaces [1]. Delamination under static and cyclic-fatigue loading has been widely studied in the literature over the past 40 years [94, 95], because it causes localized damage that is hard to detect and may lead to sudden structural collapse. The cohesive zone modeling approach has been extensively used to analyze and predict mixed-mode delamination propagation, despite its drawbacks and limitations. A particular drawback of the standard finite element implementation of cohesive zone models (CZMs) is its occasional numerical instability, which causes spurious traction oscillations at delamination/crack interface [46]. Simple engineering solutions [52] may mitigate numerical issues with the standard finite element method (FEM) on a case-by-case basis, but they are not robust and introduce parametric uncertainty [79]. We recently illustrated that a Nistche-based stabilized FEM is robust and accurate for enforcing stiff cohesive laws and simulating fracture propagation in isotropic, homogeneous elastic materials [22]. The purpose of this article is to investigate the numerical stability and accuracy of standard FEM and weighted Nitsche-based stabilized FEM for delamination analysis of composites using cohesive elements, especially at anisotropic and dissimilar interlaminar interfaces.

The cohesive zone modeling approach, which is based on continuum damage mechanics [47], has been widely used to simulate mixed-mode delamination of composites [96, 5, 97], including the growth of multiple delamination cracks extending into various ply interfaces [98, 99]. Despite its success, the standard FEM implementation of CZMs comes with certain outstanding challenges, including mesh dependence, parametric uncertainty, computational efficiency, and numerical instability. Mesh dependence of the predicted crack path or directional mesh bias can be an issue with CZMs, as cracks can only propagate along finite element edges. To allow the propagation of arbitrary cohesive cracks and/or the inclusion of intra-element cohesive interfaces, various approaches based on the partition of unity concept (including G/XFEM) or virtual/phantom nodes were proposed [100, 101, 102, 21, 103, 104, 105, 106]. The performance of the standard FEM to simulate cohesive cracks can be poor with distorted or low quality meshes, so mesh free methods were proposed to alleviate such difficulties [107]. Recently, phase-field damage models have also been proposed to simulate delamination of orthotropic laminates [108, 109].

Parametric uncertainty or sensitivity of CZMs to the choice of model parameters can affect the accuracy of delamination analysis. Depending on the choice of cohesive stiffness, cohesive/interface strength, and fracture toughness parameters, the accuracy of load and interface traction prediction can vary significantly [79, 110]. Out of these three parameters, only fracture toughness can be determined or well-constrained from experiments for a given composite material. Notably, in the case of mixed-mode delamination at dissimilar interfaces in bi-materials, fracture toughness is also dependent on the mode mixity (loading) [111]. In contrast, the cohesive strength is difficult to determine from experiments, and is usually assumed based on mesh size considerations [47, 52, 3], as a compromise between computational efficiency and numerical accuracy. The cohesive stiffness is generally regarded as a numerical penalty parameter in intrinsic CZMs that assume an initially elastic response, and in extrinsic CZMs that assume initially rigid response and elastic unloading/reloading response. The FEM implementation of extrinsic CZMs requires advanced algorithms [37, 35, 38], which increases computational complexity; whereas, intrinsic CZMs are relatively straightforward to implement within a legacy/commercial finite element code, but the choice of cohesive stiffness can affect numerical stability and/or convergence. It is noteworthy that extrinsic CZMs under fatigue and compressive loading scenarios also suffer from numerical instabilities observed in intrinsic CZMs with large values of cohesive stiffness.

In quasi-static fracture/delamination analysis, the standard FEM implementations using intrinsic CZMs can exhibit spurious traction oscillations along the cohesive interface, especially near crack tips, if a large initial cohesive stiffness is specified [54, 112, 55, 12, 113, 52, 114]. Even with potential-based intrinsic CZMs, it is important to control the elastic behavior through initial slope indicators to avoid instability [44]. Past studies indicate that using the Gaussian full integration scheme [46, 54, 1, 55] can cause spurious oscillations in the traction profile along cohesive interfaces. Although the Newton-Cotes integration scheme was suggested as an alternative, some studies reported that it can result in an odd wrinkling mode in thin laminates undergoing delamination process [115, 116, 117]. Improved cohesive stress integration schemes for continuum CZMs [118] were developed to further tackle the issues of stability and robustness. Alternatively, discrete CZMs were developed [119, 120, 48, 121] that use spring-like elements to connect the finite element nodes at delamination interfaces, instead of element edges, to alleviate numerical instability and/or convergence issues. However, in discrete CZMs, when using non-uniform meshes, or modeling interfacial kinks, relating force-displacement relations for the spring like elements with interface traction is not straightforward. The issue of numerical instability in the standard FEM implementation of intrinsic continuum CZMs, when using large cohesive stiffness and full/reduced Gauss integration schemes, arises due to ill-conditioning of discrete systems, as typical with penalty-like formulations [14]. Although Lagrange-multiplier-based mixed or two-field formulations for intrinsic/extrinsic CZMs [57, 58] can overcome numerical instability, they can be computationally expensive or cumbersome owing to the difficulty in determining a stable Lagrange multiplier space.

To broadly address the numerical instability issues with penalty-like formulations and standard FEM for interface/contact problems, discontinuous Galerkin (dG) methods or Nitsche-based methods were proposed in the last two decades [64, 11]. Several novel dG approaches were developed for fracture problems, including dG interface [122, 81, 83], space-time dG approaches [82, 123], and hybrid dG-CZM approaches [124, 125, 126, 127], where the dG method is generally used before fracture initiation and CZMs are used for simulating fracture propagation. A limitation, however, for the wider use of dG approaches for fracture is the inherent complexity associated with their implementation, especially in legacy/commercial finite element codes/software. Conversely, Nitsche methods were advocated by [17, 128] for modeling strong/weak discontinuities and elastic interface problems. Nitsche methods overcome the issue of numerical instability affecting penalty-like formulations, by adding consistency terms [66, 67]. Nitsche's method has been extended for modeling frictional-sliding on embedded interfaces [77, 19] and small-sliding contact on frictional surfaces, including stick–slip behavior [20]. Inspired by the work of [78], we recently extended the Nitsche's method to cohesive fracture problems, and developed a stabilized FEM that alleviates traction oscillations with stiff, anisotropic cohesive laws [22].

In this chapter, we illustrate the ability of the stabilized FEM of Ghosh *et al.* [22] in alleviating traction oscillations at interlaminar interfaces in multi-directional orthotropic composite laminates under different loading conditions. A specific aim is to illustrate its robustness for composite delamination analysis, with regard to the choice of the cohesive stiffness and the structure of the finite element mesh (e.g. uniform structured versus perturbed or semi-structured meshes), which has not been addressed before. The rest of this paper is organized as follows: in Section 3.2, we briefly describe the governing equations of the cohesive fracture problem and the weak forms corresponding to the standard and stabilized methods. In Section 3.3, we discuss the salient aspects of the numerical implementation and the selected model/material parameters. Specifically, we focus on the implementation via user element subroutines in commercial finite element software ABAQUS [86], so that it can be utilized by the broader composite modeling community. In Section 3.4, we present several benchmark numerical examples to compare the standard and stabilized methods, with a particular emphasis on the accuracy of the interface traction field and load–displacement curves. Finally, in Section 3.5, we conclude with a summary and closing remarks.

## 3.2 Governing Equations and Weak Formulations

In this section, we briefly review the Nitsche-inspired stabilized finite element method originally proposed in [22] for enforcing stiff cohesive laws. We will begin with a description of the strong form of the governing equations followed by the anisotropic bilinear cohesive law for mixed-mode loading. Subsequently, we will discuss the weak form for the standard and stabilized methods, and the choice of stabilization parameters and weights.

### 3.2.1 Strong Form of the Delamination/Debonding Problem

We define an initial domain $\Omega \subset \mathbb{R}^2$, which is partitioned into two non-overlapping bulk domains $\Omega^{(1)}$ and $\Omega^{(2)}$ separated by a pre-defined internal cohesive interface $\Gamma_*$, such that $\Omega = \Omega^{(1)} \cup \Omega^{(2)}$ (see Fig. 3.1). Throughout this chapter, we use the notation that numbers within parentheses in the superscript identify the domain partitions. Dirichlet and Neumann boundary conditions are enforced on two disjointed parts of the domain boundary $\Gamma \equiv \partial\Omega$ in such a way so that $\partial\Omega = \Gamma_D \cup \Gamma_N$ with $\Gamma_D \cap \Gamma_N = \emptyset$. The outward unit normal to the boundary $\partial\Omega$ is denoted by $\mathbf{n}_\mathrm{e}$ and unit normal vector associated with the interface boundary $\Gamma_*$ is denoted by $\mathbf{n}$ and points from $\Omega^{(2)}$ to $\Omega^{(1)}$ (thus $\mathbf{n} = -\mathbf{n}^{(1)} = \mathbf{n}^{(2)}$).

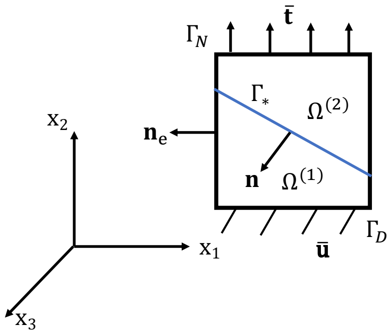

Figure 3.1: A schematic of the undeformed domain for the quasi-static delamination/debonding problem. We choose $X_1$ and $X_2$ as the in-plane coordinates for the laminate material, and $X_3$ is the out-of-plane coordinate.

For delamination and debonding at sharp interfaces, we assume the bulk domains consist of a homogeneous anisotropic linearly elastic material, thus intralaminar damage is neglected and only interlaminar damage is considered. Assuming small displacements, the Cauchy stress tensor can be defined in $\Omega^{(1)}$ and $\Omega^{(2)}$ as

$$\boldsymbol{\sigma}^{(m)} = \mathbf{D}^{(m)} : \boldsymbol{\epsilon}^{(m)}, \quad m = \{1,2\}, \tag{3.1}$$

where $\mathbf{D}$ denotes the fourth-order anisotropic elasticity tensor and the small strain tensor $\boldsymbol{\epsilon} = \frac{1}{2}(\boldsymbol{\nabla}\mathbf{u} + (\boldsymbol{\nabla}\mathbf{u})^T)$ is defined by the symmetric part of the displacement gradient tensor. The governing elasto-static equilibrium equations in the absence of body forces are given by:

$$\begin{aligned}
\boldsymbol{\nabla}\cdot\boldsymbol{\sigma}^{(m)} &= \mathbf{0} \text{ in } \Omega^{(m)}, \quad m = \{1,2\}, && (3.2)\\
\mathbf{u} &= \bar{\mathbf{u}} \text{ on } \Gamma_D, && (3.3)\\
\boldsymbol{\sigma}\cdot\mathbf{n}_\mathrm{e} &= \bar{\mathbf{t}} \text{ on } \Gamma_N, && (3.4)\\
\mathbf{t}_\mathrm{c} &= -\boldsymbol{\sigma}^{(1)}\cdot\mathbf{n}^{(1)} = \boldsymbol{\sigma}^{(2)}\cdot\mathbf{n}^{(2)} \text{ on } \Gamma_*, && (3.5)
\end{aligned}$$

where $\bar{\mathbf{u}}$ is the prescribed displacement vector on the Dirichlet boundary $\Gamma_D$ and $\bar{\mathbf{t}}$ is the prescribed traction on the Neumann boundary $\Gamma_N$. The interface traction $\mathbf{t}_\mathrm{c}$ is related to the Cauchy stress tensor evaluated in the sub-domains $\Omega^{(1)}$ and $\Omega^{(2)}$ as given by (3.5), and is continuous across the cohesive interface $\Gamma_*$ to satisfy the force equilibrium. The cohesive traction $\hat{\mathbf{t}}_\mathrm{c}$ is the Newton's third law pair to the interface traction $\mathbf{t}_\mathrm{c}$ on a given delamination/crack surface and can be defined as a function of the interface separation or displacement jump as

$$\hat{\mathbf{t}}_\mathrm{c} = -\mathbf{t}_\mathrm{c} = \boldsymbol{\alpha}(\boldsymbol{\delta})\ \boldsymbol{\delta}, \tag{3.6}$$

$$\boldsymbol{\delta} = [\![\mathbf{u}]\!] = \mathbf{u}^{(2)} - \mathbf{u}^{(1)}, \tag{3.7}$$

where the cohesive stiffness matrix $\boldsymbol{\alpha}$ is usually a nonlinear function of the interface separation.

**Remark 1** *In the case where the interlaminar interface delineates two dissimilar materials (i.e.,* $\mathbf{D}^{(1)} \neq \mathbf{D}^{(2)}$*), the Cauchy stress tensor evaluated at interface from either side can be different (i.e.,* $\boldsymbol{\sigma}^{(1)} \neq \boldsymbol{\sigma}^{(2)}$*), but the traction field must be continuous across the interface.*

### 3.2.2 Anisotropic bilinear cohesive law

We consider an intrinsic bilinear traction–separation or cohesive law that consists of an initial elastic region followed by a softening region. For mixed-mode delamination under quasi-static loading in two-dimensions, we cast the bilinear cohesive law in the damage mechanics framework as detailed in [79]. The tangential $t_\tau$ and normal $t_n$ components of the interface traction vector $\mathbf{t}_\mathrm{c}$ are related to the tangential $\delta_\tau$ and normal $\delta_n$ components of the interface separation $\boldsymbol{\delta}$ as

$$\mathbf{t}_\mathrm{c} = \begin{Bmatrix} t_\tau \\ t_n \end{Bmatrix} = -\begin{bmatrix} (1-D_s)\alpha_\tau^0 & 0 \\ 0 & \left(1 - D_s\dfrac{\langle\delta_n\rangle}{\delta_n}\right)\alpha_n^0 \end{bmatrix} \begin{Bmatrix} \delta_\tau \\ \delta_n \end{Bmatrix}, \tag{3.8}$$

where $\alpha_n^0$ and $\alpha_\tau^0$ represent the initial cohesive stiffness in the normal and the tangential directions, respectively, and the scalar damage variable $D_s$ is given by

$$D_s = \begin{cases} 0 & \text{if} \quad \delta_e < \delta_e^c, \\ \dfrac{\delta_e^u(\delta_e - \delta_e^c)}{\delta_e(\delta_e^u - \delta_e^c)} & \text{if} \quad \delta_e^c \leq \delta_e < \delta_e^u, \\ 1 & \text{if} \quad \delta_e^u \leq \delta_e, \end{cases} \tag{3.9}$$

and the equivalent separation $\delta_e = \sqrt{\langle\delta_n\rangle^2 + \delta_\tau^2}$. In the above equations, $\langle\cdot\rangle$ denotes Macaulay brackets, so that $\langle\delta_n\rangle = \max(0, \delta_n)$, which ensures that there is no damage growth or damage effect on the normal cohesive stiffness response under compression or contact. The critical and ultimate interface separation parameters $\delta_e^c$ and $\delta_e^u$, respectively, defined as [5]:

$$\frac{1}{\delta_e^c} = \sqrt{\left(\frac{\alpha_n^0 \cos I}{\sigma_{\max}}\right)^2 + \left(\frac{\alpha_\tau^0 \cos II}{\tau_{\max}}\right)^2}, \tag{3.10}$$

$$\frac{1}{\delta_e^u} = \left(\frac{\alpha_n^0 \delta_e^c (\cos I)^2}{2\, G_{IC}}\right) + \left(\frac{\alpha_\tau^0 \delta_e^c (\cos II)^2}{2\, G_{IIC}}\right), \tag{3.11}$$

where the direction cosines $\cos I = \delta_n/\delta_e$ and $\cos II = \delta_\tau/\delta_e$, $\sigma_{\max}$ and $\tau_{\max}$ are the pure mode I and mode II cohesive strengths, and $G_{IC}$ and $G_{IIC}$ are the pure mode I and mode II critical fracture energies. For illustration, the normal and tangential traction profiles as a function of the normal and tangential interface separations are shown in Fig. 2.3.

**Remark 2** *Although the anisotropic bilinear cohesive law is phenomenological, it can be related to a potential function defined as*

$$\Psi = -\frac{1}{2}\left((1 - D_s)\alpha_\tau^0 \delta_\tau^2 + \left(1 - D_s \frac{\langle\delta_n\rangle}{\delta_n}\right) \alpha_n^0 \delta_n^2\right). \tag{3.12}$$

*The crack surface traction components can be defined based on the above potential function as* $t_\tau = \dfrac{\partial \Psi}{\partial \delta_\tau}$ *and* $t_n = \dfrac{\partial \Psi}{\partial \delta_n}$. *The expressions for (3.8) are approximations obtained by neglecting the nonlinearity due to interface damage $d_s$, which is a function of the interface* *separation.*

**Remark 3** *The anisotropic bilinear cohesive law of Jiang et al. [5] has six independent parameters, namely initial cohesive stiffness, maximum cohesive strength and critical fracture energy of pure mode I and II loadings, to describe the traction-separation relationship. If these parameter values are chosen to be the same for both normal and shear modes, then we get an isotropic bilinear cohesive law with only three independent parameters.*

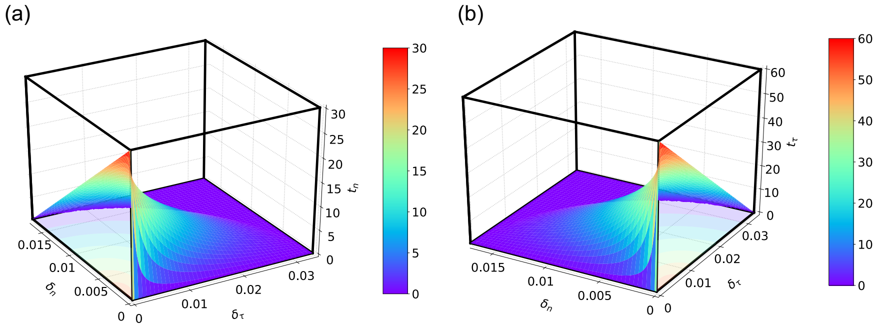

Figure 3.2: Traction-separation relations defined by the anisotropic, intrinsic bilinear cohesive law of [5]: (a) normal traction field and (b) tangential traction field.

### 3.2.3 Standard weak form

We apply the Galerkin procedure of weighted residuals to derive the standard weak form, which is detailed in [22]. By weighting the equilibrium equation in (2.2) by a test function $\mathbf{w}$, integrating by parts, applying the divergence theorem, using the traction continuity condition at the interface in (3.5), and the constitutive relation in (3.1), we obtain the weak form as:

$$\sum_{m=1}^{2} \int_{\Omega^{(m)}} \nabla^{s}\mathbf{w}^{(m)} : \mathbf{D}^{(m)} : \nabla^{s}\mathbf{u}^{(m)} \, d\Omega - \int_{\Gamma_*} [\![\mathbf{w}]\!] \cdot \mathbf{t}_c \, d\Gamma = \int_{\Gamma_N} \mathbf{w} \cdot \bar{\mathbf{t}} \, d\Gamma, \tag{3.13}$$

where the jump in the test function is defined as $[\![\mathbf{w}]\!] = \mathbf{w}^{(2)} - \mathbf{w}^{(1)}$. Substituting the traction-separation relation in (2.8) into the weak form in (3.13) we obtain the standard weak form as

$$\sum_{m=1}^{2} \int_{\Omega^{(m)}} \nabla^{\mathrm{s}} \mathbf{w}^{(m)} : \mathbf{D}^{(m)} : \nabla^{\mathrm{s}} \mathbf{u}^{(m)} \, \mathrm{d}\Omega + \int_{\Gamma_*} [\![\mathbf{w}]\!] \cdot \, \boldsymbol{\alpha}(\boldsymbol{\delta}) \, \boldsymbol{\delta} \, \mathrm{d}\Gamma = \int_{\Gamma_N} \mathbf{w} \cdot \bar{\mathbf{t}} \, \mathrm{d}\Gamma. \tag{3.14}$$

Because the cohesive traction and separation components are defined in the normal and tangential directions, the standard weak form is implemented as,

$$\sum_{m=1}^{2} \int_{\Omega^{(m)}} \nabla^{\mathrm{s}} \mathbf{w}^{(m)} : \mathbf{D}^{(m)} : \nabla^{\mathrm{s}} \mathbf{u}^{(m)} \, \mathrm{d}\Omega + \int_{\Gamma_*} (1 - D_s) \left( [\![w_n]\!] \alpha_n^0 \delta_n + [\![w_\tau]\!] \alpha_\tau^0 \delta_\tau \right) \, \mathrm{d}\Gamma = \int_{\Gamma_N} \mathbf{w} \cdot \bar{\mathbf{t}} \, \mathrm{d}\Gamma. \tag{3.15}$$

Thus, in the standard weak formulation, the cohesive traction is simply enforced as a mixed boundary condition on the interface.

**Remark 4** *If the initial cohesive stiffness parameters $\alpha_n^0$ and $\alpha_\tau^0$ are taken to be large enough, the standard weak form resembles the penalty method for enforcing displacement continuity across the interface. However, for stiff cohesive laws, where cohesive stiffness is several orders of magnitude greater than the elastic modulus, the standard weak form becomes ill-conditioned leading to numerical instability and/or convergence issues. In the limiting case of a non-interpenetration (contact) constraint or an extrinsic cohesive law, where $\alpha_n^0 \to \infty$ and/or $\alpha_\tau^0 \to \infty$, the standard weak form is not well defined.*

### 3.2.4 Stabilized weak form

The stabilized FEM developed in [22] extended Nitsche's method [78, 73] to cohesive fracture problems, which we review here for the sake of clarity. The key idea is to evaluate the interface traction in terms of a weighted average stress in the bulk material across the interface and the traction in the cohesive interface as

$$\mathbf{t}_{\mathrm{c}} = (\mathbf{I} - \mathbf{S}) \langle \boldsymbol{\sigma} \rangle_{\gamma} \cdot \mathbf{n} - \mathbf{S} \boldsymbol{\alpha} \, \boldsymbol{\delta}, \tag{3.16}$$

where **I** is the second-order identity matrix, **S** is the stabilization matrix defined as,

$$\mathbf{S} = \begin{bmatrix} \dfrac{\beta_\tau}{\alpha_\tau^0(1-D_s)+\beta_\tau} & 0 \\ 0 & \dfrac{\beta_n}{\alpha_n^0(1-D_s)+\beta_n} \end{bmatrix}, \tag{3.17}$$

$\beta_\tau, \beta_n$ are the stabilization parameters, and $\langle \boldsymbol{\sigma} \rangle_\gamma$ is the weighted average of the stress tensors on both sides of the interface defined as

$$\langle \boldsymbol{\sigma} \rangle_\gamma = (\gamma^{(1)}\boldsymbol{\sigma}^{(1)} + \gamma^{(2)}\boldsymbol{\sigma}^{(2)}) \ \forall \ \gamma^{(1)} + \gamma^{(2)} = 1, \ \ \gamma^{(1)} > 0, \ \ \gamma^{(2)} > 0. \tag{3.18}$$

Substituting (2.29) into the weak form in (3.13) we obtained the stabilized weak form as

$$\sum_{m=1}^{2} \int_{\Omega^{(m)}} \nabla^{\mathrm{s}}\mathbf{w}^{(m)} : \mathbf{D}^{(m)} : \nabla^{\mathrm{s}}\mathbf{u}^{(m)} \,\mathrm{d}\Omega - \int_{\Gamma_*} [\![\mathbf{w}]\!] \cdot (\mathbf{I}-\mathbf{S}) \langle \boldsymbol{\sigma} \rangle_\gamma \cdot \mathbf{n} \,\mathrm{d}\Gamma \\ + \int_{\Gamma_*} [\![\mathbf{w}]\!] \cdot \mathbf{S}\alpha(\delta)\, \delta \,\mathrm{d}\Gamma = \int_{\Gamma_N} \mathbf{w} \cdot \bar{\mathbf{t}} \,\mathrm{d}\Gamma. \tag{3.19}$$

In the above equation, the second and third terms on the left hand side ensure consistency and stability, respectively. If the stabilization matrix is taken as the identity matrix, then the stabilized weak form in (2.26) becomes identical to the standard weak form in (2.15).

**Remark 5** *The stabilized method presented here is unsymmetric and resembles the incomplete interior penalty method [65, 84]. It can be proved that the displacement solution* **u** *of the strong form equations (2.2) – (3.5) is satisfied by the solution to the weak form equation (2.26), which establishes consistency for any value of cohesive stiffness; the mathematical procedure for proving this is similar to that described in [78, Lemma 2.1].*

The stabilized weak form with the interface traction and separation components expressed in the normal and tangential coordinates is given by

$$\sum_{m=1}^{2} \int_{\Omega^{(m)}} \nabla^{s}\mathbf{w}^{(m)} : \mathbf{D}^{(m)} : \nabla^{s}\mathbf{u}^{(m)} \, \mathrm{d}\Omega \; - \int_{\Gamma_*} [\![\mathbf{w}]\!] \cdot (\mathbf{I} - \mathbf{S}) \, \langle \boldsymbol{\sigma} \rangle_{\gamma} \cdot \mathbf{n} \, \mathrm{d}\Gamma$$

$$+ \int_{\Gamma_*} \left( [\![w_n]\!] \frac{(1-D_s)\alpha_n^0 \beta_n}{\alpha_n^0 (1-D_s) + \beta_n} \delta_n + [\![w_\tau]\!] \frac{(1-D_s)\alpha_\tau^0 \beta_\tau}{\alpha_\tau^0 (1-D_s) + \beta_\tau} \delta_\tau \right) \mathrm{d}\Gamma = \int_{\Gamma_N} \mathbf{w} \cdot \bar{\mathbf{t}} \, \mathrm{d}\Gamma. \quad (3.20)$$

**Remark 6** *As $(1-D_s)\alpha_n^0, (1-D_s)\alpha_\tau^0 \to \infty$, the stabilized weak form in (3.20) resembles the Nitsche stabilized finite element method for frictional contact presented in [19]. Thus, the stabilized weak form remains well-defined in the limiting case of a non-interpenetration (contact) constraint or an extrinsic cohesive law, unlike the standard weak form in (2.16).*

### 3.2.5 Choice of stabilization parameters and weight factor

The stabilization parameters $\beta_\tau, \beta_n$ and the weights $\gamma^{(1)}, \gamma^{(2)}$ play a key role in the numerical performance of a Nitsche-based stabilized FEM [18]. For instance, taking a small value for the stabilization parameters may undermine the positive definiteness of the global linear system of equations; whereas, taking a large value for the stabilization parameters will essentially lead to a penalty-like method for enforcing the interface constraints [74]. Moreover, taking equal weights for dissimilar material interfaces may hamper numerical performance, or may not alleviate traction field oscillations. For constant strain triangular and tetrahedral elements, Annavarapu et al. [18] provided estimates for the stabilization parameters using a local coercivity analysis as given by

$$\beta_n = \beta_\tau = 2 \left( \frac{|\mathbf{D}^{(1)}| (\gamma^{(1)})^2}{\mathrm{meas}(\Omega^{(1)})} + \frac{|\mathbf{D}^{(2)}| (\gamma^{(2)})^2}{\mathrm{meas}(\Omega^{(2)})} \right) \mathrm{meas}(\Gamma_*). \quad (3.21)$$

Here, we simply use the above estimate of stabilization parameters for bilinear quadrilateral finite elements and conduct parametric sensitivity studies to illustrate their adequacy. Equation (3.21) establishes a functional dependency between the stabilization parameter and interface weights, and the weights are chosen so that it minimizes the stabilization parameter while ensuring coercivity. Here, we simply use expression for interface weights derived in [18]:

$$\gamma^{(1)} = \frac{\dfrac{\text{meas}(\Omega^{(1)})}{|\mathbf{D}^{(1)}|}}{\dfrac{\text{meas}(\Omega^{(1)})}{|\mathbf{D}^{(1)}|} + \dfrac{\text{meas}(\Omega^{(2)})}{|\mathbf{D}^{(2)}|}}; \gamma^{(2)} = 1 - \gamma^{(1)}, \tag{3.22}$$

where $|\mathbf{D}|$ denotes the two-norm of the elasticity tensor, $\text{meas}(\Omega)$ denotes the area of neighboring bulk element in 2D, and $\text{meas}(\Gamma_*)$ is the length of the interface element.

**Remark 7** *For the weak form in* (2.26)*, precise estimates for the stabilization parameter can be derived for constant strain elements following the procedure described in [18]. For higher-order elements, closed-form analytical estimates for the stabilization parameters are yet to be derived. However, the stabilization parameters can be specified by solving a local eigenvalue problem [129].*

## 3.3 Numerical Implementation and Model Parameters

We implemented the stabilized FEM in the commercial software ABAQUS through user-defined subroutines. In this section, we briefly present key details of ABAQUS implementation and list the model parameters that are specific to delamination analysis. The full details of the numerical implementation (omitted here), including the finite element approximation, discretization and linearization of the standard and stabilized weak forms, and the expressions for continuum and interface element force vectors and matrices can be found in [22].

### 3.3.1 ABAQUS Implementation

We use bilinear quadrilateral four-noded plane stress continuum elements with four-point Gauss integration scheme and four-noded linear zero-thickness interface elements with two-point Gauss integration scheme. Although our method can be implemented in 3-D, we use the 2D plane stress approximation as it has been extensively used in prior studies and has been validated with experimental data [3, 97, 44, 81]. We chose the finite element mesh and interface element size so that there are at least three interface elements within the estimated cohesive process zone; this is necessary for an accurate representation of the numerical stress distribution within the process zone at the point of initial crack propagation, as elaborated in [3]. User-element subroutines in ABAQUS typically require the user to provide the stiffness matrix (AMATRX) and the right hand side (RHS) force vector. In our implementation, we utilize the UELMAT subroutine to provide the continuum element force vector and stiffness matrix, and the UEL subroutine to provide the cohesive element force vector and stiffness matrix. The UELMAT subroutine allows the user to access some of the inbuilt material models through utility subroutines `MATERIAL_LIB_MECH`, unlike the UMAT subroutine. Using global modules, we store and share the stress and shape function derivative matrices calculated in the UELMAT subroutine to the UEL subroutine for computing interface force vector and stiffness matrix. A detailed description of these computations can be found in [22] for isotropic elasticity; whereas, here we use anisotropic elasticity for composites. For the sake of verification or comparison in some simulation studies, we used ABAQUS in-built 4-noded 2D cohesive elements (COH2D4) along with 4-noded plane stress 2D continuum elements (CPS4).

### 3.3.2 Secant stiffness and convergence

The anisotropic bilinear cohesive law described in Section 4.2.2 is highly nonlinear, because the scalar damage variable is a complex nonlinear function of the normal and tangential separations. The consistent tangent stiffness corresponding to this cohesive law can be derived from (3.8) as

$$\mathbf{K}^{\text{tan}} = -\begin{bmatrix} \dfrac{\partial t_\tau}{\partial \delta_\tau} & \dfrac{\partial t_\tau}{\partial \delta_n} \\ \dfrac{\partial t_n}{\partial \delta_\tau} & \dfrac{\partial t_n}{\partial \delta_n} \end{bmatrix} = \begin{bmatrix} (1-D_s)\alpha_\tau^0 - \alpha_\tau^0 \delta_\tau \dfrac{\partial d_s}{\partial \delta_\tau} & -\alpha_\tau^0 \delta_\tau \dfrac{\partial d_s}{\partial \delta_n} \\ -\alpha_n^0 \delta_n \dfrac{\langle \delta_n \rangle}{\delta_n} \dfrac{\partial d_s}{\partial \delta_\tau} & \left(1 - D_s \dfrac{\langle \delta_n \rangle}{\delta_n}\right) \alpha_n^0 - \alpha_n^0 \delta_n \dfrac{\langle \delta_n \rangle}{\delta_n} \dfrac{\partial d_s}{\partial \delta_n} \end{bmatrix}, \tag{3.23}$$

Deriving and implementing a closed-form expression of the above consistent tangent is arduous, and using it can cause numerical issues, as the diagonal terms become negative in the softening portion of the cohesive law. In our previous work [48, 80, 79], we argued that the secant stiffness is more advantageous with this cohesive law and demonstrated its accuracy and convergence with an implicit scheme. The simpler secant stiffness matrix can be derived from (3.8) as

$$\mathbf{K}^{\text{sec}} = \begin{bmatrix} (1-D_s)\alpha_\tau^0 & 0 \\ 0 & \left(1 - D_s \dfrac{\langle \delta_n \rangle}{\delta_n}\right) \alpha_n^0 \end{bmatrix}, \tag{3.24}$$

Although we include the simple, linearized secant stiffness terms in the AMATRX defined in the UEL subroutine, the nonlinearity of the cohesive fracture problem is handled in ABAQUS/Stan-dard outside of the user subroutines. As detailed in the user manual [86, Chapter 7: Analysis Solution and Control], ABAQUS/Standard combines incremental and iterative (Newton-Raphson) procedures for solving nonlinear problems. Using the secant stiffness necessitates smaller load/disp-lacement increments (pseudo-time steps) to gradually reach the final applied load/displacement. The user typically suggests the maximum and minimum increment size and the size of the first increment, and ABAQUS/Standard automatically chooses the size of the subsequent increments. Within each increment, ABAQUS/Standard automatically performs iteration to find an equilibrium solution based on a user-defined criteria for residual force and displacement correction. In all of our simulations, we use sufficiently small increment size that most displacement steps converge in a single iteration, except at certain time steps where more than one cohesive element fails. Also, in cohesive fracture simulations, the ABAQUS/Standard default criteria for residual force tolerance may be too small that numerical convergence may not be attainable as cohesive elements fail. Especially, using the secant stiffness it becomes necessary to increase these tolerances appropriately (sometimes by two orders of magnitude than the default value) to attain convergence. Therefore, we compare the predicted load–displacement curves against analytical solutions, experimental data, other numerical model results to ensure the accuracy of our simulations.

### 3.3.3 Bulk material Properties

We consider HTA/6376C unidirectional carbon-fiber-reinforced epoxy laminate as the generic composite material. Here, we only consider delamination or debonding along 2D straight interfaces between two HTA/6376C lamina with the fibers aligned either in the $X_1$ (in-plane horizontal) or $X_3$ (out-of-plane) direction, as indicated in Figure 2.2. According to the standard notation used to define stacking sequences in multi-ply composites laminates [130], "[0/0]" laminate denotes the two-ply specimen with fibers in the top and bottom lamina oriented in $X_1$ direction. Similarly, "[0/90]" laminate denotes the cross-ply specimen with the fibers in the top lamina oriented in the $X_1$ direction and fibers in the bottom lamina oriented in the $X_3$ direction. Usually, this notation implies that each laminate layer has the same thickness and made of the same composite material (HTA/6376C in our study). Unfortunately, experimental data from delamination tests is only available for [0/0] laminates. The anisotropic (transversely isotropic) linear elastic material properties for the 0° ply HTA/6376C laminate are listed in Table 3.1, which is directly obtained from experiments [2]. Using coordinate transformation relations we can easily obtain these material properties for the 90° ply HTA/6376C laminate.

Table 3.1: Material properties of carbon fiber/epoxy laminated composite HTA/6376C obtained from [2]

| $E_{11}$ (N/mm$^2$) | $E_{22} = E_{33}$ (N/mm$^2$) | $G_{12} = G_{13}$ (N/mm$^2$) | $G_{23}$ (N/mm$^2$) | $\nu_{12} = \nu_{13}$ | $\nu_{23}$ |
|---|---|---|---|---|---|
| $1.2 \times 10^5$ | $1.05 \times 10^4$ | $5.52 \times 10^3$ | $3.48 \times 10^3$ | 0.3 | 0.51 |

### 3.3.4 Cohesive zone model parameters

The CZM parameters chosen in our simulation studies are listed in Table 3.2. The mode I and mode II fracture energies for the 0° ply HTA/6376C laminate are taken from [2]. For ensuring the accuracy and convergence of delamination analysis using the FEM with cohesive elements, two conditions must be satisfied [52]: (1) the element size must be less than the cohesive (process) zone length, which is determined by fracture toughness and cohesive strength; and (2) the cohesive stiffness must be large enough to avoid the introduction of artificial compliance. The cohesive strength is often chosen based on cohesive zone length and mesh size considerations [see Eq. (7) in Ref. 3], owing to computational cost or limitations. Choosing a small cohesive strength may yield a poor peak load prediction, but beyond a certain value choosing a larger cohesive strength will not improve model fit with the load–displacement data from quasi-static delamination tests, but will severely restrict the mesh size and increase computational cost. Here, we use the cohesive strength values suggested in [3] to ensure numerical accuracy and efficiency. Due to the unavailability of experimental data for the 90° ply HTA/6376C laminate, we assume the same CZM parameters listed in Table 3.2.

The cohesive stiffness is generally considered to be a penalty parameter and various guidelines have been proposed in the literature for selecting the stiffness. Although the purpose of the cohesive stiffness in intrinsic/extrinsic cohesive zone models is to account for the elastic loading, unloading and reloading response of the fracture/delamination interface, it can contribute to the global deformation response and introduce artificial compliance or numerical instability issues. Based on 1D laminate model, the cohesive stiffness necessary to avoid artificial compliance issue can be estimated as [52]

$$\alpha^0 = E\,M/t, \tag{3.25}$$

where $E$ is the Young's modulus of the material along the laminate thickness direction, $t$ is the sub-laminate thickness , and $M$ is a non-dimensional number that is to be chosen much larger than one. For cohesive interfaces in non-laminates $t$ is not defined, so in (3.25) it can be replaced by a certain length measure $h$ of the bulk material [51] or the finite element mesh size. Taking $M = 100$, $E = E_{22} = 1.05 \times 10^4$ N/mm$^2$ and $t = 1.55$ mm for the delamination tests (see Section 3.4), we estimate $\alpha^0 \approx 10^6$ N/mm$^3$. To demonstrate the performance of the standard and stabilized methods, we assume three values of cohesive stiffness in our studies, including values that are two orders of magnitude smaller and larger than the above estimate. However, we note that for thin-ply laminates with $t < 0.1$ mm or for small values of length measure $h < 0.1$ mm in non-laminates, the estimated cohesive stiffness $\alpha^0 > 10^7$ N/mm$^3$.

Table 3.2: Cohesive zone model parameters for the carbon fiber/epoxy laminated composite HTA/6376C are taken from [3], except the cohesive stiffness values.

| $\alpha_n^0$ (N/mm$^3$) | $\alpha_\tau^0$ (N/mm$^3$) | G$_{IC}$ (N/mm) | G$_{IIC}$ (N/mm) | $\sigma_{\max}$ (N/mm$^2$) | $\tau_{\max}$ (N/mm$^2$) |
|---|---|---|---|---|---|
| $\{10^4, 10^6, 10^8\}$ | $\{10^4, 10^6, 10^8\}$ | 0.26 | 1.002 | 30 | 60 |

## 3.4 Numerical Examples

In this section, we present several examples to demonstrate the ability of the Nitsche-inspired stabilized formulation in alleviating oscillations in interface traction using constant strain patch tests, and pure mode I, mode II and mixed mode delamination tests. Through these tests, we specifically examine numerical stability at similar and dissimilar laminate interfaces defined by anisotropic and isotropic cohesive laws using perturbed, structured and unstructured meshes.

### 3.4.1 Patch Tests

We assess the ability of the standard and stabilized formulations in alleviating traction oscillations at horizontal and inclined straight interfaces using the constant strain patch test. Under compressive loading, we assume a stiff elastic response in the normal direction to enforce contact and a weak elastic sliding response in the tangential direction, which is captured by the anisotropic CZM. We assign the square plate with a side length $L = 1$ mm and the horizontal delamination interface at mid-height. To apply the compressive load, we constrain both vertical and horizontal displacements at the bottom edge of the plate, and prescribe a uniform vertical displacement $\Delta = -0.1$ mm at the top edge of the plate. We specify traction-free conditions at the left and right edges of the square plate. The cohesive parameters and material properties assumed for this test are listed in Tables 2.7 and 3.2, respectively.

#### 3.4.1.1 Square Plate with Horizontal Interface

To examine mesh sensitivity, we generate a $10 \times 10$ structured square mesh with element length of 0.1 mm (Fig. 3.3a) and perturb the interface nodes by $\approx 3\%$ of the element length (Fig. 3.3b). In Fig. 3.4, we show the normal traction profile versus the horizontal coordinate along the [0/0] laminate interface obtained from the standard and stabilized methods. We consider high stiffness-contrast with the anisotropic CZM, where $\alpha_n^0 = 10^8$ N/mm$^3$ and $\alpha_\tau^0 = 10^1$ N/mm$^3$. According to (3.21), we take the stabilization parameters $\beta_n = \beta_\tau = 3 \times 10^6$ N/mm$^3$. As shown in Fig. 3.4a, if the interface is perfectly flat, then both standard and stabilized methods yield smooth traction profiles without any spurious oscillations. However, we note that the standard FEM exhibits spurious traction oscillations even with the unperturbed mesh, if the normal stiffness $\alpha_n^0 = \alpha_\tau^0 \geq 10^{11}$ N/mm$^3$ (results not shown here). From Fig. 3.4b, we can see that the standard FEM suffers from severe numerical instability even with a slightly perturbed interface mesh, as evident from the large amplitude traction oscillations. In contrast, our stabilized FEM is stable and alleviates traction oscillations for anisotropic CZMs with high stiffness contrast between normal and tangential directions.

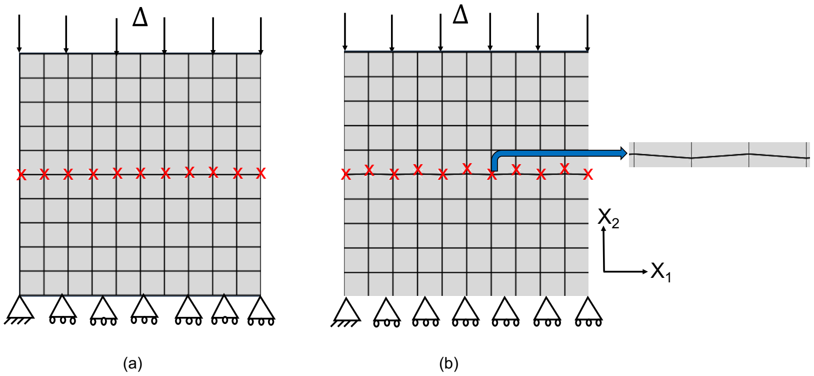

Figure 3.3: Boundary conditions and mesh used for the square plate with horizontal interface: (a) straight interface; (b) perturbed interface. The nodes are perturbed by ≈ 3% of the element size and a zoom of the interface undulations is shown in the inset.

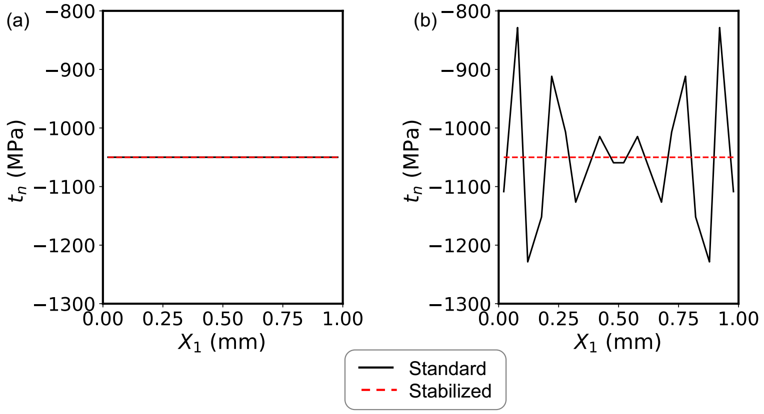

Figure 3.4: Traction profiles obtained from the standard and stabilized methods with the anisotropic CZM ($\alpha_n^0 = 10^8$ and $\alpha_\tau^0 = 10^1$ N/mm$^3$) for the square plate made of [0/0] laminate: (a) horizontal interface (b) perturbed interface.

#### 3.4.1.2 Square Plate with Inclined Interface

We consider a straight interface inclined at an initial angle of 140.4° with the horizontal $X_1$ axis embedded within the square plate of side length $L = 1$ mm (Fig. 3.5a). We discretize the domain using a $13 \times 18$ semi-structured mesh with quadrilateral element, so that the interface is divided into 13 elements (Fig. 3.5b). According to (3.21), we take the stabilization parameters $\beta_n = \beta_\tau = 5 \times 10^6, 3 \times 10^5$ N/mm$^3$ for [0/0] and [0/90] laminate interfaces, respectively. We consider the anisotropic CZM with high stiffness contrast, where $\alpha_n^0$= $10^8$ N/mm$^3$ and $\alpha_\tau^0$= $10^1$ N/mm$^3$. In Fig. 3.6, we show the normal traction profile versus the horizontal $X_1$ coordinate of the integration points along the inclined interface for [0/0] and [0/90] laminates obtained from the standard and stabilized methods. While the standard FEM exhibits instability evident from the large amplitude traction oscillations, the stabilized FEM is able to alleviate oscillations and yields a smooth traction profile. This study illustrates the drawback of the standard formulation for semi-structured meshes and potentially unstructured meshes when using anisotropic CZMs with high stiffness contrast. Overall, the two patch tests highlight the robustness of our stabilized FEM, but in the following sections we will investigate its performance for benchmark delamination tests.

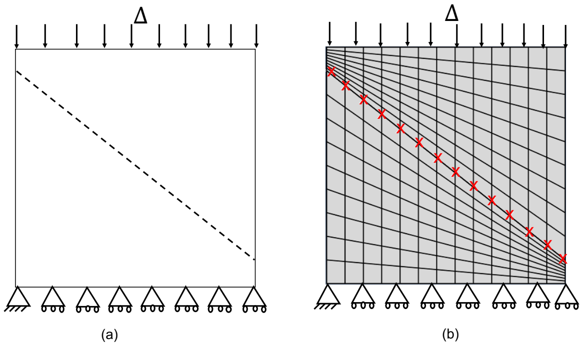

Figure 3.5: Boundary conditions and mesh used for the square plate with inclined interface: (a) schematic diagram; (b) structured finite element mesh with quadrilateral (non-rectangular) elements.

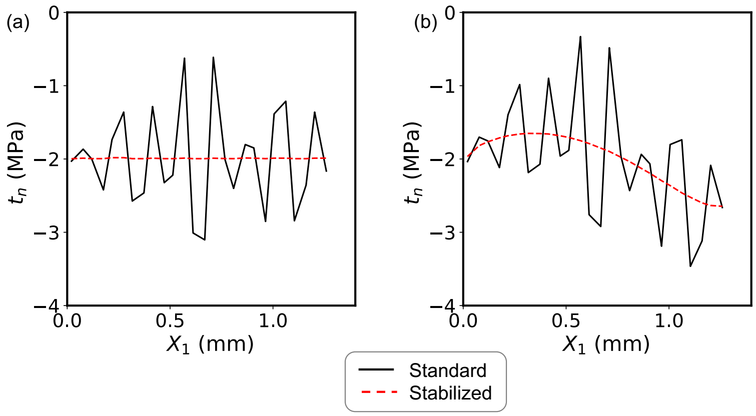

Figure 3.6: Traction profiles obtained from the standard and stabilized methods with the anisotropic CZM ($\alpha_n^0 = 10^8$ and $\alpha_\tau^0 = 10^1$ N/mm$^3$) for the square plate with an inclined interface: (a) [0/0] laminate (b) [0/90] laminate.

### 3.4.2 Double Cantilever Beam Test

We investigate the ability of the stabilized FEM in recovering oscillation-free interface traction during mode-I delamination crack growth, using the double cantilever beam (DCB) test. The specimen geometry and test set-up along with the finite element mesh are shown in Fig. 3.7. To initiate the delamination process, a pre-crack is placed at the left end of the beam, and equal and opposite vertical displacements ($\Delta$) are applied on the upper and lower nodes. The corresponding load (P) is determined from the simulation using the reaction force at the corresponding node. The fixed boundary condition is applied at the right end of the beam.

In Fig. 3.8(a), we compare the load–displacement curves obtained from the stabilized formulation for [0/0] laminate with experimental data from [131], to check that our choice of strength and displacement increment is appropriate and to determine the sensitivity to cohesive stiffness. Evidently, there is good agreement between the numerically predicted load-displacement response and the experimental data. The slight mismatch in the predicted peak load and the initial slope of the load–displacement curves is plausibly due to the idealization of boundary and loading conditions in the model, compared to the experimental test setup. In Fig. 3.8(b), we compare the load–displacement curves obtained from the stabilized FEM for [0/90] laminate with those obtained from ABAQUS inbuilt cohesive elements [86], as experimental data is unavailable. The perfect match of load–displacement curves obtained with our user-defined and ABAQUS inbuilt (COH2D4) elements verifies the correctness of our implementation. The load–displacement curves obtained from the standard FEM exactly match with those from the stabilized FEM, so we do not show them here. As the two methods differ primarily in their ability to recover interface traction fields, we examine traction fields along the delamination interfaces obtained from standard and stabilized methods for [0/0] and [0/90] laminates.

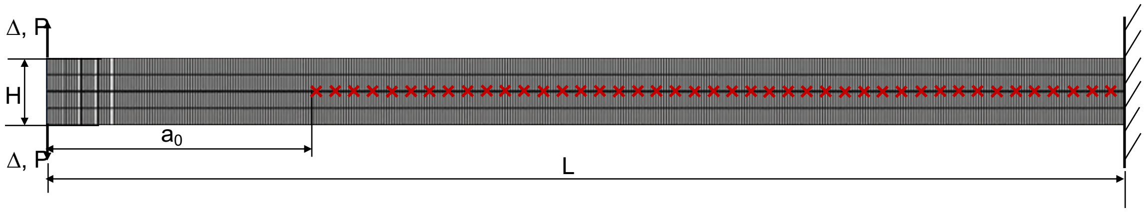

Figure 3.7: Geometry and boundary conditions for the double cantilever beam test. The dimensions are: L = 150 mm, H = 3.1 mm and $a_0$ = 35 mm.

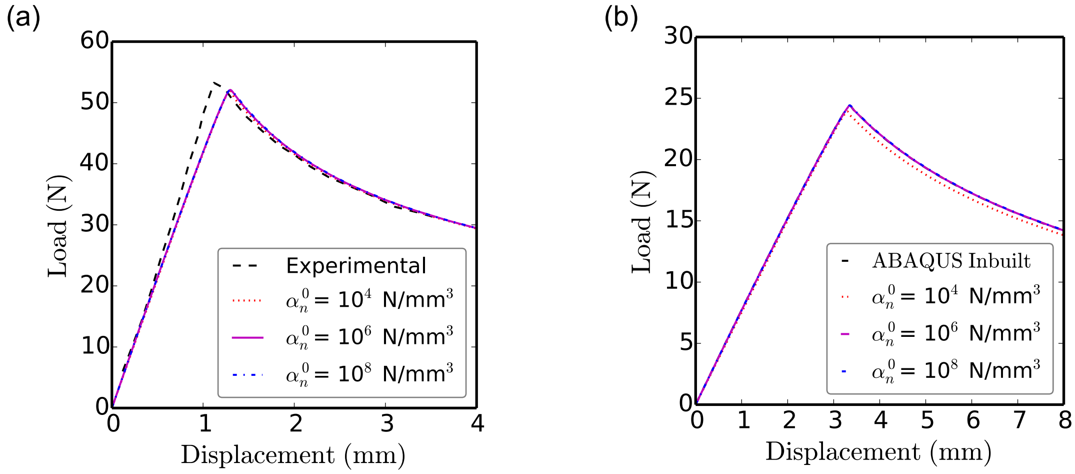

Figure 3.8: Load versus displacement curves for the double cantilever beam test obtained from the stabilized FEM: (a) [0/0] laminate and (b) [0/90] laminate.

#### 3.4.2.1 Traction at [0/0] Laminate Interface

From Fig. 3.9a, we find that for smaller values of stiffness $\alpha_n^0 = 10^4, 10^6$ N/mm$^3$ the normal traction profile from the standard FEM is smooth, but for the larger value of $\alpha_n^0 = 10^8$ N/mm$^3$ significant oscillations are observed in the traction profile. From Fig. 3.9b, it is evident that the stabilized FEM is able to alleviate traction oscillations for the large value of cohesive stiffness. We also notice that the location of the region of traction oscillations (i.e. $X_1 \approx 44$ mm) coincides with the transition from tensile to compressive normal traction. To further examine the effect of this instability on interface damage, we plotted the respective damage profiles obtained from both methods in Figs. 3.9c and 3.9d. For $\alpha_n^0 = 10^8$ N/mm$^3$ at the location of traction oscillations, we also find an oscillation in the damage profile with the standard FEM; whereas, there is no such oscillation in the damage profile with the stabilized FEM. This study shows evidence of instability with the standard FEM even with a perfectly flat interface and structured rectangular mesh.

We next examine the interface traction along the delamination interface recovered with a perturbed rectangular mesh, where we change the coordinates of interface nodes by $\approx 3\%$ of the element length. In Fig. 3.10a and 3.10b, we show the normal traction profiles obtained from the standard FEM and a zoomed-in image showing evidence of spurious oscillations in the compression region of the traction. From Fig. 3.10c it is evident that the stabilized FEM is able to alleviate the traction oscillations. This study demonstrates that numerical instability with the standard FEM is more pronounced under contact conditions (i.e. in the regions where the normal traction is negative) when using perturbed or unstructured finite element meshes, although the amplitude of the spurious oscillations in the mode I DCB test is generally small.

#### 3.4.2.2 Traction at [0/90] laminate interface

We now compare the interface traction fields recovered from standard and stabilized methods at dissimilar material interfaces. Recall that the 0° laminate exhibits anisotropic

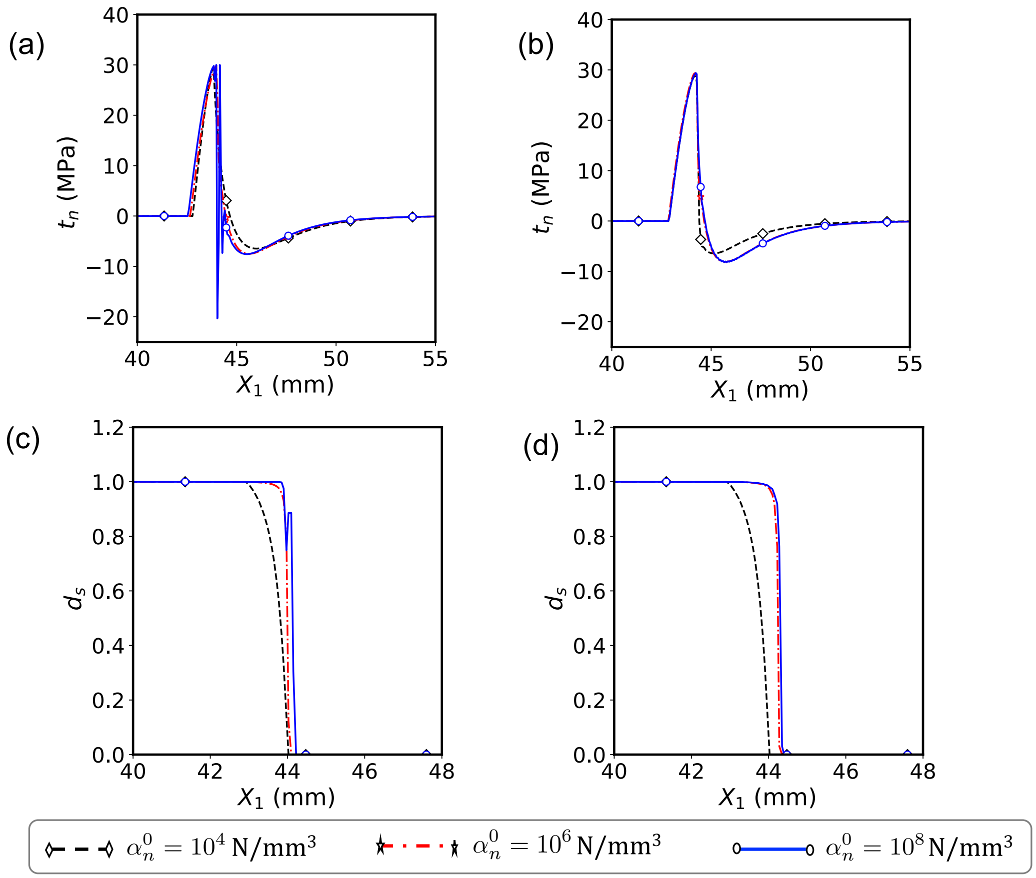

Figure 3.9: Normal traction and damage versus interface length curves from the double cantilever beam test ([0/0] ply orientation) for different cohesive stiffness values: (a), (c) standard FEM and (b), (d) stabilized FEM.

material behavior in the $X_1$ and $X_2$ plane; whereas, the 90° laminate exhibits isotropic material behavior in this plane with an order of magnitude contrast in elastic modulus ($E_{11}/E_{22} = 11.4$). In Fig. 3.11, we show the normal traction along the delamination interface recovered from the standard and stabilized methods for different values of initial cohesive stiffness. We do find a minor oscillation in normal traction and damage profiles in Figs. 3.11a and 3.11c with the standard FEM for $\alpha_n^0 = 10^8$ N/mm$^3$, which is not the case with the stabilized FEM. Notably, there are minor differences in the traction and damage curves for different stiffness values, unless stiffness is taken greater than $10^8$ N/mm$^3$.

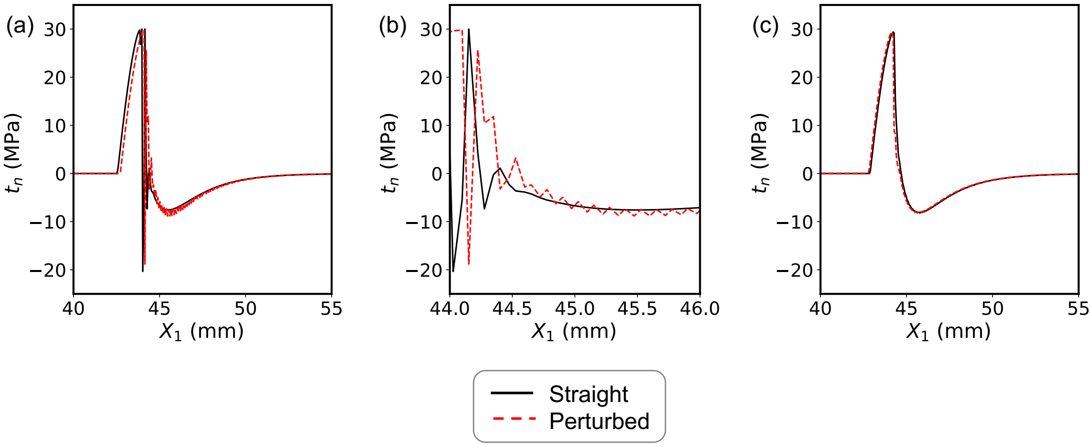

Figure 3.10: Normal traction versus interface length for $\alpha_n^0 = 10^8$ N/mm$^3$ obtained from DCB test ([0/0] ply orientation): (a) standard FEM, (b) zoom in of standard FEM near the crack tip and (c) stabilized FEM.

### 3.4.3 End Notch Flexure Test

We investigate the ability of the stabilized FEM in recovering oscillation-free interface traction during mode-II delamination crack growth, using the end notch flexure (ENF) test. The specimen geometry and test set-up are shown along with the finite element mesh in Fig. 3.12. To initiate the delamination process, a pre-crack is placed at the left end of the beam and downward vertical displacement is applied at the middle of the simply supported beam. In Fig. 3.13(a), we compare the load–displacement curves obtained from the stabilized FEM for [0/0] laminate specimen along with the experimental data and the corrected beam theory solution from [3] for different values of cohesive stiffness. In Fig. 3.13(b), we compare the load–displacement curves obtained from the stabilized FEM for [0/90] laminate with those obtained from ABAQUS inbuilt cohesive elements [86], due to the unavailability of experimental data or analytical solutions. The good match of load–displacement curves, including the predicted peak load, obtained with our user-defined and ABAQUS inbuilt (COH2D4) elements verifies the correctness of our implementation. The load–displacement curves obtained from the standard FEM exactly match with those from the stabilized FEM, so we do not show them here.

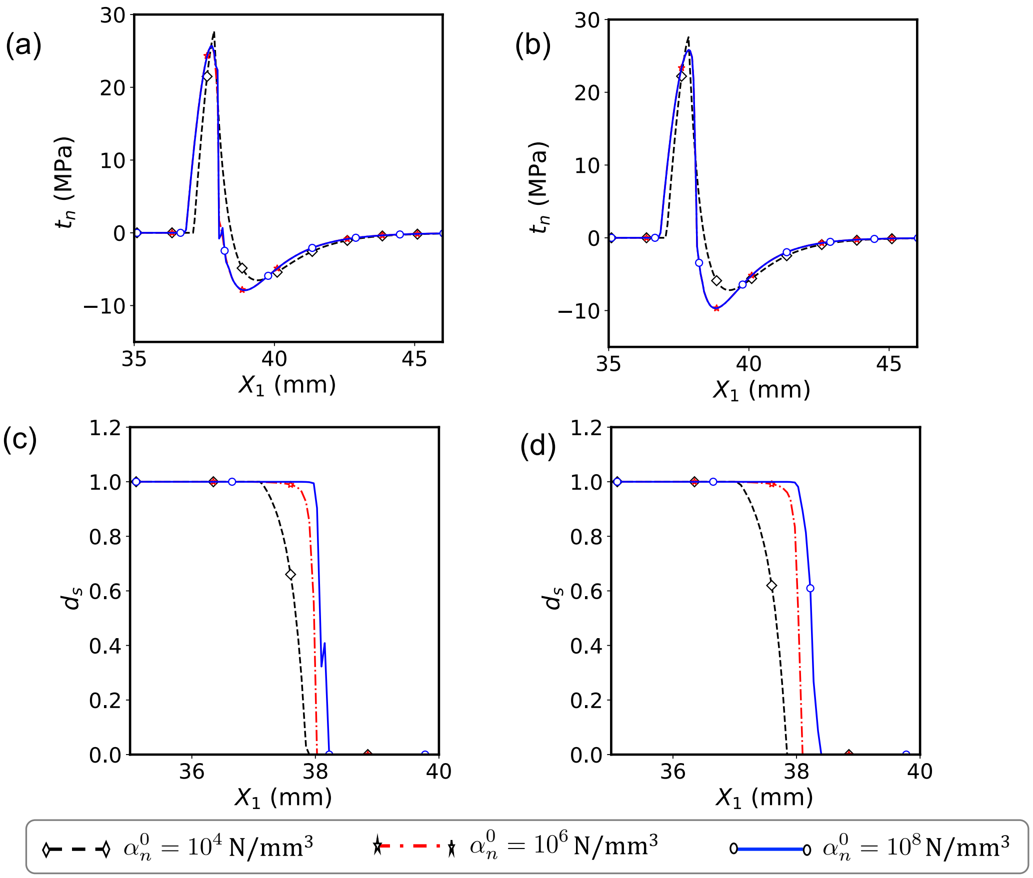

Figure 3.11: Normal traction and damage versus interface length curves from the double cantilever beam test ([0/90] ply orientation) for different cohesive stiffness values: (a), (c) standard FEM and (b), (d) stabilized FEM.

#### 3.4.3.1 Traction at [0/0] Laminate Interface

From Fig. 3.14a, it is evident that the tangential traction profile obtained from the standard FEM is oscillation-free for smaller cohesive stiffness values $\alpha_\tau^0 = 10^4, 10^6$ N/mm$^3$, but for the larger value $\alpha_\tau^0 = 10^8$ N/mm$^3$ a significant oscillation can be seen. Also, the traction field for $\alpha_\tau^0 = 10^4$ from the standard FEM does not match with that for larger stiffness values, which emphasizes the importance of choosing a large enough cohesive stiffness. The traction profile obtained from the stabilized FEM shown in Fig. 3.14b does not exhibit any oscillations for all cohesive stiffness values, thus demonstrating stability and robustness. We also plot the respective damage profiles obtained from both the methods in Figs. 3.14c

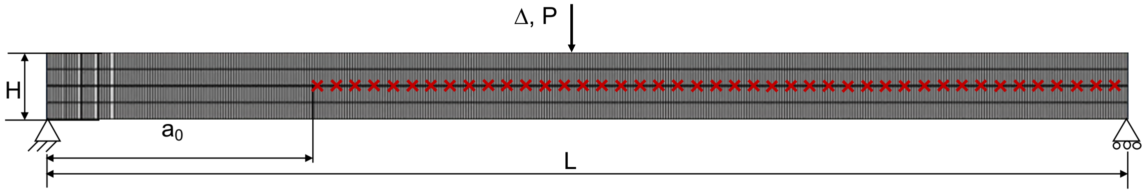

Figure 3.12: Geometry and boundary conditions for the end notch flexure test. The dimensions are: L = 100 mm, H = 3.1 mm and $a_0$ = 35 mm.

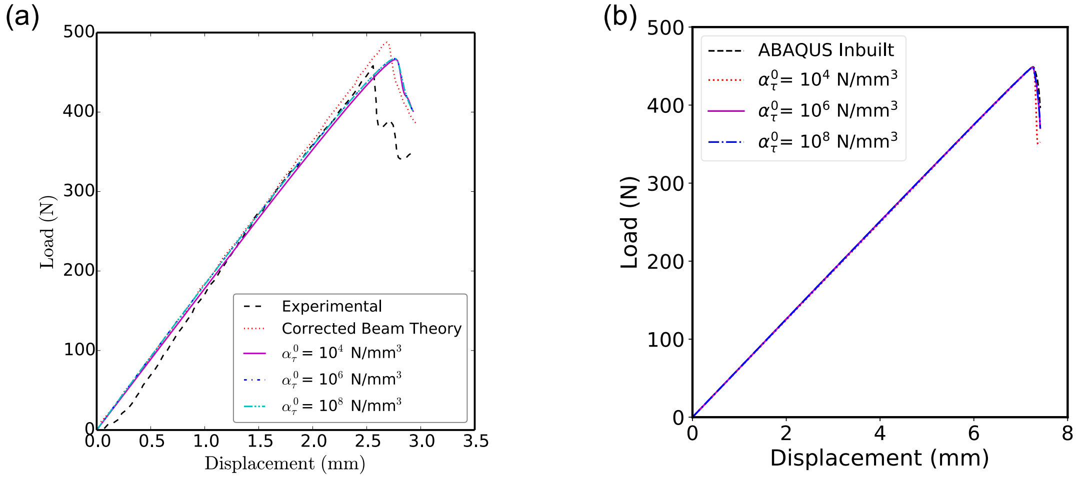

Figure 3.13: Load versus displacement curves for the end notch flexure test obtained using the stabilized FEM: (a) [0/0] laminate and (b) [0/90] laminate.

and 3.14d, which show a corresponding oscillation in the damage profile for the standard FEM for $\alpha_\tau^0 = 10^8$ N/mm$^3$, but no such oscillation exists in the damage profile with the stabilized FEM. These results indicate that even though the standard and stabilized methods capture the load displacement curves well, numerical instability can corrupt the tangential traction and damage field at the interlaminar interface.

We next examined the tangential traction along the delamination interface recovered with a perturbed rectangular mesh, where we change the coordinates of interface nodes by $\approx 3\%$ of the element length. In Fig. 3.15a and 3.15b, we show the tangential traction profiles obtained from the standard FEM and a zoomed-in image showing clear evidence of spurious oscillations. From Fig. 3.15c it is evident that the stabilized FEM is able to alleviate the large amplitude oscillations. This study demonstrates that numerical instability with

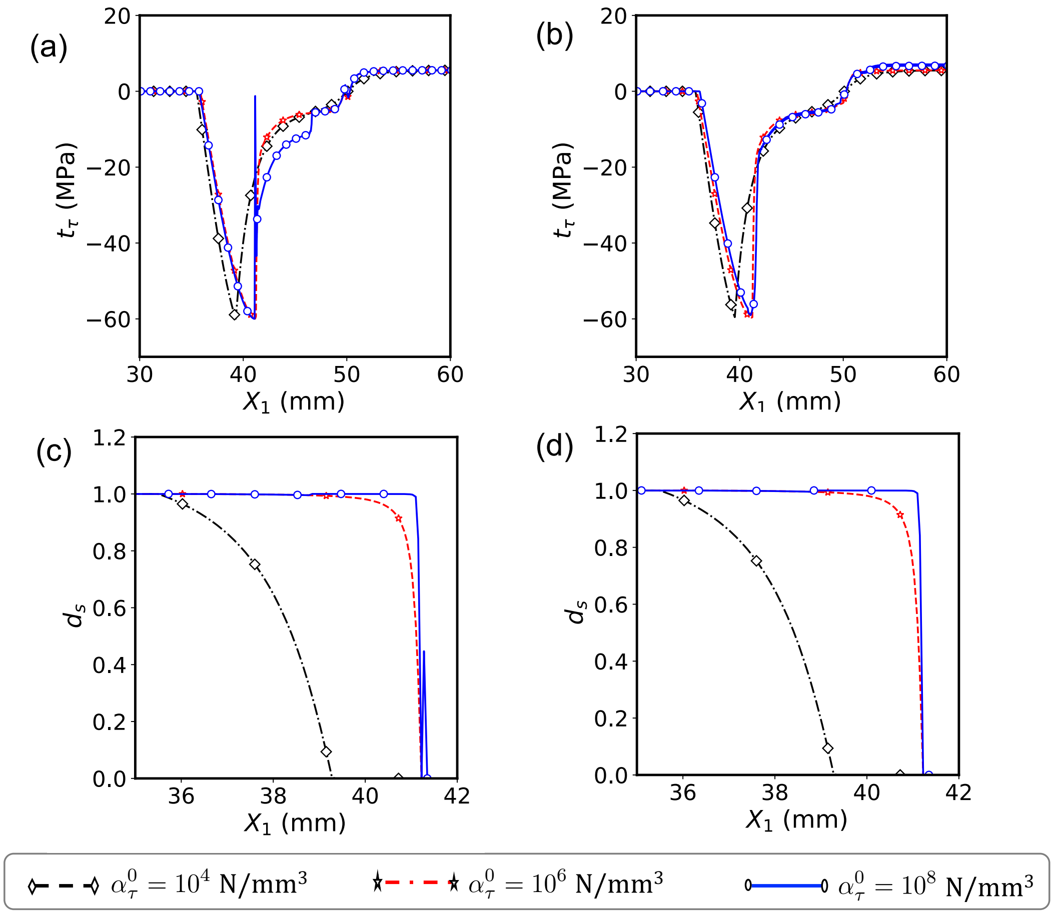

Figure 3.14: Tangential traction and damage versus interface length curves from the end notch flexure test ([0/0] ply orientation) for different cohesive stiffness values: (a), (c) standard FEM and (b), (d) stabilized FEM.

the standard FEM can corrupt tangential traction (i.e. shear stress at the interface) when using perturbed or unstructured finite element meshes, and the amplitude of some spurious oscillations in the mode II ENF test can be large (as much as 50% local error). Therefore, we recommend using the stabilized FEM to improve accuracy and avoid convergence issues with stiff cohesive laws.

#### 3.4.3.2 Traction at [0/90] Laminate Interface

We now examine the interface traction fields obtained from both standard and stabilized methods for the [0/90] laminate interface. Although we expect a similar response to the

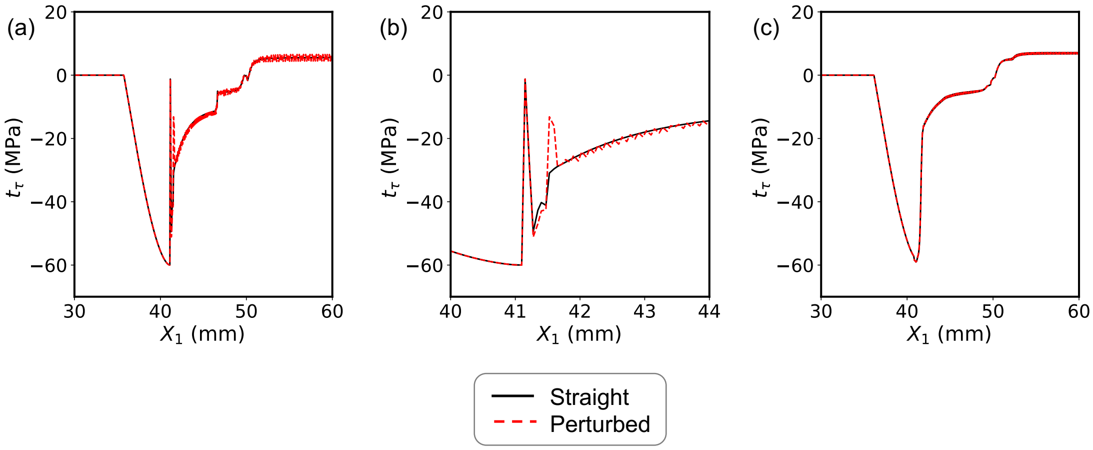

Figure 3.15: Tangential traction versus interface length for $\alpha_\tau^0 = 10^8$ N/mm$^3$ obtained from ENF test ([0/0] ply orientation): (a) standard FEM , (b) zoom in near the crack tip for standard FEM and (c) stabilized FEM.

[0/0] laminate interface case, we present the results here for completeness. In Fig. 3.16, we show the tangential traction along the delamination interface recovered from the standard and stabilized methods for different values of initial cohesive stiffness. We do find large amplitude oscillations in the tangential traction for $\alpha_\tau^0 = 10^8$ N/mm$^3$ in Fig. 3.16a, and in the corresponding damage profile in Fig. 3.16c with standard FEM, whereas no traction oscillations are seen with the stabilized FEM.

### 3.4.4 Fixed Ratio Mixed Mode Test

We also investigated the ability of the stabilized FEM in recovering normal and tangential traction fields during mixed-mode delamination crack growth using the fixed ratio mixed mode (FRMM) test. The specimen geometry and test set-up along with the finite element mesh are shown in Fig. 3.17. To initiate the delamination process, a pre-crack is placed at the left end and vertical displacement is applied only at the upper corner node. The fixed boundary condition is applied at the right end of the beam.

In Fig. 3.18a, we compare the load–displacement curves from the stabilized FEM with the corrected beam theory solution from [3] for [0/0] laminate, due to the lack of experi-

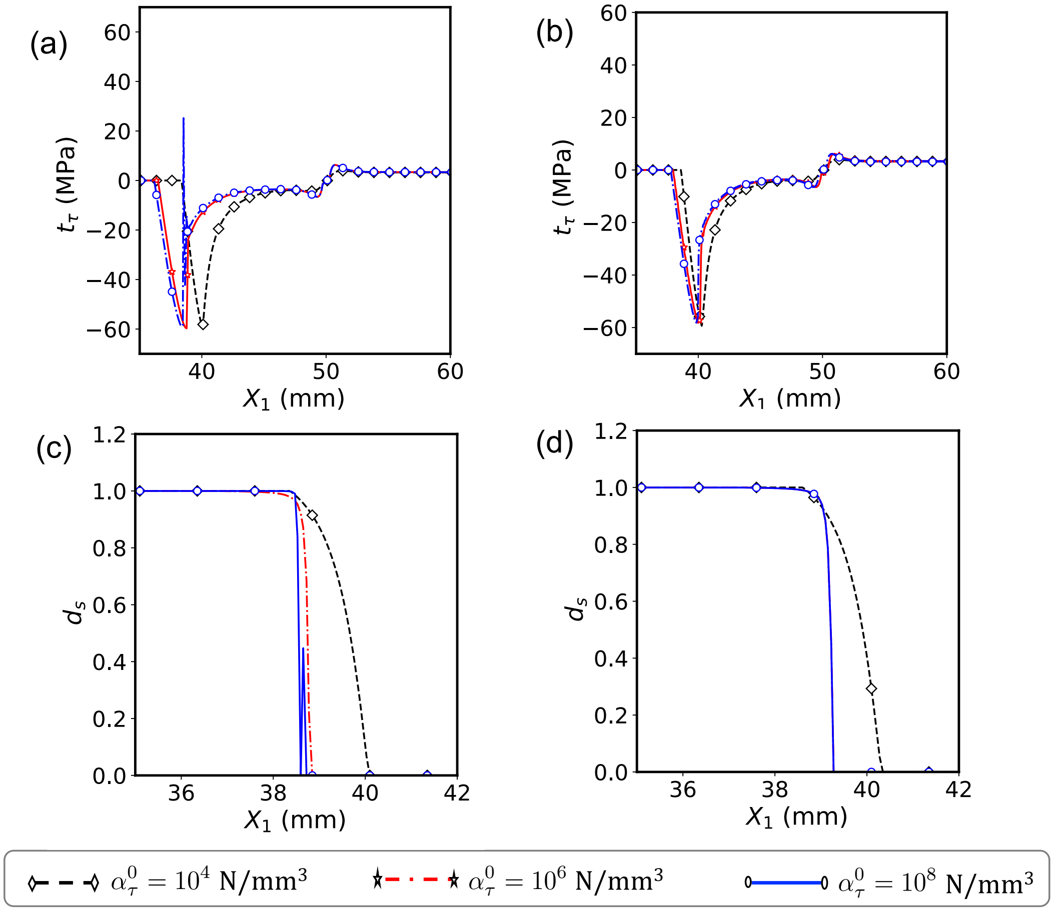

Figure 3.16: Tangential traction and damage versus interface length curves from the end notch flexure test ([0/90] ply orientation) for different cohesive stiffness values: (a), (c) standard FEM and (b), (d) stabilized FEM.

mental data. In Fig. 3.18b, we compare the load–displacement curves from the stabilized FEM with the ABAQUS inbuilt cohesive elements for [0/90] laminate, due to the lack of experimental data or analytical solutions. Because the ABAQUS inbuilt cohesive elements use a different mixed-mode criteria proposed in [96], the predicted peaks loads and softening portions of the load–displacements are different in Fig. 3.18b. However, by choosing different cohesive strengths with different mixed-mode criteria it is possible to match the load–displacement curves obtained from stabilized FEM and inbuilt ABAQUS elements.

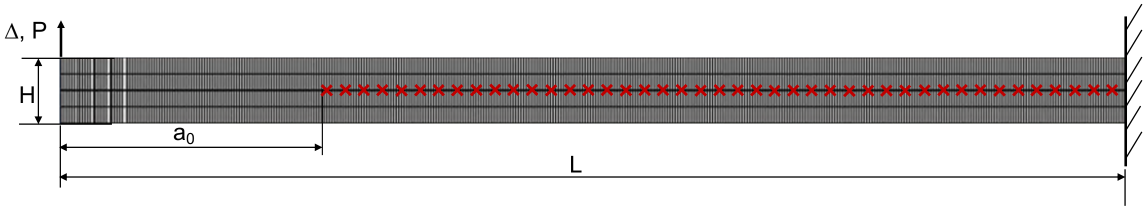

Figure 3.17: Geometry and boundary conditions for the fixed ratio mixed mode test. The dimensions are: L = 50 mm, H = 3.1 mm and a$_0$ = 35 mm.

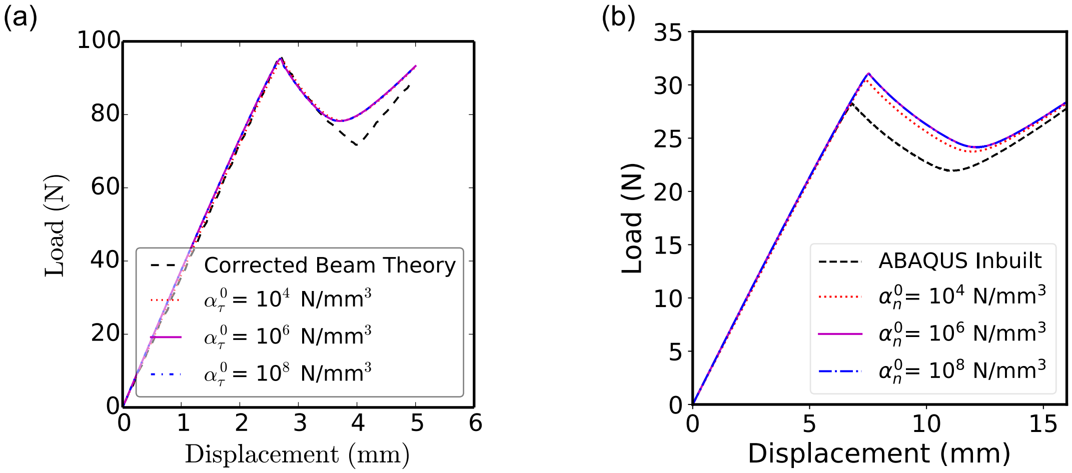

Figure 3.18: Load versus displacement curves for the fixed ratio mixed mode test obtained from the stabilized FEM: (a) [0/0] orientation and (b) [0/90] orientation.

#### 3.4.4.1 Traction at [0/0] Laminate Interface

In Figs. 3.19a and 3.19b, we show the normal and tangential traction profiles for [0/0] laminate from the standard FEM. We find that for the large cohesive stiffness $\alpha_n^0 = \alpha_\tau^0 = 10^8$ N/mm$^3$, large amplitude oscillations appear in the tangential traction, but a few small amplitude oscillation appears in the normal traction profile. The stabilized FEM alleviates oscillations in both normal and tangential traction fields, as evident from Figs. 3.19c and 3.19d. Notably, for the smaller stiffness value of $10^4$ N/mm$^3$, the peak tangential traction value is considerably smaller than the other two cohesive stiffness cases (i.e., $10^6$ N/mm$^3$ and $10^8$ N/mm$^3$) from both methods, which also happens with ABAQUS in-built cohesive elements. This suggests that it is important to take the cohesive stiffness large enough to accurately recover the interface traction for mixed mode loading.

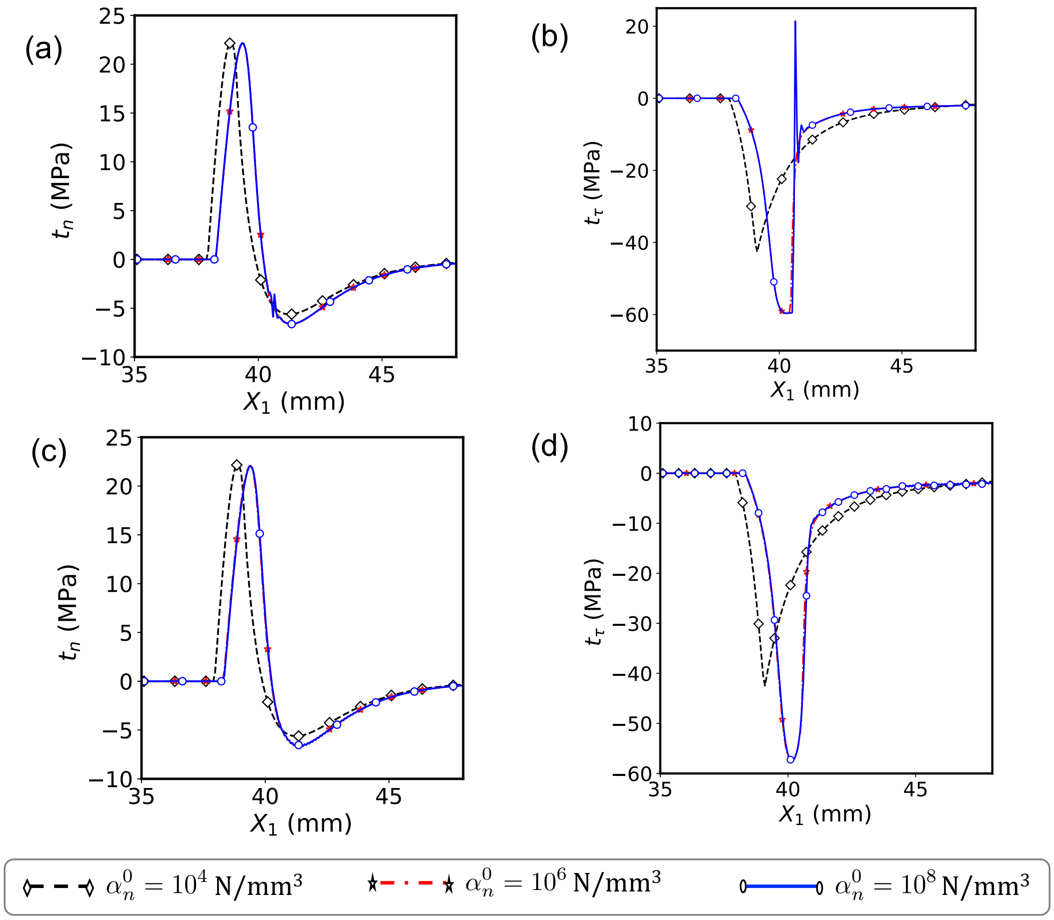

Figure 3.19: (a) Normal and tangential traction fields versus interface length from the fixed ratio mixed mode test ([0/0] ply orientation) for different cohesive stiffness values: (a), (b) standard FEM and (c), (d) stabilized FEM.

### 3.4.4.2 Traction at [0/90] Laminate Interface

In Figs. 3.20a and 3.20b, we show the normal and tangential traction profiles for [0/90] laminate from the standard FEM. We find that for $\alpha_n^0 = \alpha_\tau^0 = 10^8$ N/mm$^3$, large amplitude oscillations appear in both normal and tangential traction profiles. The stabilized FEM alleviates these oscillations, as evident from Figs. 3.20c and 3.20d. We also notice for the smaller stiffness value of $10^4$ N/mm$^3$, the peak tangential traction value is considerably smaller than the other two cohesive stiffness cases (i.e., $10^6$ N/mm$^3$ and $10^8$ N/mm$^3$). Once again, this indicates the importance of taking a larger value for cohesive stiffness to accurately recover the interface traction.

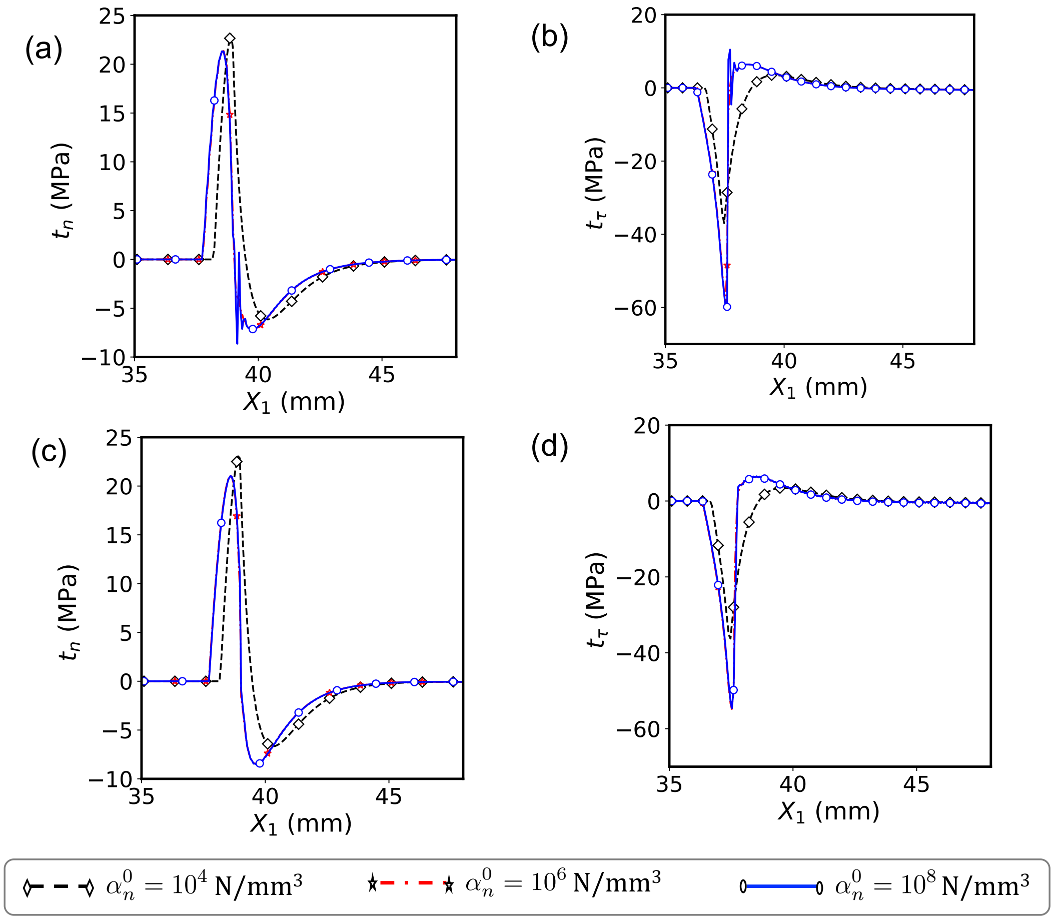

Figure 3.20: Normal and tangential traction fields versus interface length from the fixed ratio mixed mode test ([0/90] ply orientation) for different cohesive stiffness values: (a), (b) standard FEM and (c), (d) stabilized FEM.

## 3.5 Conclusion

In this chapter, we demonstrated the applicability of the stabilized finite element method proposed by Ghosh *et al.* [22] for modeling delamination growth in laminated fiber-reinforced composite materials with transversely isotropic elastic behavior, which are widely used in the aerospace/automobile industry. To achieve Our main objectives are twofold: (1) to highlight the parametric uncertainties, numerical instability, mesh dependence, and computational efficiency issues associated with the commonly used standard finite element method for cohesive fracture/delamination; and (2) to illustrate the advantages of using the stabilized method that address the issues with the standard method in the context of delamination analysis. While the stabilized finite element method for cohesive fracture/delamination problems was fully developed in Ghosh *et al.* [22], it was tested only for isotropic linearly elastic media using simplified patch tests and benchmark problems to verify accuracy and illustrate convergence. In this chapter, we simulated mode-I, mode-II, and mixed-mode crack growth in laminated cross-ply composites by choosing standardized test configurations and validated the results with experimental data, when available. Furthermore, we explored the stability and accuracy of standard and stabilized methods with semi-structured or perturbed meshes for delamination analysis. The key results and findings are listed below:

1. **Constant strain patch tests:** We illustrated that numerical instability with standard FEM causes spurious oscillations in the interface traction fields at both similar and dissimilar composite material interfaces. We found that perturbed, semi-structured and potentially unstructured meshes can aggravate the numerical instability with standard FEM, especially with anisotropic CZMs where the contrast between normal and tangential stiffness is high. We demonstrated the ability of a stabilized method in alleviating spurious traction oscillations at the delamination interface. Thus, these studies illustrated the stabilized method is mesh agnostic, which is advantageous when using non-uniform and semi-structured finite element meshes for delamination analysis.

2. **Benchmark delamination tests:** We examined the traction and damage profiles recovered from the standard and stabilized methods using standardized delamination tests (*i.e.,* DCB, ENF and FRMM tests) to identify numerical instability. We found that the traction oscillations (instability) coincide with an abrupt change in interface damage for an inappropriate choice of cohesive stiffness parameter. Although we observed spurious oscillations in normal and tangential traction fields for a moderately large choice of the cohesive stiffness parameter (*i. e.,* three orders of magnitude larger than the bulk stiffness), these oscillations did not affect the predicted

> load–displacement curves from both standard method. Taking a small cohesive stiffness parameter can alleviate oscillations with the standard method, but it can lead to inaccurate evaluation of the traction field, especially under mixed-mode loading. These studies established the stabilized method as an robust alternative to the standard FEM, so that ad hoc guidelines for stiffness selection are no longer needed.

To conclude, in the standard FEM for delamination modeling the choice of cohesive stiffness is non-trivial and involves a precarious trade-off – prescribing a value that is larger than necessary results in numerical instabilities, whereas prescribing a value that is smaller than necessary results in inaccurate traction recovery. The "appropriate" choice of cohesive stiffness for a given multi-directional multi-ply composite laminate requires trial-and-error procedure and/or conducting sensitivity studies based on 1D model estimates. In contrast, the proposed stabilized FEM is robust and stable for a wide range of cohesive stiffness values. Because the stabilized FEM does not increase the computational cost compared to the standard FEM, it can be advantageous for composite delamination analysis using cohesive/interface elements.

## Chapter 4

# A PORO-DAMAGE MECHANICS-BASED COHESIVE ZONE APPROACH FOR MODELING CREVASSE PROPAGATION IN GLACIERS

This chapter is adapted from “A poro-damage mechanics-based cohesive zone approach for modeling crevasse propagation in glaciers” which will be submitted to *Cold Regions Science and Technology* and has been reproduced with the permission of my co-authors Yuxiang Gao, Xiangming Sun, Stephen Jiménez, and Ravindra Duddu: Gao, Y$^*$., Ghosh, G$^*$., Sun, X., Jiménez, S., and Duddu, R. A poro-damage mechanics based cohesive zone approach for modeling crevasse propagation in glaciers, *In Preparation* ($^*$: Denotes Co-First Author)

## 4.1 Introduction

The plausibility of rapid global sea-level rise predominantly due to mass loss from glaciers and ice sheets due to hydrofracturing of ice shelves and marine ice cliff instability highlights the urgent need for modeling and understanding fracture/failure mechanisms in glaciers. [132, 133, 134, 135, 136] have highlighted the growing need for a better understanding of the glacier fracture/failure mechanisms [137]. In pursuit of this, researchers have fundamentally associated the presence and propagation of crevasses with the key detrimental factors for failure of glaciers like: mass loss, surface ablation, basal sliding, iceberg calving [138]. However, the fracture mechanisms associated with crevasse initiation and propagation, are complex and involve mechanical, thermal and hydraulic fracture processes [23, 24, 25, 26]. For instance, when melt-water infiltrates the surface crevasses or seawater infiltrates the basal crevasses, and the corresponding water pressure on the crevasse walls exceeds the fracture toughness of ice, crevasse propagates deeper into the glacier; this hydraulic-pressure-driven fracture is commonly referred to as hydro-fracture [27]. In this work, we develop a poro-damage mechanics based cohesive zone modeling approach to better understand the complex hydro-fracture process, and the resulting crevasse propagation in glaciers.

There are three broad class of models available in the literature for modeling crevasse formation [138]: the zero stress model, the linear elastic fracture mechanics model, and the continuous damage mechanics model. Here we will briefly review each of these models and talk about their advantages and disadvantages. The zero stress model is based on the notion that crevasses penetrate to the glacier depth at which the ice overburden pressure equals the tensile stress. After being first proposed by [139], the zero stress model has been modified and extensively used by several reserachers [140, 141, 142, 143] for estimating the depth of water-filled crevasses. This model suffers from issues like over-simplistic assumptions or not accounting for the finite glacier thickness, thus limiting it's applications. To address the issues with the zero stress models, fracture mechanics based models were developed based on the notion that glacier ice contains innumerable preexisting minute cracks, in which both sides of the fracture are touching, that permit the propagation of crevasses [144]. Under the linear elastic material assumption, the fracture mechanics model infers that a crevasse propagates downward as long as the intensity factor at the crevasse tip is larger than the fracture toughness of the surrounding ice [145, 144]. The LEFM model does a better job of capturing the physics of crevasse formation compared to the zero stress model and has been used by several researchers [146, 147, 148, 149, 150] to understand critical tensile stress, crevasse water depths, role of multiple crevasses, etc. The fracture mechanics approach suffers from the following limitations: (i) it relies on critical parameters, such as crevasse spacing and ice fracture toughness, which must be prescribed a priori and are not readily available in most numerical flow models; (ii) the widely adopted coefficients of the fracture mechanics model are not suitable for application to crevasse fields in which crevasse spacing influences depth and (iii) assuming a linear elastic rheology in place of the true nonlinear rheology of glacier ice is a fundamental approximation of the contemporary fracture mechanics approach [138]. In last two decades, the continuum damage mechanics-based approach has been developed and used for predicting crevasse depth

[151, 152, 153, 154, 155]. The continuum damage mechanics model has following advantages: (i) easy to implement and does not need complex algorithms to track the crevasse propagation; (ii) it does not need a pre-crack unlike the LEFM model to initiate crevasse propagation. It suffers from the issues like: (i) this model involves several empirical parameters that may not be uniquely calibrated from existing experiments or observations, and this parametric uncertainty can affect its predictive capability and (ii) this model within a full Stokes numerical formulation is computationally expensive for investigating crevasse propagation in real glaciers or ice shelves.

In last few decades, non-linear models have gained particular interest in modeling glacier and ice sheet evolution. The presence of large distributed zone of cracking, known as the fracture process zone in the context of quasi-brittle fracture mechanics, leads to nonlinearity into the fracture scaling, necessitating either a quasi-brittle (nonlinear) representation of the fracture or the use of a non-local damage model [156, 157]. Among the available models, the non-linear Stokes equations provide an accurate and complete description of momentum balance for modeling the flow of land ice [158, 159] compared to other approaches. More recently, researchers have used higher-order finite element discretization, scalable solvers and updated-Lagrangian formulation for the solution of Stokes equations [160, 161, 162, 155]. The other popular approaches developed in last two decades include: a non-linear visco-elastic/visco-plastic approach to model uniaxial deformation of sea-ice [163, 164]; discrete particle-based simulation model where ice body is made of discrete particles linked to each other by bonds that can break off when undergoing a too high stress [165, 166]; discrete element methods have been conducted to simulate the brittle failure of ice [167, 168, 169, 170]; a probabilistic approach-based study where a logistic regression algorithm has been developed to predict the fracture locations in an ice shelf [171].

Recently, a poro-damage based approach has been proposed by [172] which incorporates the effects of water pressure in crevasses, based on the principles of continuum damage mechanics and poro-mechanics. This new approach considers the effect of water pressure inside damaged ice in the crevasse as an additional damage effect. Extending the concept of this model and the continuum damage approach proposed by [155], a non-local continuum poro-damage mechanics (CPDM) model has been proposed by [173] to simulate hydro-fracture in glaciers. The CPDM model alleviates spurious mesh-size sensitivity and artificial diffusion of damage in crevasse propagation simulations and accounts for the feedback between viscous (or elastic) and damage processes at the crevasse tip. On the other-hand, cohesive zone modeling approach is another popular numerical tool for simulating hydraulic fracture in the poro-elastic medium [174, 175, 176, 177]. In this approach, a zero-thickness interface element is placed along the potential crack path and it's behavior is governed by a cohesive law. Although this approach has been extensively used in modeling hydro-fracture in rocks [178, 179, 177], to authors' knowledge no such study exists for ice.

In this work, we present a cohesive zone modeling approach for simulating hydro-fracture and crevasse propagation in glaciers by using the poro-damage mechanics formulation proposed by [172]. In our formulation, we interpret damage to represent the ratio of isotropic void area to total area along the cohesive interface, we assume that water can permeate the damaged material and exert hydrostatic pressure along the interface. The rest of the article is organized as follows: in Section 4.2, we present the strong form of the governing equations of the poro-damage based CZM model for hydro- fracture; in Section 4.3, we present a concise discussion of the key points in implementation and choice of model parameters; in Section 4.4, we present a concise discussion of the key points in implementation and choice of model parameters, and several idealized simulation results for ice fracture and calving for real glaciers; and in Section 4.5, we conclude with a summary and closing remarks.

## 4.2 Model Formulation

In this section, we present a detailed description of the poro-damage mechanics based extension of an existing mixed mode cohesive zone model for modeling quasi-static hydrofracturing. We then present the linear elastic, linear/nonlinear viscoelastic constitutive models for glacier ice, and the strong form of the governing equations of static equilibrium.

### 4.2.1 Cohesive Zone Modeling Approach

The cohesive zone modeling approach represents a nonlinear fracture/damage process based on the concept of bounded stress within the cohesive zone at the crack tip , unlike linear elastic fracture mechanics (LEFM) where the stress is singular at the crack tip. The major advantage of this approach is its ability to describe crack initiation and propagation within the framework of the finite element method. Generally, the cohesive zone model (CZM) is implemented by inserting a zero-thickness interface/cohesive elements along potential crack interfaces between bulk finite elements in the undeformed mesh configuration. (Fig. 4.1). Under the action of tensile and shear stresses in the bulk finite elements, the cohesive element stretches and thus simulating crack opening and sliding in the deformed mesh configuration (e.g. see Fig. 4.5b). This crack interface separation is defined by the nodal displacements of the cohesive element as

$$\boldsymbol{\Delta} = [\![\mathbf{u}]\!] = \mathbf{u}^{(2)} - \mathbf{u}^{(1)}, \tag{4.1}$$

The interface traction vector $\mathbf{t}_\mathrm{c}$ can be defined as

$$\mathbf{t}_\mathrm{c} = \boldsymbol{\alpha}(\boldsymbol{\Delta})\ \boldsymbol{\Delta}, \tag{4.2}$$

where the cohesive stiffness matrix $\boldsymbol{\alpha}$ is usually a nonlinear function of the interface separation. The above equation is the so-called cohesive law or traction-separation law describing the constitutive behavior of the cohesive elements.

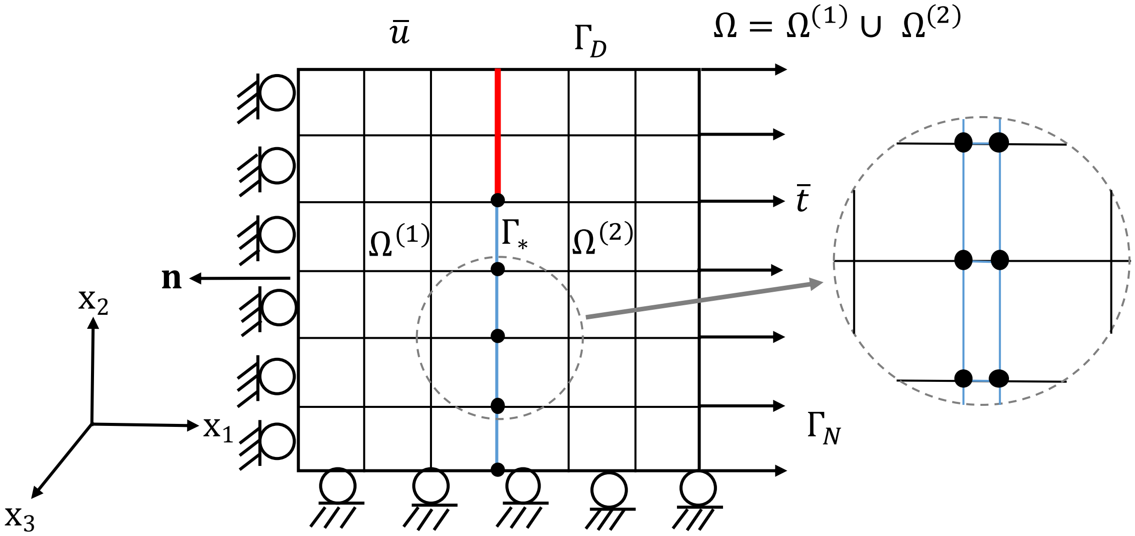

Figure 4.1: A typical mesh for the glacier with cohesive interface elements placed at the interface. The crack is represented by a red line, where the cohesive elements have failed.

### 4.2.2 Bilinear Cohesive Law

The cohesive law generally features an initial elastic response to resist crack opening followed by an irreversible damage-induced softening response. In this study, we have assumed a bilinear cohesive law consisting an initial (increasing) linear elastic region followed by a (decreasing) linear softening region. For mixed-mode delamination under quasi-static loading in two-dimensions, we cast the bilinear cohesive law in the damage mechanics framework as detailed in [79]. The tangential $t_\tau$ and normal $t_n$ components of the interface traction vector $\mathbf{t}_c$ are related to the tangential $\Delta_\tau$ and normal $\Delta_n$ components of the interface separation $\boldsymbol{\Delta}$ as

$$\mathbf{t}_c = \begin{Bmatrix} t_\tau \\ t_n \end{Bmatrix} = \begin{bmatrix} (1-D_s)\alpha_\tau^0 & 0 \\ 0 & \left(1 - D_s \dfrac{\langle \Delta_n \rangle}{\Delta_n}\right) \alpha_n^0 \end{bmatrix} \begin{Bmatrix} \Delta_\tau \\ \Delta_n \end{Bmatrix}, \tag{4.3}$$

where $\alpha_n^0$ and $\alpha_\tau^0$ represent the initial cohesive stiffness in the normal and the tangential directions, respectively, and the scalar damage variable $D_s$ is given by

$$D_s = \begin{cases} 0 & \text{if} \quad \Delta_e < \Delta_e^c, \\ \dfrac{\Delta_e^u(\Delta_e - \Delta_e^c)}{\Delta_e(\Delta_e^u - \Delta_e^c)} & \text{if} \quad \Delta_e^c \leq \Delta_e < \Delta_e^u, \\ 1 & \text{if} \quad \Delta_e^u \leq \Delta_e, \end{cases} \tag{4.4}$$

and the equivalent separation $\Delta_e = \sqrt{\langle \Delta_n \rangle^2 + \Delta_\tau^2}$. In the above equations, $\langle \cdot \rangle$ denotes Macaulay brackets, so that $\langle \Delta_n \rangle = \max(0, \Delta_n)$, which ensures that there is no damage growth or damage effect on the normal cohesive stiffness response under compression or contact. The critical and ultimate interface separation parameters $\Delta_e^c$ and $\Delta_e^u$ can then be defined as [5]:

$$\frac{1}{\Delta_e^c} = \sqrt{\left(\frac{\alpha_n^0 \cos I}{\sigma_{\max}}\right)^2 + \left(\frac{\alpha_\tau^0 \cos II}{\tau_{\max}}\right)^2}, \tag{4.5}$$

$$\frac{1}{\Delta_e^u} = \left(\frac{\alpha_n^0 \Delta_e^c (\cos I)^2}{2\, G_{IC}}\right) + \left(\frac{\alpha_\tau^0 \Delta_e^c (\cos II)^2}{2\, G_{IIC}}\right), \tag{4.6}$$

where the direction cosines $\cos I = \Delta_n / \Delta_e$ and $\cos II = \Delta_\tau / \Delta_e$, $\sigma_{\max}$ and $\tau_{\max}$ are the pure mode I and mode II cohesive strengths, and $G_{IC}$ and $G_{IIC}$ are the pure mode I and mode II critical fracture energies. A schematic diagram of the bilinear traction-separation relationship and the damage-separation relationship are shown in Fig. 2.3.

### 4.2.3 Extension of Cohesive Law Based on Poro-damage Mechanics

Herein, we present an augmented traction-separation law that incorporates hydraulic fracture. As we interpret damage to represent the ratio of isotropic void area to total area along the cohesive interface, we assume that water can permeate the damaged material and exert hydrostatic pressure along the interface. Our implementation is based on the poro-mechanics approach proposed in [172, 180, 173] for hydraulic fracture within ice

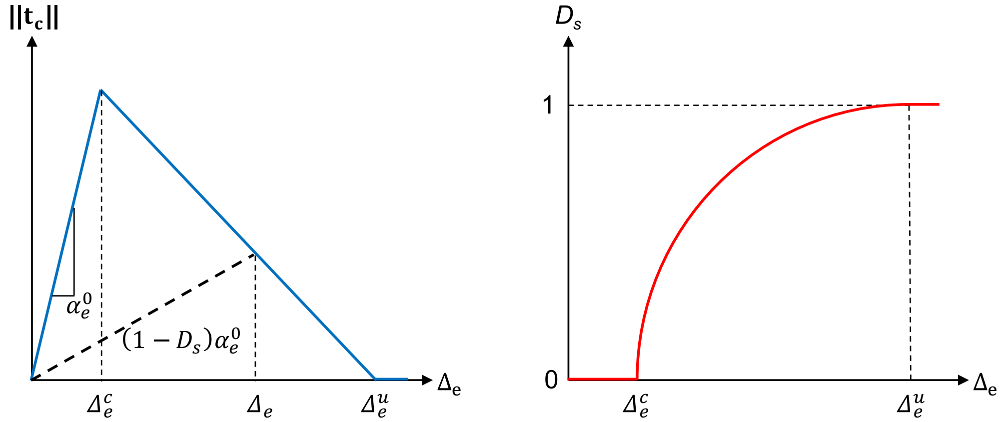

Figure 4.2: A schematic diagram of the bilinear cohesive zone model: (a) the traction-separation relationship; (b) the relationship between the static damage variable $D_s$ and the equivalent separation. The magnitude of the traction vector $\|\mathbf{t}_c\| = \sqrt{t_n^2 + t_\tau^2}$.

sheets based on continuum damage mechanics, which extends Biot's theory of poroelasticity [181] by considering damage to have the same effect on the material behavior as porosity. Poroelasticity theory states that the Cauchy stress tensor $\sigma_{ij}$ in a porous media can be written as,

$$\sigma_{ij} = (1-\phi)\tilde{\sigma_{ij}} - \phi p_w \delta_{ij}, \tag{4.7}$$

where $\tilde{\sigma_{ij}}$ is the effective Cauchy stress tensor, $\phi$ is the material porosity, and $p_w$ is the hydraulic pressure within the crack. The above equation can be simply recast as a damage mechanics formulation by replacing the porosity $\phi$ with the damage variable $\mathrm{D}_s$ (we assume that damage and porosity are equivalent in isotropically damaged ice):

$$\sigma_{ij} = (1-D_s)\tilde{\sigma_{ij}} - D_s p_w \delta_{ij}. \tag{4.8}$$

The poro-mechanics approach to simulate hydraulic fracture can be similarly applied to the CZM by introducing a new term to the traction-separation law in Eq. 3.8, which is able to account for hydraulic pressure in the damaged zone. The augmented traction-separation law can then be extended as,

$$\mathbf{t}_\mathrm{c} = \begin{Bmatrix} t_\tau \\ t_n \end{Bmatrix} = \begin{bmatrix} (1-D_s)\alpha_\tau^0 & 0 \\ 0 & \left(1-D_s\dfrac{\langle\Delta_n\rangle}{\Delta_n}\right)\alpha_n^0 \end{bmatrix} \begin{Bmatrix} \Delta_\tau \\ \Delta_n \end{Bmatrix} - D_s p_w \begin{Bmatrix} 0 \\ 1 \end{Bmatrix}. \tag{4.9}$$

As shown in Fig. 4.5(a), we consider a rectangular ice slab with water-filled surface. We use the Cartesian coordinate system with $(x_1,x_2,x_3) = (x,y,z)$, where $x$ and $z$ represent in-plane horizontal and vertical coordinates, respectively; and the direction of $y$-axis must point into the $x$-$z$ plane to obey the right-handed rule. The hydraulic pressure can then be defined as,

$$p_\mathrm{w}(z) = \rho_\mathrm{f} g \langle h_\mathrm{s} - (z - z_\mathrm{s})\rangle \tag{4.10}$$

where $\rho_f$, $g$, $h_s$, and $z_s$ denote the density of freshwater, acceleration due to gravity, water height in the surface crevasse, and vertical coordinate of the surface crevasse tip, respectively. Because hydrostatic pressure only acts in the direction normal to the cohesive interface, we apply $p_w$ in Eq. 4.9 to the normal traction component ($\mathrm{t}_n$) only.

A schematic illustration of the poro-damaged based cohesive zone modeling approach is shown in Fig. 4.3. In the figure, two adjacent bulk elements are initially in a perfectly bonded condition, and a zero-thickness cohesive element is present in between them. As the tensile stress at the crack tip exceeds the maximum cohesive strength and a critical separation is reached, damage starts to propagate under hydrostatic pressure. Therefore, $D_s = 0$ accounts for perfectly bonded condition, and $D_s = 1$ accounts for completely opened crack after failure. For the case of $0 < D_s < 1$, the crack is filled with air and/or water and starts to contribute in the normal traction component as given by Eq. 4.9.

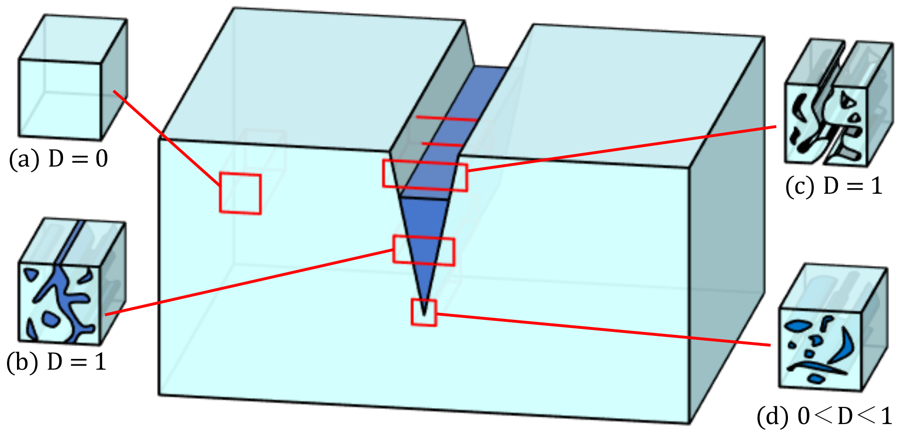

Figure 4.3: Schematic illustration of poro-damage mechanics based cohesive zone model.

### 4.2.4 Constitutive Model for Bulk Ice

The mechanical response of ice over shorter time scales (seconds to hours) is often described by linear elastic or visco-elastic constitutive models [182], whereas glacier and ice-sheet flow over longer times scales (days to centuries) is best described by a non-linear viscous constitutive model known as Glen's law [183].

Assuming small strains, the additive decomposition of the total strain tensor into its components is assumed as,

$$\boldsymbol{\epsilon} = \boldsymbol{\epsilon}^e + \boldsymbol{\epsilon}^v, \tag{4.11}$$

where $\boldsymbol{\epsilon}^e$, and $\boldsymbol{\epsilon}^v$ denote the elastic strain tensor (time independent and recoverable component), and the viscous strain tensor (time-dependent and irrecoverable component), respectively [184, 185]. The elastic stress–strain relation is given by the generalized Hooke's law,

$$\sigma_{ij} = C_{ijkl}\varepsilon^e_{kl}, \tag{4.12}$$

where $\sigma_{ij}$ denotes the components of Cauchy stress tensor, $\varepsilon^e_{kl}$ denotes the components of elastic small strain, and $C_{ijkl}$ denotes the components of fourth-order isotropic elasticity tensor. The elastic strain tensor is given by the following expression:

$$\varepsilon_{kl}^{e} = \frac{1}{E}[\sigma_{kl} - \nu(\sigma_{ii}\delta_{kl} - \sigma_{kl})], \tag{4.13}$$

where E is the elasticity modulus, $\nu$ is the Poisson's ratio, $\delta_{kl}$ is the Kronecker's delta and repeated indices mean summation. The fourth order elasticity tensor $C_{ijkl}$ can be expressed as:

$$C_{ijkl} = \frac{E}{2(1+\nu)}(\delta_{il}\delta_{jk} + \delta_{ik}\delta_{jl}) + \frac{E\nu}{(1+\nu)(1-2\nu)}\delta_{ij}\delta_{kl}, \tag{4.14}$$

The permanent viscous strain rate, $\dot{\varepsilon}_{kl}^{v}$, is generalized by the power-law creep equation [185] as,

$$\dot{\varepsilon}_{kl}^{v} = \frac{3}{2}K_N(\frac{3}{2}\sigma_{mn}^{dev}\sigma_{mn}^{dev})^{(N-1)/2}\sigma_{kl}^{dev}, \tag{4.15}$$

where K$_N$ and N are viscous parameters. The power exponent, N, is determined to be around 3 in most experimental and field investigations.

### 4.2.5 Strong Form of the Cohesive Fracture Problem

To model the cohesive fracture problem in glaciers, we consider an ice domain $\Omega$ (as shown in Fig. 4.4), which is composed of two undamaged non-overlapping bulk domains $\Omega^{(1)}$ and $\Omega^{(2)}$ separated by a pre-defined internal cohesive interface $\Gamma_*$ along the potential crevasse path. Dirichlet and Neumann boundary conditions are enforced on two disjointed parts of the domain boundary $\Gamma \equiv \partial\Omega$. The outward unit normal to the boundary $\partial\Omega$ is denoted by **n**.

Assuming small deformations, the governing static equilibrium in presence of body force can be described by the standard boundary value problem:

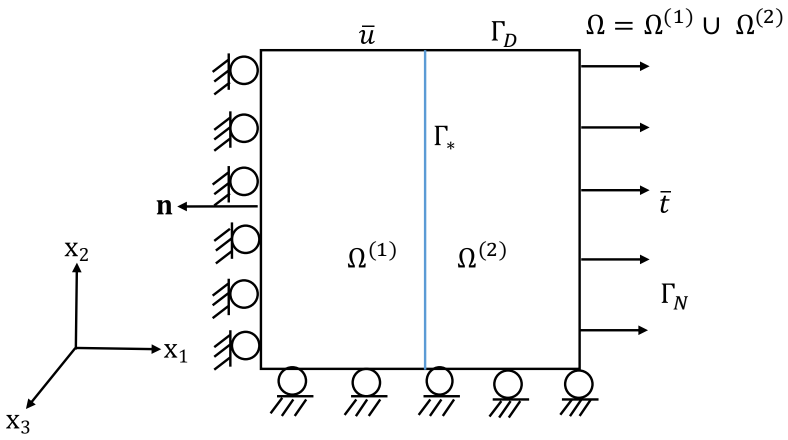

Figure 4.4: A schematic of the domain for the quasi-static cohesive fracture problem.

$$\sigma_{ij,j} + b_i = 0 \text{ in } \Omega^{(m)}, \quad m = \{1,2\}, \tag{4.16}$$

$$u_i = \bar{u}_i \text{ on } \Gamma_D, \tag{4.17}$$

$$\sigma_{ij} n_j = \bar{t}_i \text{ on } \Gamma_N, \tag{4.18}$$

where $b_i$ is the body force vector, $\bar{u}_i$ is the prescribed displacement vector on the Dirichlet boundary $\Gamma_D$ corresponding to free slip or zero slip, and $\bar{t}_i$ is the prescribed traction on the Neumann boundary $\Gamma_N$ corresponding to seawater pressure on the domain boundary.

## 4.3 Numerical Implementation

In this section, we implement the extended cohesive zone model based on poro-damage mechanics in the commercial software ABAQUS through user-defined subroutines. We first briefly present key details of ABAQUS implementation and then list the model parameters that are specific to modeling of glacier crevasses propagation. Next, we briefly describe the effect of compressibility on glacier ice followed by a discussion on the model geometry and boundary conditions for the two scenarios considered in our study, namely grounded glacier and floating ice shelf.

### 4.3.1 ABAQUS Implementation

We implement the extended cohesive zone formulation in the commercial software ABAQUS and utilize the User Element (UEL) subroutine for modeling four-noded linear zero-thickness cohesive elements with two-point Gauss integration scheme; whereas, the bulk (i.e., non-interface) elements are modeled using bilinear quadrilateral four-noded plane strain continuum elements with four-point Gauss integration scheme. We choose interface element sizes in such a way so that there are at least three interface elements within the estimated cohesive process zone; this is necessary for an accurate representation of the numerical stress distribution within the process zone at the point of initial crack propagation, as elaborated in [3]. User-element subroutines in ABAQUS typically require the user to provide the stiffness matrix (AMATRX) and the right hand side (RHS) force vector. In our implementation, we utilize the UEL subroutine to provide the cohesive element force vector and stiffness matrix.

### 4.3.2 Ice properties and model parameters

The material properties for incompressible, linear elastic ice are taken as follows: the elastic modulus E = 9500 MPa, the Poisson's ratio $\nu$ = 0.4995, and the density as $\rho_i$= 917 kg/ $m^3$. The CZM parameters chosen in our simulation studies are listed in Table 4.1. The mode I and mode II fracture energies for the ice are taken from [186, 147]. For ensuring the accuracy and convergence of crack analysis using the FEM with cohesive elements, two conditions must be satisfied: (1) the element size must be less than the cohesive (process) zone length, which is determined by fracture toughness and cohesive strength; and (2) the cohesive stiffness must be large enough to avoid the introduction of artificial compliance. An approximate value of the cohesive strength ($\sigma_c$) can be obtained by using the following formula [187]

$$l_c \approx \frac{EG_{IC}}{\sigma_c^2} = \frac{K_{IC}^2(1-\nu^2)}{\sigma_c^2}, \tag{4.19}$$

where $l_c$ is the length scale parameter and an indicator of the length of the fracture process zone (FPZ) ahead of the crack tip, $G_{IC}$ is the Griffith fracture energy, and $K_{IC}$ is the fracture toughness of the glacier ice. Based on the previous studies [147, 151] we have considered cohesive strength in the range of 35-350 kPa and chose the length scale accordingly.

Table 4.1: Cohesive zone model parameters for ice.

| $\alpha_n^0$ (N/m$^3$) | $\alpha_\tau^0$ (N/m$^3$) | $G_{IC}$ (Pa.m) | $G_{IIC}$ (Pa.m) | $\sigma_{\max}$ (kPa) | $\tau_{\max}$ (kPa) |
|---|---|---|---|---|---|
| $10^{10}$ | $10^{10}$ | 12.63 | 12.63 | {35-350} | {35-350} |

### 4.3.3 Compressibility of Glacier Ice

It is important to mention here that there is an ambiguity in the glaciological community regarding the Poisson's ratio for ice. This discussion has it's roots in the fundamental question: whether ice is an incompressible material or a compressible material. It has been found that in laboratory conditions, ice shows a compressible behavior and researchers have suggested that we should take 0.35 as Poisson's ratio [188]; on the contrary the researchers conducting field experiments on glaciers found that ice behaves as an incompressible material and we should take 0.5 as Poisson's ratio [183]. The compressible behavior can be explained from the context of the fact that without initial overburden pressure, the ice shelf experiences an initial volumetric contraction $\sim p_0/K$ with bulk modulus K; whereas this volumetric contraction does not occur in real ice shelves because ice can be well approximated as being incompressible at timescales longer than the Maxwell time [189]. To address this issue, [190] accounted for an initial hydrostatic stress in a manner following [191] wherein the equations of elasticity are solved for a perturbation stress tensor $\sigma_{ij}^{'}$ defined as the total (Cauchy) stress tensor plus the initial overburden pressure,

$$\sigma_{ij}^{'} = \sigma_{ij} + p_0\delta_{ij} \tag{4.20}$$

where the overburden pressure is as follows:

$$p_0 = \rho_i g(H - z) \tag{4.21}$$

The inclusion of perturbation stress tensor is necessary to explain the physical behavior of ice as described earlier. In this study, for both the grounded glacier and floating ice shelves, we have addressed this issue and provided an observation-based guideline on whether one should consider ice as compressible/incompressible material in  A.

### 4.3.4 Model Geometry and Boundary Conditions

We perform a series of numerical studies using the augmented cohesive zone model (CZM) to predict the evolution of water-filled surface crevasses in grounded glaciers and floating ice-shelves. For the grounded glacier example, we consider an idealized rectangular glacier of length L = 500 m and height H = 125 m. For simplicity, we neglect lateral shear and restrict the domain to a flow line near the terminus of a grounded glacier. The glacier is grounded on a rigid, frictionless (free-slip) bed and terminates at either ground or ocean depending on the seawater depth $h_w$, as depicted in Fig. 4.5 . To discount the free translation motion of the glacier, we apply a boundary condition to enforce zero horizontal displacement at the left edge of the domain. The hydrostatic pressure from seawater is applied as a traction (Neumann) boundary condition normal to the right edge of the ice slab with magnitude $-\rho_{s}g\langle h_w - z\rangle$. This loading configuration has glaciological significance as it represents a land or marine-terminating glacier resting over a free-slip surface and deforming under its self-weight.

For the floating ice shelf example, we consider an idealized, rectangular domain with length L = 5000 m and height H = 125 m under plane strain assumptions, as depicted in

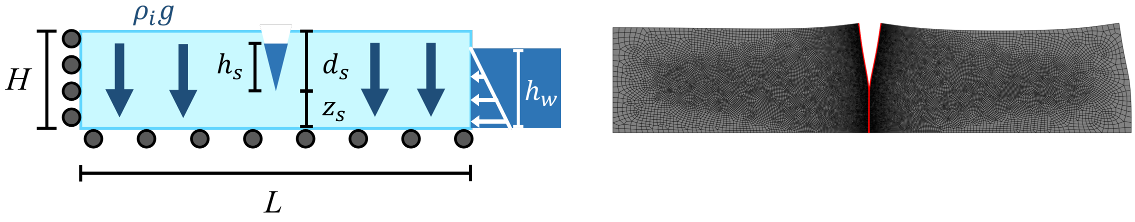

Figure 4.5: (a) Loading configuration for the grounded glacier with height H =125 m and length L =500 m and a no-slip boundary condition at the base. (b) Finite element mesh used for discretizing the domain.

Fig. 4.6 for all the finite element simulations. A free-slip (roller) boundary condition is applied to the left edge to prevent horizontal motion. A Robin-type boundary condition is applied to the bottom domain edge in order to simulate buoyancy of the floating ice shelf in seawater. Hydrostatic pressure is applied as a Neumann boundary condition to the right domain edge with seawater level $h_w/H=\rho_i/\rho_s$, which is the floating depth of ice.

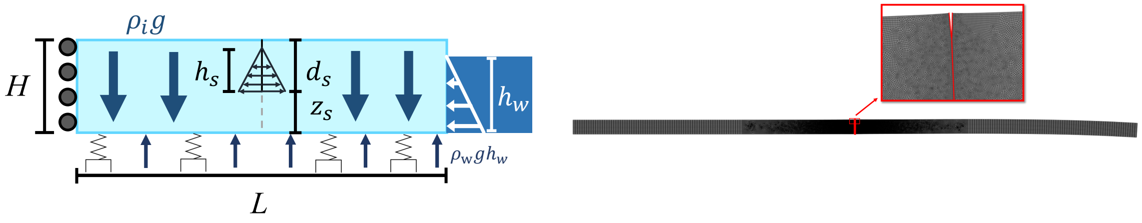

Figure 4.6: (a) Loading configuration for the floating ice shelf with height H =125 m and length L =5000 m. (b) Finite element mesh used for discretizing the domain.

## 4.4 Numerical Examples

In this section, we present several examples to demonstrate the ability of the poro-damage mechanics based augmented cohesive zone formulation in predicting crevasse depth for grounded glaciers and floating ice shelves with surface crevasses. We also address how the rheology, elastic modulus, and density parameters can affect the predicted crevasse depth and what are their implications in real glaciers.

### 4.4.1 Effect of Visco-elastic Rheology on Crevasse Depth Prediction

Researchers have shown that the material response of ice can be highly non-linear and visco-elastic [192] and the rheology plays an important role in understanding the glacier dynamics and making reliable predictions. Also, the tensile strength of ice is an important parameter in determining crevasse depth or predicting calving events, but there is a great uncertainty in estimating the correct value of it. A huge range of strength values have been proposed by the researchers e.g.,0.7-3.1 MPa for laboratory and lake ice [193], 0.09-0.32 MPa for glacier ice [194], 0.03-0.08 MPa for single crevasses to be formed [148]. Thus, in this section, we investigate and try to gain a better insight into the role of ice rheology in predicting the crevasse depth for a grounded glacier and a floating ice shelf, respectively while varying the cohesive strength in the range of 35-220 kPa. In order to achieve this goal, we first modeled ice as a linear elastic material in case of a near flotation grounded glacier and an ice shelf, and compared the predicted crevasse depth with the analytical LEFM solution for different cohesive strength values as shown in Fig. 4.7 (a) and (c), respectively. The key observations are as follows:

1. If we choose a lower cohesive strength of 35 kPa, the predicted crevasse depth shows an excellent match with the LEFM solution in both the grounded glacier and the floating ice shelf. Here, for small deformation, both the grounded glacier and floating ice shelf matches well with the linear elastic solution.

2. For a higher cohesive strength of 220 kPa, the crevasse fails to propagate in both grounded glacier and floating ice shelf. Whereas, for a cohesive strength of 110 kPa, although the grounded glacier still don't have any crevasse propagation, crevasse suddenly starts to propagate in the floating ice shelf once the melt-water reaches around 90%. This behavior can be explained from the fact that the stress state in a near flotation grounded glacier is such that it is less likely to propagate a crevasse than that in case of an ice shelf. In other words, a smaller threshold is enough to

arrest the crack propagation in the near flotation grounded glacier.

3. The difference between the LEFM and cohesive zone model solution can be explained form the fact that in LEFM, there is no concept of finite cohesive strength at the crack tip and essentially a stress singularity occurs there due to the presence of infinite stress. Whereas, in reality the material has a plastic zone at the crack tip and there is no such infinite stress present, cohesive zone model with a finite cohesive strength is more appropriate to capture the non-linearity.

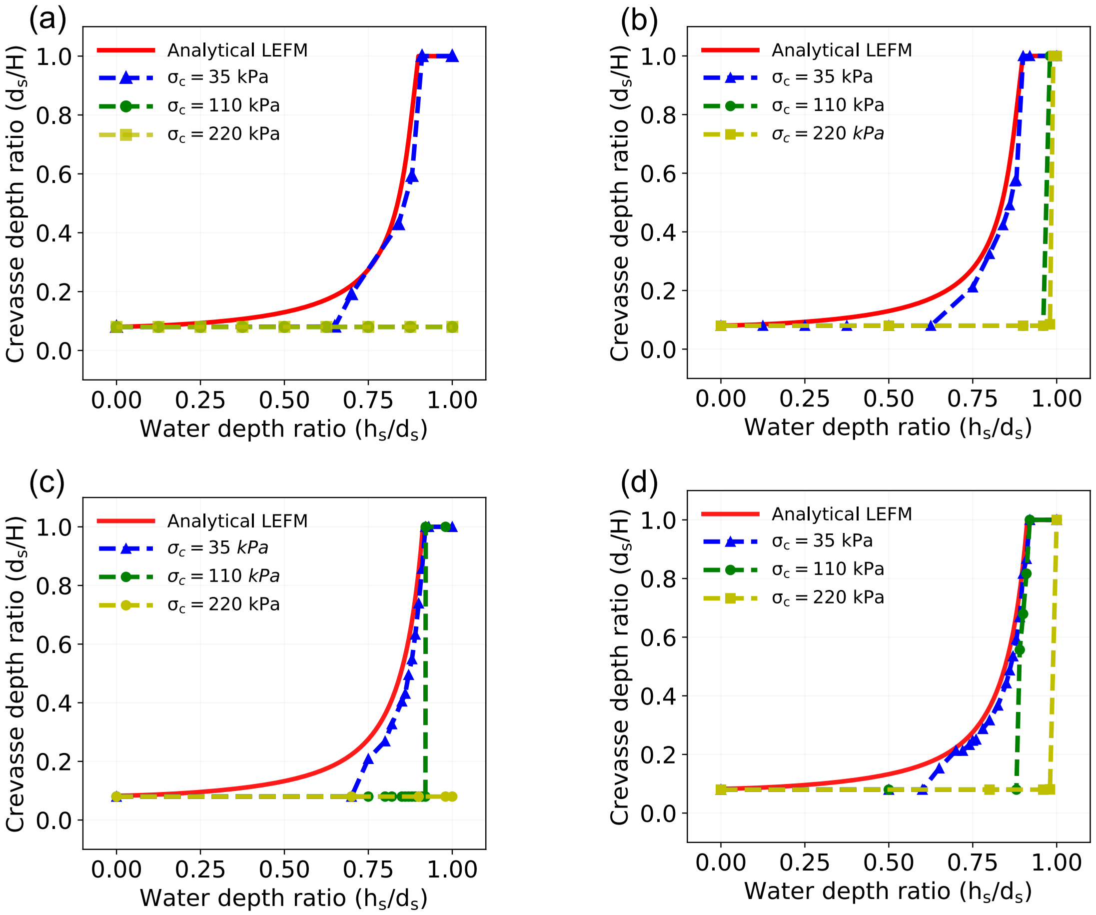

Figure 4.7: Surface crevasse depth $d_s$ normalized with the domain height H vs fresh water levels $h_s$ normalized with the Surface crevasse depth $d_s$ using CZM for different cohesive strength considering (a) linear elastic rheology of ice at near flotation grounded glacier, (b) non-linear visco-elastic rheology of ice at near flotation grounded glacier, (c) linear elastic rheology of ice at floating ice shelf, and (d) non-linear visco-elastic rheology of ice at floating ice shelf. The results are compared with the analytically obtained LEFM solution.

Now, we consider the effect of viscous strain in predicting the crevasse depth in addition to the elastic strain. In order to do so, we followed the linear viscoelastic formulation proposed by [152] for poly-crystalline ice, and implemented it in ABAQUS using a user-defined material subroutine (UMAT). We assumed the viscosity coefficient parameter as $1.58825 \times 10^{-7}$ Pa-s, and the viscosity exponent parameter as 3 for non-linear visco-elastic rheology. The results from near flotation grounded glacier and floating ice shelf are plotted in Fig. 4.7 (b) and (d), respectively. The key observation is as follows:

1. unlike the linear elastic case, here if the crevasse is almost 100% filled with melt-water, it propagates even for the higher cohesive strength values in the near flotation case. For the floating ice shelf also, we see a similar behavior. Which can be explained form the fact that the inclusion of viscous effects facilitated the crack propagation by making sure the crack-separation in the cohesive zone exceeds the maximum separation. As our damage model is developed on the separation-based criteria, once the equivalent separation exceeds the maximum separation, the cohesive elements fail and crack propagation occurs.

So, the extending question from this discussion is: why do we see crack propagation in an ice shelf even for higher cohesive strength values considering ice as a non-linear visco-elastic material unlike in the case when it is considered as linear elastic? To explain these observations, we have performed a study on crack opening vs time and crevasse depth vs time in an element near the crack tip for floating ice shelf. In Fig. 4.8 (a) and (b), how the equivalent crack separation evolves over time in a crack tip element for linear elastic and non-linear visco-elastic rheology, respectively have been plotted. The key observations are as follows:

1. In the linear elastic case, we see that although for lower cohesive strength values, the equivalent separation exceeds the maximum separation values (shown by dashed lines) corresponding to respective cohesive strengths, for the 220 kPa case, it fails to

reach that limit. As a result, for lower cohesive strengths, non-linearity gets introduced in the model, and progressive damage accumulation happens, which further facilitates crack propagation and complete failure of a cohesive element. Whereas, in the 220 kPa case, the equivalent separation never reaches the maximum separation limit, which is essential for a complete failure of an element and crack propagation; thus we observe a crack arrest as shown in Fig. 4.7 (c). It is important to note that in our model, we didn't account for ice strengthening mechanisms, which can further arrest cracks. In a future work, we can modify our present damage model to include such effects.

2. Whereas, when we consider ice as a non-linear visco-elastic material, the equivalent separation exceeds the corresponding maximum separation at the crack tip element for all three cohesive strengths (see Fig. 4.8 (b)), and as result of that we observe crack propagation in all three cases (see Fig. 4.7 (d)). The inclusion of time dependent viscous strain into the model helps to increase the crack driving force and once the separation exceeds the maximum separation limit, damage nucleation starts, which culminates into the crevasse propagation in the ice shelf.

Another important point in this discussion is whether the crevasse propagation is a time dependent effect and how the rate of crack propagation affects calving events? To answer that, we have plotted the crack propagation vs time data for a crack tip element in Fig. 4.8 (c) and (d). It can be clearly observed from Fig. 4.8 (d), for a non-linear visco-elastic rheology, there is a delayed effect in the crack propagation depending on the choice of cohesive strengths, but eventually in all the cases crevasse penetrates the whole ice shelf, i.e., calving occurs. So, the effect of non-linearity is important to capture the time dependent event, which can lead to periodic calving in the ice shelf.

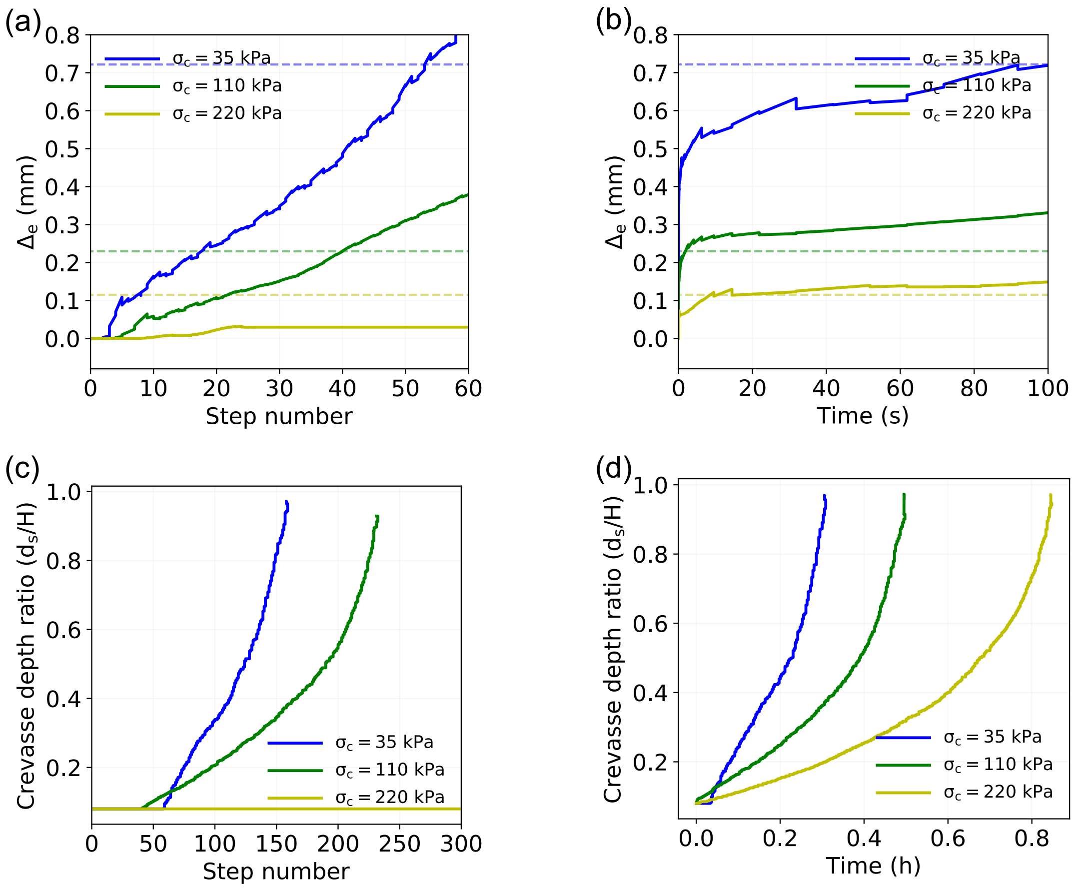

Figure 4.8: Equivalent Crack separation evalution over time in a crack tip element of a floating ice shelf using CZM for different cohesive strength considering (a) linear elastic rheology of ice, and (b)non-linear visco-elastic rheology of ice; Rate of crevasse propagation in a crack tip element of a floating ice shelf using CZM for different cohesive strength considering (a) linear elastic rheology of ice, and (b)non-linear visco-elastic rheology of ice

### 4.4.2 Effect of Elastic Modulus on Crevasse Depth Prediction

Now, we try to address the uncertainty regarding the choice of Young's modulus value for glacier ice. This is important because it has been established in the literature [195] that the elastic stress is dependent on the modulus of elasticity and thus can directly affect one's choice of tensile strength/cohesive strength parameter for reliable simulations. We have found that the researchers have considered a range of values as elastic modulus of ice (e.g., 4-10 GPa [196], 1-10 GPa [197]). In this work, we have chosen two representative elastic modulus values (1 GPa and 9.5 GPa, respectively), and test the sensitivity effects by varying cohesive strengths in the range of 35-220 kPa for near flotation grounded glacier and floating ice shelf, considering non-linear visco-elastic rheology. We plot the crevasse depth ratio vs freshwater depth ratio data obtained from the CZM model for grounded glacier and floating ice shelf in Fig. 4.9. The key observations are as follows:

1. For both the near flotation grounded glacier and the floating ice shelf, the predicted crevasse depth is sensitive to the choice of elastic modulus for higher cohesive strength values. Whereas, for a low cohesive strength, the crevasse depth is insensitive to the elastic modulus of ice. This observation highlights the fact that the researchers should be careful while choosing the elastic modulus of ice for modeling purpose, as depending on the choice of tensile strength/cohesive strength, the crevasse depth prediction can vary.

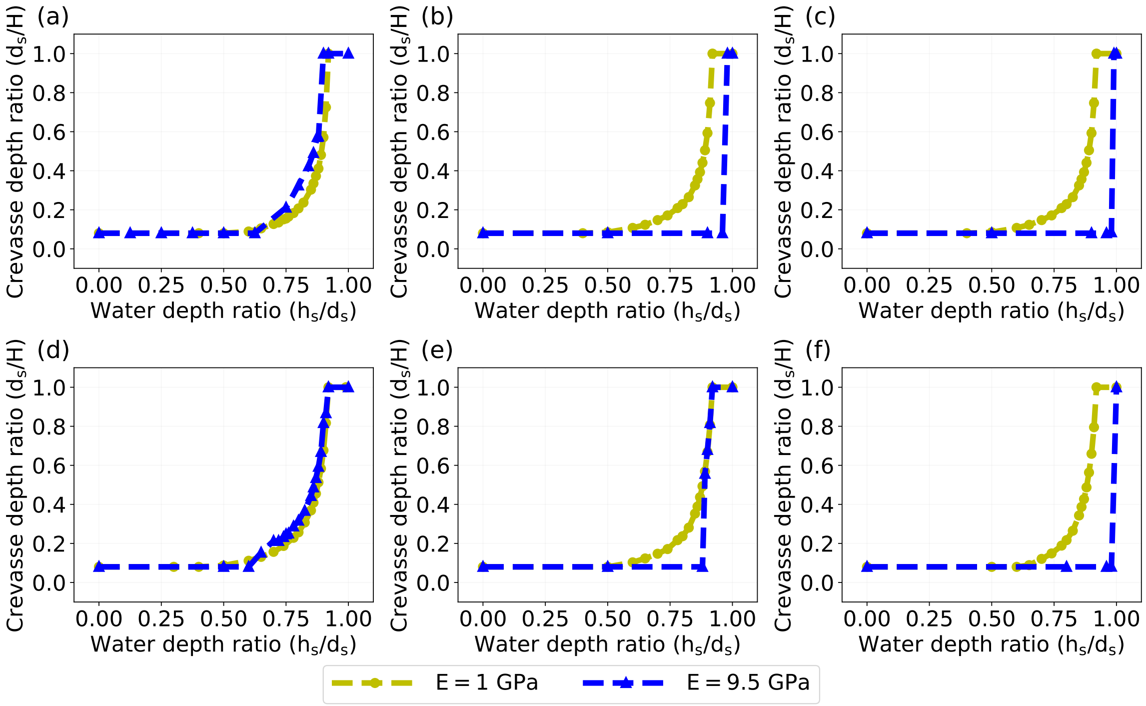

Figure 4.9: Surface crevasse depth $d_s$ normalized with the domain height H fresh water level $h_s$ normalized with the Surface crevasse depth $d_s$ obtained from the CZM solution for varying elastic modulus: Near flotation grounded glacier (a) 35 kPa, (b) 110 kPa, and (c) 220 kPa; Floating ice shelf (d) 35 kPa, (e) 110 kPa, and (f) 220 kPa.

In Fig. 4.10, we plotted the crevasse depth ratio vs fresh water depth ratio data for the near flotation glacier and floating ice shelf considering non-linear visco-elastic rheology of ice and elastic modulus values as 1 GPa and 9.5 GPa, respectively. From this figure, we observe the following:

1. If we choose the elastic modulus as 1 GPa, for both near flotation grounded glacier and floating ice shelf, the crevasse depth prediction is insensitive towards the choice of cohesive strength. In all the cases, the crevasse propagates and we don't observe any crack arrest phenomena. Whereas, if we choose the elastic modulus as 9.5 GPa, as we have discussed earlier there is sensitivity towards the choice of cohesive strength as well as the boundary condition.

### 4.4.3 Effect of Variation in Density and Temperature with Depth on Crevasse Depth Prediction

In this section, we investigate the role of variation in density with the height in predicting crevasse depth, i.e., whether one should consider a constant density all through the depth of the glacier ice, or change it along the depth? This issue stems from the following discussion: in the models of [146, 145] the ice density is assumed constant and the compressive overburden stress increases linearly with depth below the surface. However as pointed out by [144], the near-surface density of firn is considerably smaller ($\approx$ 350 kg/m$^3$) than that of solid ice ($\approx$ 917 kg/m$^3$). Consequently, the crevasse-closure effect from ice overburden may be over-estimated in prior models, in particular for shallow crevasses. A more appropriate approach is to explicitly include a density–depth profile to account for the lower densities in the upper firn layers. In order to do so, we followed the approach proposed in the work of [147], and considered the empirical relationship proposed by [186] to describe the variation of ice density with the depth. In Fig. 4.11, we have plotted the crevasse depth predicted by the CZM approach for constant and variable

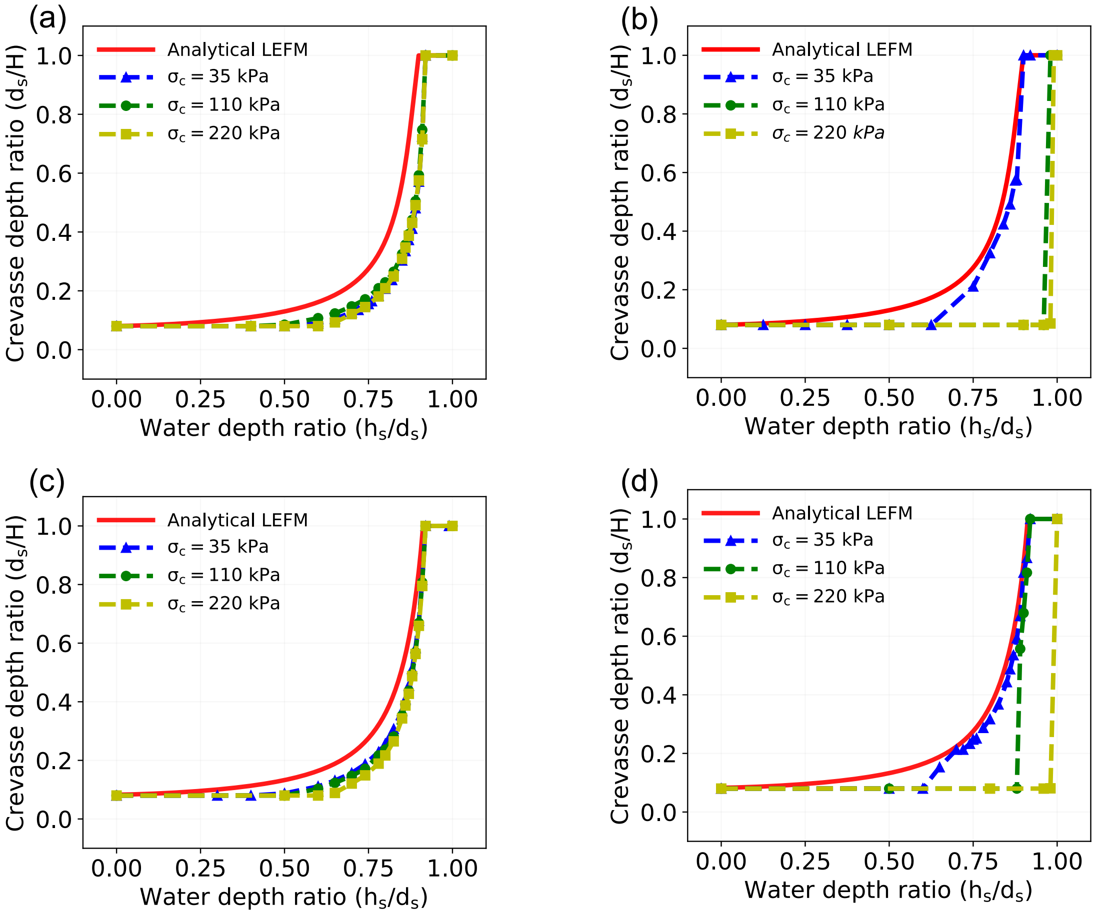

Figure 4.10: Surface crevasse depth $d_s$ normalized with the domain height H vs fresh water level $h_s$ normalized with the Surface crevasse depth $d_s$ obtained from the CZM simulation considering nonlinear visco-elastic rheology of ice : (a) E=1 GPa at near flotation grounded glacier, (b) E=9.5 GPa at near flotation grounded glacier, (c) E=1 GPa at floating ice shelf, and (d) E=9.5 GPa at floating ice shelf. The results are compared with the analytically obtained LEFM solution.

density cases by varying cohesive strength and freshwater present inside the crevasse in a near flotation grounded glacier. The key observations are as follows:

1. If we don't consider the variation in density with the depth, we tend to significantly overestimate the crevasse depth. This can be explained from the fact that when we consider the density is varying along the depth, the glacier is subjected to a smaller gravity load, and correspondingly the acting overburden stress is smaller, which leads to lesser number of cohesive elements exceeding the maximum crack separation

criteria unlike in the constant density case. When freshwater is present inside the crevasse and the cohesive strength is low, for a higher seawater cases, we even don't see any crack propagation in the variable density case, whereas the constant density case still has crack propagating. It can be explain from the fact that, when the cohesive strength is lower, the equivalent crack separation can cross the maximum separation threshold in the constant density case and the damage accumulation culminates into the crevasse propagation. Whereas, for a higher cohesive strength, the separation in a crack tip element fails to exceed the maximum separation threshold and subsequently we see crack arrest when the seawater depth is around 90%.

Now, as an extending discussion, we try to answer what is the possible effect of variable temperature and density, when combined on the crevasse depth prediction in a floating ice shelf. This is important to study because it is found that there can be water present at the base of the Antarctic ice shelves, while the top surface of the ice shelf can have much lower temperature, creating a poly-thermal ice shelf. In order to capture such polythermal behavior, we have considered the viscosity coefficient ($K_N$) to be dependent on temperature in the non-linear visco-elastic model. The viscosity coefficient is given by an Arrhenius type relation [198]

$$K_N(T) = K_N(T_m)exp(\frac{-Q}{R}(\frac{1}{T} - \frac{1}{T_m})), \tag{4.22}$$

where Q is the creep activation energy, R is the universal gas constant, and $K_N(T_m)$ is the viscosity coefficient at a reference temperature $T_m$. Here, we have conducted a set of simulations by varying the freshwater present in the crevasse (0% and 90%) and the cohesive strength in the range of 35-220 kPa. The final crevasse depth ratio values are listed for both the cases in Tables 4.2 and 4.3, and the key observations are as follows:

1. For the dry crevasse, when the temperature and density, both are constant along the depth, there is crack arrest in the floating ice shelf, unlike the variable temperature and variable density case. So, this shows that the variation of temperature and density

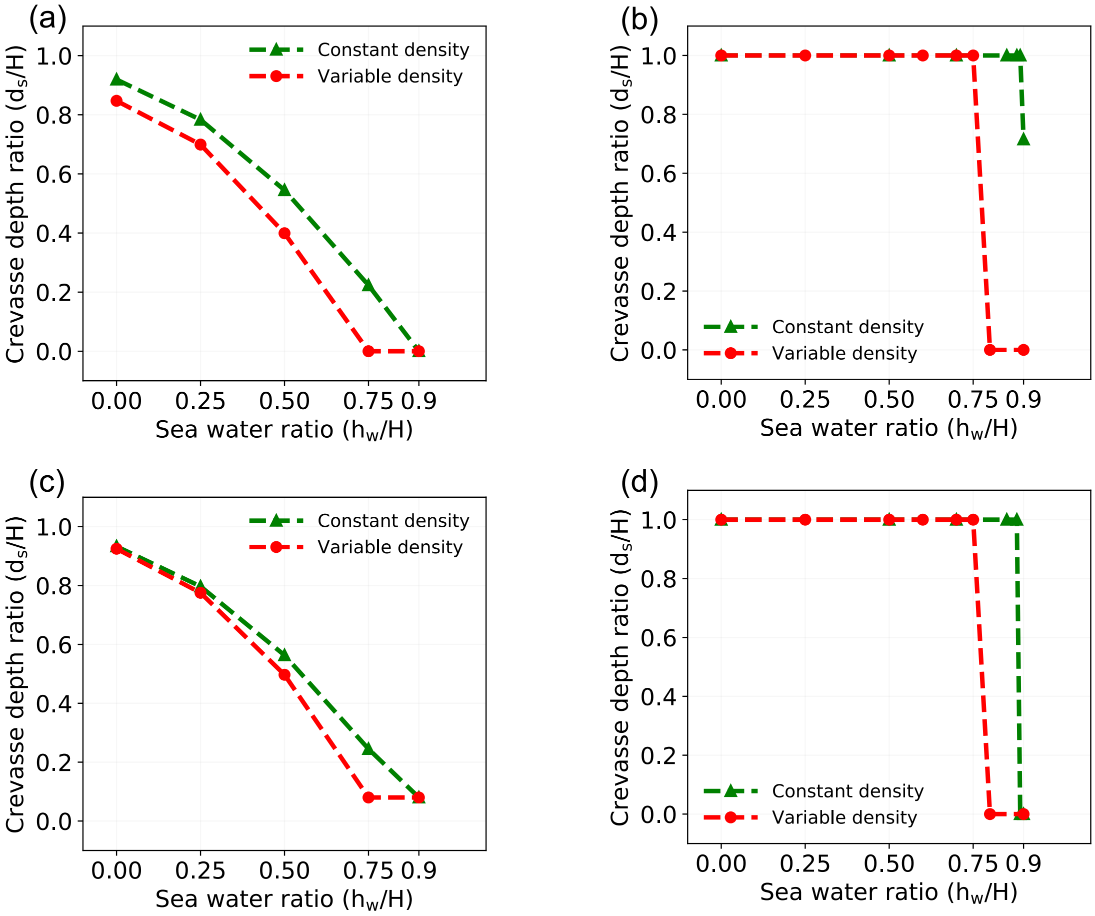

Figure 4.11: Surface crevasse depth $d_s$ normalized with the domain height H for varying sea water levels $h_w$ normalized with the domain height H obtained from the CZM solution of grounded glacier for constant and variable density of ice over the depth: (a) dry crevasse for cohesive strength of 35 kPa, and (b) 90% freshwater in the crevasse for cohesive strength of 35 kPa (c) dry crevasse for cohesive strength of 220 kPa, and (d) 90% freshwater in the crevasse for cohesive strength of 220 kPa

along the depth of the ice shelf provides an additional crack driving force, which helps in propagating crevasse, and as the cohesive strength increase the maximum crevasse depth increases.

2. When there is 90% freshwater present in the crevasse, if the temperature and density both varies, complete penetration/calving can occur in the ice shelf, unlike the constant density and temperature case. In the constant density and temperature case, as the cohesive strength is increased the extent of crevasse propagation decreases, sug-

gesting the stress state in the ice shelf gradually becoming suitable for crack arrest.

Table 4.2: Effect of density and temperature on final crevasse depth ratio in floating ice shelf with a dry crevasse.

| Cohesive Strength (kPa) | Constant Temperature and Density | Variable Temperature and Density |
|---|---|---|
| 35 | 0.08 | 0.116 |
| 110 | 0.08 | 0.209 |
| 220 | 0.08 | 0.225 |

Table 4.3: Effect of density and temperature on final crevasse depth ratio in floating ice shelf with 90% freshwater present in the crevasse.

| Cohesive Strength (kPa) | Constant Temperature and Density | Variable Temperature and Density |
|---|---|---|
| 35 | 0.816 | 1 |
| 110 | 0.68 | 1 |
| 220 | 0.08 | 1 |

## 4.5 Conclusions

We have proposed a poro-damage mechanics based cohesive zone approach for modeling hydro-fracture and crevasse propagation in glaciers. In our formulation, we interpret damage to represent the ratio of isotropic void area to total area along the cohesive interface, we assume that water can permeate the damaged material and exert hydro-static pressure along the interface. The proposed model has been implemented in the commercial software ABAQUS through user-defined subroutines. In this work, we investigate the influence of ice rheology and the tensile strength on crevasse penetration in glaciers and ice shelves by performing a series of numerical studies using the augmented cohesive zone model (CZM). We also address the effect of variation of density and temperature along the depth on accurate prediction of crevasse depth in grounded glaciers and floating ice-shelves. The key findings from our study can be summarized as follows:

1. If the ice is modeled as a linear elastic material, the predicted crevasse depth from the nonlinear CZM model shows an excellent match with the analytical LEFM solu-

tion in both glaciers and ice shelves. We also observe that the threshold strength for crack arrest in the grounded glacier is much lower than the ice shelf, indicating the ice shelves are more vulnerable to the calving events. Whereas, if we model ice as a non-linear visco-elastic material, the threshold strength for crack arrest in grounded glacier increases significantly. To support this observation, we investigated the evolution of crack separation in a crack tip element, and saw that the inclusion of viscous effects into the model facilitates failure of more cohesive elements, increasing the risks of crevasse propagation.

2. The choice of elastic modulus can significantly affect the predicted crevasse depth in both grounded glaciers and floating ice shelf. Our study finds that a lower elastic modulus value is insensitive to the choice of cohesive strength unlike the higher elastic modulus value. It shows that a choice of lower elastic modulus is more likely to cause a calving event in comparison to the higher elastic modulus case.

3. If we consider a variable density profile along the height of a glacier, the predicted crevasse depth gets lowered significantly in comparison to a constant density case. Whereas, in the ice shelf, as we vary both temperature and density along the height to represent real scenario, the chances of calving increases significantly in comparison to the constant temperature and density model.

# Chapter 5

# CONCLUSIONS

This dissertation presented robust damage mechanics-based cohesive zone modeling approaches and their applications to composite delamination and hydrofracturing of glaciers. A stabilized Nitsche-based finite element approach is developed and it's accuracy, stability for composite delamination analysis through numerical validation and verification studies is established. A poro-damage mechanics-based cohesive zone modeling approach for simulating hydrofracture in glaciers is also developed in thus study.

In Chapter 2, A stabilized finite element method that generalizes Nitsche's method for enforcing stiff anisotropic cohesive laws with different normal and tangential stiffness is presented. For smaller values of cohesive stiffness, the stabilized method resembles the standard method, wherein the traction on the crack surface is enforced as a Neumann boundary condition. Conversely, for larger values of cohesive stiffness, the stabilized method resembles Nitsche's method, wherein the cohesive law is enforced as a kinematic constraint. Several numerical examples, in two-dimensions, are presented to compare the performance of the stabilized and standard methods. The results illustrate that the stabilized method enables accurate recovery of crack-face traction for stiff isotropic and anisotropic cohesive laws; whereas, the standard method is less accurate due to spurious traction oscillations. Also, the stabilized method could improve computational efficiency by allowing the use of larger displacement increment in mixed-mode fracture simulation owing to its stability and accuracy.

In Chapter 3, the ability of a stabilized finite element method, inspired by the weighted Nitsche approach is demonstrated to alleviate spurious oscillations in the traction fields at interlaminar interfaces in multi-ply multi-directional composite laminates. This is achieved by defining a weighted interface traction such that it allows a gradual transition from the penalty-like method for soft elastic contact to the Nitsche-like method for rigid contact. To investigate numerical stability, several simulation studies involving constant strain patch tests and benchmark delamination tests under mode-I, mode-II and mixed-mode loadings are conducted. The results show clear evidence of traction oscillations with the standard method with structured and perturbed finite element meshes, and that the stabilized method alleviates these oscillations, thus illustrating its robustness.

In Chapter 4, hydrofracture-driven crevasse propagation in idealized glaciers and ice shelves using cohesive zone models based on the notion of poro-damage mechanics is investigated. The poro-damage cohesive zone model describes nonlinear fracture initiation and propagation along the potential crevasse interface, including the effect of hydrostatic pressure for a water-filled crevasse. Two commonly used rheological models for glacier ice, namely linear elastic and nonlinear viscoelastic, are considered and their predictions of crevasse depths are compared. Also the parametric sensitivity of crevasse depth predictions with respect to elastic modulus and tensile (cohesive) strength parameters are explored, and its implications for calving from glaciers and ice shelves are discussed. Finally, the consequences of varying density and temperature profiles on crevasse penetration are investigated. The major finding is that non-linear visco-elastic ice is more prone to calving than when modeled as a linear elastic one. It is also observed that depending on the choice of elastic modulus, there can be a significant sensitivity towards the choice of tensile strength. As a future work on this topic, the proposed model can be validated with relevant experiments.

# Appendix A

## Effect of Poisson's Ratio on Glacier Ice

For decades, there have been many studies and discussions on determining the compressibility of ice [199, 188] as it is an important property to be known to get an accurate numerical model, which can capture the physics of the problem. So, here we investigate for a grounded glacier, whether ice should be considered as an in-compressible material or a compressible material? To answer this question, we ran a couple of test cases with varying sea-water level to compare the different stress-components arising in the grounded glacier for two scenarios: (i) assumed ice as an in-compressible elastic material; and (ii) assumed ice as a compressible material and considered Cathles's theory to account for the initial overburden pressure correction as suggested by [190]. In Tables A.1 and A.2, the normalized root mean square (NRMS) error of each stress components between the above mentioned scenarios has been listed for varying seawater levels (0% and 90%) at the right terminus, respectively. The normalized error norm is calculated as

$$\frac{||\varepsilon_{S_{ij}}||_2}{||S^*_{ij}||_2} = \frac{\sqrt{\sum_{k=1}^{N_{\mathrm{GP}}} \left(S^k_{ij} - S^{*k}_{ij}\right)^2}}{\sqrt{\sum_{k=1}^{N_{\mathrm{GP}}} \left(S^{*k}_{ij}\right)^2}}; \tag{A.1}$$

where $N_{\mathrm{GP}}$ is the total number of Gauss (integration) points in the bulk elements, $\mathrm{S}_{ij}$ is the stress component obtained from Cathles's theory, and the reference stress component from incompressible elastic theory is denoted by $\mathrm{S}^*_{ij}$, respectively. The results clearly indicate that for a range of Poisson's ratio values varying from 0-0.495, the stress solutions from incompressible elastic material assumption agrees extremely well with the compressible elastic material consideration accounting for the Cathles's theory based corrections.

Thus, it can be safely concluded that we can assume ice as an incompressible material for simulating the grounded glacier and don't have to account for the Cathles's theory to get accurate predictions.

Table A.1: NRMS error of each stress component for grounded glacier for zero seawater level.

| Poisson's Ratio | $\frac{\|\|\varepsilon_{S_{11}}\|\|_2}{\|\|S_{11}^*\|\|_2}$ | $\frac{\|\|\varepsilon_{S_{12}}\|\|_2}{\|\|S_{12}^*\|\|_2}$ | $\frac{\|\|\varepsilon_{S_{22}}\|\|_2}{\|\|S_{22}^*\|\|_2}$ |
|---|---|---|---|
| 0 | 0.0053 | 0.0056 | 0.0015 |
| 0.1 | 0.0053 | 0.0056 | 0.0018 |
| 0.2 | 0.0053 | 0.0056 | 0.0018 |
| 0.35 | 0.0053 | 0.0056 | 0.0018 |
| 0.495 | 0.0051 | 0.0055 | 0.0009 |

Table A.2: NRMS error of each stress component for grounded glacier for 90% seawater level.

| Poisson's Ratio | S11 $\frac{\|\|\varepsilon_{S_{11}}\|\|_2}{\|\|S_{11}^*\|\|_2}$ | S12 $\frac{\|\|\varepsilon_{S_{12}}\|\|_2}{\|\|S_{12}^*\|\|_2}$ | S22 $\frac{\|\|\varepsilon_{S_{22}}\|\|_2}{\|\|S_{22}^*\|\|_2}$ |
|---|---|---|---|
| 0 | 0.0045 | 0.0271 | 0.0009 |
| 0.1 | 0.0045 | 0.0271 | 0.001 |
| 0.2 | 0.0045 | 0.0271 | 0.001 |
| 0.35 | 0.0045 | 0.0271 | 0.0009 |
| 0.495 | 0.0045 | 0.0272 | 0.0009 |

We conducted a similar study for the floating ice shelf. The results follows a similar trend as observed in the grounded glacier case as evident from Table A.3, and we can thus safely assume ice as an in-compressible material for all the simulations.

Table A.3: NRMS error of each stress component for floating ice shelf.

| Poisson's Ratio | $S_{11}$ $\frac{\|\|\varepsilon_{S_{11}}\|\|_2}{\|\|S^*_{11}\|\|_2}$ | $S_{12}$ $\frac{\|\|\varepsilon_{S_{12}}\|\|_2}{\|\|S^*_{12}\|\|_2}$ | $S_{22}$ $\frac{\|\|\varepsilon_{S_{22}}\|\|_2}{\|\|S^*_{22}\|\|_2}$ |
|---|---|---|---|
| 0 | 0.0004 | 0.0029 | 0.0003 |
| 0.1 | 0.0004 | 0.0029 | 0.0004 |
| 0.2 | 0.0004 | 0.0029 | 0.0004 |
| 0.35 | 0.0004 | 0.0029 | 0.0004 |
| 0.495 | 0.0002 | 0.0017 | $6.2\times10^{-5}$ |

# BIBLIOGRAPHY

[1] Y. Mi, M.A. Crisfield, G.A.O. Davies, and H.B. Hellweg. Progressive delamination using interface elements. *Journal of Composite Materials*, 32(14):1246–1272, 1998.

[2] L.E. Asp, A. Sjögren, and E.S. Greenhalgh. Delamination growth and thresholds in a carbon/epoxy composites under fatigue loading. *Journal of Composites Technology & Research*, 23(2):55–68, 2001.

[3] P.W. Harper and S.R. Hallet. Cohesive zone length in numerical simulations of composite delamination. *Engineering Fracture Mechanics*, 75(16):4774–4792, 2008.

[4] L.F. Kawashita and S.R. Hallett. A crack tip tracking algorithm for cohesive interface element analysis of fatigue delamination propagation in composite materials. *International Journal of Solids and Structures*, 49(21):2898 – 2913, 2012.

[5] W.G. Jiang, S.R. Hallett, B.G. Green, and M.R. Wisnom. A concise interface constitutive law for analysis of delamination and splitting in composite materials and its application to scaled notched tensile specimens. *International Journal for Numerical Methods in Engineering*, 69(9):1982–1995, 2007.

[6] J. Lemaitre. *A course on damage mechanics*. Springer Science & Business Media, 2012.

[7] L.M. Kachanov. Time of the rupture process under creep conditions. *Nank SSR Otd Tech Nauk*, 8:26–31, 1958.

[8] Y.N. Rabotnov. On the equation of state of creep. In *Proceedings of the Institution of Mechanical Engineers, Conference Proceedings*, volume 178, pages 2–117. SAGE Publications Sage UK: London, England, 1963.

[9] J. Lemaitre. Evaluation of dissipation and damage in metals. In *Proc. ICM Kyoto*, volume 1, 1971.

[10] F. Sidoroff. Description of anisotropic damage application to elasticity. In *Physical Non-Linearities in Structural Analysis*, pages 237–244. Springer, 1981.

[11] V.P. Nguyen. Discontinuous Galerkin/extrinsic cohesive zone modeling: Implementation caveats and applications in computational fracture mechanics. *Engineering Fracture Mechanics*, 128:37–68, 2014.

[12] A. Simone. Partition of unity-based discontinuous elements for interface phenomena: computational issues. *International Journal for Numerical Methods in Biomedical Engineering*, 20(6):465–478, 2004.

[13] N. Blal, L. Daridon, Y. Monerie, and S. Pagano. Artificial compliance inherent to the intrinsic cohesive zone models: criteria and application to planar meshes. *International Journal of Fracture*, 178(1-2):71–83, 2012.

[14] E. Svenning. A weak penalty formulation remedying traction oscillations in interface elements. *Computer Methods in Applied Mechanics and Engineering*, 310:460–474, 2016.

[15] R. Radovitzky, A. Seagraves, M. Tupek, and L. Noels. A scalable 3D fracture and fragmentation algorithm based on a hybrid, discontinuous Galerkin, cohesive element method. *Computer Methods in Applied Mechanics and Engineering*, 200(1):326–344, 2011.

[16] J. Nitsche. Über ein Variationsprinzip zur Lösung von Dirichlet-Problemen bei Verwendung von Teilräumen, die keinen Randbedingungen unterworfen sind. In *Abhandlungen aus dem mathematischen Seminar der Universität Hamburg*, volume 36, pages 9–15. Springer, 1971.

[17] A. Hansbo and P. Hansbo. A finite element method for the simulation of strong and weak discontinuities in solid mechanics. *Computer Methods in Applied Mechanics and Engineering*, 193(33-35):3523–3540, 2004.

[18] C. Annavarapu, M. Hautefeuille, and J.E. Dolbow. A robust Nitsche's formulation for interface problems. *Computer Methods in Applied Mechanics and Engineering*, 225:44–54, 2012.

[19] C. Annavarapu, M. Hautefeuille, and J.E. Dolbow. A Nitsche stabilized finite element method for frictional sliding on embedded interfaces. Part I: single interface. *Computer Methods in Applied Mechanics and Engineering*, 268:417–436, 2014.

[20] C. Annavarapu, R.R. Settgast, S.M. Johnson, P. Fu, and E.B. Herbold. A weighted Nitsche stabilized method for small-sliding contact on frictional surfaces. *Computer Methods in Applied Mechanics and Engineering*, 283:763–781, 2015.

[21] J. Mergheim, E. Kuhl, and P. Steinmann. A finite element method for the computational modelling of cohesive cracks. *International Journal for Numerical Methods in Engineering*, 63(2):276–289, 2005.

[22] G. Ghosh, R. Duddu, and C. Annavarapu. A stabilized finite element method for enforcing stiff anisotropic cohesive laws using interface elements. *Computer Methods in Applied Mechanics and Engineering*, 348:1013–1038, 2019.

[23] R.B. Alley, T.K. Dupont, B.R. Parizek, and S. Anandakrishnan. Access of surface meltwater to beds of sub-freezing glaciers: preliminary insights. *Annals of Glaciology*, 40:8–14, 2005.

[24] L.A. Stearns, B.E. Smith, and G.S. Hamilton. Increased flow speed on a large East Antarctic outlet glacier caused by subglacial floods. *Nature Geoscience*, 1(12):827–831, 2008.

[25] S.B. Das, I. Joughin, M.D. Behn, I.M. Howat, M.A. King, D. Lizarralde, and M.P. Bhatia. Fracture propagation to the base of the Greenland Ice Sheet during supraglacial lake drainage. *Science*, 320(5877):778–781, 2008.

[26] J.N. Bassis and Y. Ma. Evolution of basal crevasses links ice shelf stability to ocean forcing. *Earth and Planetary Science Letters*, 409:203–211, 2015.

[27] K.E. Alley, T.A. Scambos, J.Z. Miller, D.G. Long, and M. MacFerrin. Quantifying vulnerability of Antarctic ice shelves to hydrofracture using microwave scattering properties. *Remote sensing of environment*, 210:297–306, 2018.

[28] G. T. Camacho and M. Ortiz. Computational modelling of impact damage in brittle materials. *International Journal of Solids and Structures*, 33(20-22):2899–2938, 1996.

[29] E.A. Repetto, R. Radovitzky, and M. Ortiz. Finite element simulation of dynamic fracture and fragmentation of glass rods. *Computer Methods in Applied Mechanics and Engineering*, 183(1-2):3–14, 2000.

[30] I. Arias, J. Knap, V.B. Chalivendra, S. Hong, M. Ortiz, and A.J. Rosakis. Numerical modelling and experimental validation of dynamic fracture events along weak planes. *Computer Methods in Applied Mechanics and Engineering*, 196(37-40):3833–3840, 2007.

[31] A. Seagraves and R. Radovitzky. Advances in cohesive zone modeling of dynamic fracture. In *Dynamic failure of materials and structures*, pages 349–405. Springer, 2009.

[32] Z. J. Zhang, G.H. Paulino, and W. Celes. Extrinsic cohesive modelling of dynamic fracture and microbranching instability in brittle materials. *International Journal for Numerical Methods in Engineering*, 72(8):893–923, 2007.

[33] J.F. Molinari, G. Gazonas, R. Raghupathy, A. Rusinek, and F. Zhou. The cohesive element approach to dynamic fragmentation: the question of energy convergence. *International Journal for Numerical Methods in Engineering*, 69(3):484–503, 2007.

[34] C-H. Sam, K.D. Papoulia, and S.A. Vavasis. Obtaining initially rigid cohesive finite element models that are temporally convergent. *Engineering Fracture Mechanics*, 72(14):2247–2267, 2005.

[35] R. Espinha, K. Park, G.H. Paulino, and W. Celes. Scalable parallel dynamic fracture simulation using an extrinsic cohesive zone model. *Computer Methods in Applied Mechanics and Engineering*, 266:144–161, 2013.

[36] K. Park, G.H. Paulino, W. Celes, and R. Espinha. Adaptive mesh refinement and coarsening for cohesive zone modeling of dynamic fracture. *International Journal for Numerical Methods in Engineering*, 92(1):1–35, 2012.

[37] A. Mota, J. Knap, and M. Ortiz. Fracture and fragmentation of simplicial finite element meshes using graphs. *International Journal for Numerical Methods in Engineering*, 73(11):1547–1570, 2008.

[38] R.R. Settgast, P. Fu, S.D.C. Walsh, J.A. White, C. Annavarapu, and F.J. Ryerson. A fully coupled method for massively parallel simulation of hydraulically driven fractures in 3-dimensions. *International Journal for Numerical and Analytical Methods in Geomechanics*, 41(5):627–653, 2017.

[39] X.P. Xu and A. Needleman. Numerical simulations of fast crack growth in brittle solids. *Journal of the Mechanics and Physics of Solids*, 42(9):1397–1434, 1994.

[40] F.H. Wittmann, K. Rokugo, E. Brühwiler, H. Mihashi, and P. Simonin. Fracture energy and strain softening of concrete as determined by means of compact tension specimens. *Materials and Structures*, 21(1):21–32, 1988.

[41] V. Tvergaard and J. W. Hutchinson. The influence of plasticity on mixed mode interface toughness. *Journal of the Mechanics and Physics of Solids*, 41(6):1119–1135, 1993.

[42] I. Scheider and W. Brocks. Simulation of cup–cone fracture using the cohesive model. *Engineering Fracture Mechanics*, 70(14):1943–1961, 2003.

[43] V. Tvergaard. Effect of fibre debonding in a Whisker-reinforced metal. *Materials Science and Engineering: A*, 125(2):203–213, 1990.

[44] K. Park, G. H. Paulino, and J. R. Roesler. A unified potential-based cohesive model of mixed-mode fracture. *Journal of the Mechanics and Physics of Solids*, 57(6):891–908, 2009.

[45] X.P. Xu and A. Needleman. Void nucleation by inclusion debonding in a crystal matrix. *Modelling and Simulation in Materials Science and Engineering*, 1(2):111, 1993.

[46] J.C.J. Schellekens and R. De Borst. A non-linear finite element approach for the analysis of mode-I free edge delamination in composites. *International Journal of Solids and Structures*, 30(9):1239–1253, 1993.

[47] G. Alfano and M.A. Crisfield. Finite element interface models for the delamination analysis of laminated composites: mechanical and computational issues. *International Journal for Numerical Methods in Engineering*, 50(7):1701–1736, 2001.

[48] X. Liu, R. Duddu, and H. Waisman. Discrete damage zone model for fracture initiation and propagation. *Engineering Fracture Mechanics*, 92:1–18, 2012.

[49] W. Wagner, F. Gruttmann, and W. Sprenger. A finite element formulation for the simulation of propagating delaminations in layered composite structures. *International Journal for Numerical Methods in Engineering*, 51(11):1337–1359, 2001.

[50] H.D. Espinosa and P.D. Zavattieri. A grain level model for the study of failure initiation and evolution in polycrystalline brittle materials. part I: Theory and numerical implementation. *Mechanics of Materials*, 35(3):333–364, 2003.

[51] S.H. Song, G.H. Paulino, and W.G. Buttlar. A bilinear cohesive zone model tailored for fracture of asphalt concrete considering viscoelastic bulk material. *Engineering Fracture Mechanics*, 73(18):2829–2848, 2006.

[52] A. Turon, C.G. Davila, P.P. Camanho, and J. Costa. An engineering solution for mesh size effects in the simulation of delamination using cohesive zone models. *Engineering Fracture Mechanics*, 74(10):1665 – 1682, 2007.

[53] P.H. Geubelle and J.S. Baylor. Impact-induced delamination of composites: a 2D simulation. *Composites Part B: Engineering*, 29(5):589–602, 1998.

[54] J.C.J. Schellekens and R. De Borst. On the numerical integration of interface elements. *International Journal for Numerical Methods in Engineering*, 36(1):43–66, 1993.

[55] R. De Borst. Numerical aspects of cohesive-zone models. *Engineering Fracture Mechanics*, 70(14):1743–1757, 2003.

[56] I. Babuška. The finite element method with penalty. *Mathematics of Computation*, 27(122):221–228, 1973.

[57] E. Lorentz. A mixed interface finite element for cohesive zone models. *Computer Methods in Applied Mechanics and Engineering*, 198(2):302–317, 2008.

[58] F. Cazes, M. Coret, and A. Combescure. A two-field modified lagrangian formulation for robust simulations of extrinsic cohesive zone models. *Computational Mechanics*, 51(6):865–884, 2013.

[59] É. Béchet, N. Moës, and B. Wohlmuth. A stable Lagrange multiplier space for stiff interface conditions within the extended finite element method. *International Journal for Numerical Methods in Engineering*, 78(8):931–954, 2009.

[60] G. Ferté, P. Massin, and N. Moës. Interface problems with quadratic X-FEM: design of a stable multiplier space and error analysis. *International Journal for Numerical Methods in Engineering*, 100(11):834–870, 2014.

[61] H. Ji and J.E. Dolbow. On strategies for enforcing interfacial constraints and evaluating jump conditions with the extended finite element method. *International Journal for Numerical Methods in Engineering*, 61(14):2508–2535, 2004.

[62] J. Douglas and T. Dupont. Interior penalty procedures for elliptic and parabolic Galerkin methods. *Computing Methods in Applied Sciences*, pages 207–216, 1976.

[63] A. Johansson and M.G. Larson. A high order discontinuous Galerkin Nitsche method for elliptic problems with fictitious boundary. *Numerische Mathematik*, 123(4):607–628, 2013.

[64] P. Hansbo. Nitsche's method for interface problems in computational mechanics. *GAMM-Mitteilungen*, 28(2):183–206, 2005.

[65] D.N. Arnold, F. Brezzi, B. Cockburn, and L. D. Marini. Unified analysis of discontinuous Galerkin methods for elliptic problems. *SIAM Journal on Numerical Analysis*, 39(5):1749–1779, 2002.

[66] F. Liu and R.I. Borja. A contact algorithm for frictional crack propagation with the extended finite element method. *International Journal for Numerical Methods in Engineering*, 76(10):1489–1512, 2008.

[67] P. Wriggers and G. Zavarise. A formulation for frictionless contact problems using a weak form introduced by Nitsche. *Computational Mechanics*, 41(3):407–420, 2008.

[68] A. Hansbo and P. Hansbo. An unfitted finite element method, based on Nitsche's method, for elliptic interface problems. *Computer Methods in Applied Mechanics and Engineering*, 191(47):5537–5552, 2002.

[69] A. Fritz, S. Hüeber, and B.I. Wohlmuth. A comparison of mortar and Nitsche techniques for linear elasticity. *Calcolo*, 41(3):115–137, 2004.

[70] M.S. Fernández and A. Huerta. Imposing essential boundary conditions in mesh-free methods. *Computer Methods in Applied Mechanics and Engineering*, 193(12-14):1257–1275, 2004.

[71] J. Dolbow and I. Harari. An efficient finite element method for embedded interface problems. *International Journal for Numerical Methods in Engineering*, 78(2):229–252, 2009.

[72] E. Burman and P. Hansbo. Fictitious domain finite element methods using cut elements: II. A stabilized Nitsche method. *Applied Numerical Mathematics*, 62(4):328–341, 2012.

[73] C. Annavarapu, M. Hautefeuille, and J.E. Dolbow. Stable imposition of stiff constraints in explicit dynamics for embedded finite element methods. *International Journal for Numerical Methods in Engineering*, 92(2):206–228, 2012.

[74] J.D. Sanders, T.A. Laursen, and M.A. Puso. A Nitsche embedded mesh method. *Computational Mechanics*, 49(2):243–257, 2012.

[75] T.J. Truster and A. Masud. Primal interface formulation for coupling multiple PDEs: a consistent derivation via the variational multiscale method. *Computer Methods in Applied Mechanics and Engineering*, 268:194–224, 2014.

[76] T.J. Truster. A stabilized, symmetric Nitsche method for spatially localized plasticity. *Computational Mechanics*, 57(1):75–103, 2016.

[77] C. Annavarapu, M. Hautefeuille, and J.E. Dolbow. A Nitsche stabilized finite element method for frictional sliding on embedded interfaces. Part II: Intersecting interfaces. *Computer Methods in Applied Mechanics and Engineering*, 267:318 – 341, 2013.

[78] M. Juntunen and R. Stenberg. Nitsche's method for general boundary conditions. *Mathematics of Computation*, 78(267):1353–1374, 2009.

[79] S. Jiménez and R. Duddu. On the parametric sensitivity of cohesive zone models for high-cycle fatigue delamination of composites. *International Journal of Solids and Structures*, 82:111–124, 2016.

[80] S. Jiménez, X. Liu, R. Duddu, and H. Waisman. A discrete damage zone model for mixed-mode delamination of composites under high-cycle fatigue. *International Journal of Fracture*, 190(1-2):53–74, 2014.

[81] D. Versino, H. M. Mourad, C. G. Davila, and F. L. Addessio. A thermodynamically consistent discontinuous Galerkin formulation for interface separation. *Composite Structures*, 133:595 – 606, 2015.

[82] R. Abedi and R. B. Haber. Spacetime simulation of dynamic fracture with crack closure and frictional sliding. *Advanced Modeling and Simulation in Engineering Sciences*, 5(1):22, Sep 2018.

[83] S.C. Aduloju and T.J. Truster. A variational multiscale discontinuous galerkin formulation for both implicit and explicit dynamic modeling of interfacial fracture. *Computer Methods in Applied Mechanics and Engineering*, 343:602 – 630, 2019.

[84] R. Liu, M.F. Wheeler, and C.N. Dawson. A three-dimensional nodal-based implementation of a family of discontinuous Galerkin methods for elasticity problems. *Computers & Structures*, 87(3):141–150, 2009.

[85] K. Park and G.H. Paulino. Computational implementation of the PPR potential-based cohesive model in ABAQUS: educational perspective. *Engineering Fracture Mechanics*, 93:239–262, 2012.

[86] *Abaqus Analysis User's Guide, Version 6.14*. Dassault Systemes Simulia Corp., 2014.

[87] G. Ghosh, C. Annavarapu, S. Jiménez, and R. Duddu. A stabilized finite element method for modeling mixed-mode delamination of composites. In *Proceedings of the American Society for Composites: Thirty-Second Technical Conference, West Lafayette, IN, October 23–25*, pages 1–16, 2017.

[88] G. Ghosh, C. Annavarapu, and R. Duddu. A stabilized finite element formulation remedying traction oscillations in cohesive interface elements. In *Proceedings of the American Society for Composites: Thirty-third Technical Conference, Seattle, WA, September 24–26*, pages 1–14, 2018.

[89] S. Sadaba, I. Romero, C. Gonzalez, and J. Llorca. A stable X-FEM in cohesive transition from closed to open crack. *International Journal for Numerical Methods in Engineering*, 101(7):540–570, 2015.

[90] B. Lawn. *Fracture of Brittle Solids*. Cambridge Solid State Science Series. Cambridge University Press, 2 edition, 1993.

[91] W.L. Bradley and R.N. Cohen. Matrix deformation and fracture in graphite-reinforced epoxies. *Delamination and debonding of materials. ASTM STP 876, American Society for Testing and Materials*, pages 389–410, 1985.

[92] J.R. Reeder and J.H. Crews. Mixed-mode bending method for delamination testing. *AIAA Journal*, 28(7):1270–1276, 1990.

[93] K.J. Bathe and A. P. Cimento. Some practical procedures for the solution of nonlinear finite element equations. *Computer Methods in Applied Mechanics and Engineering*, 22(1):59–85, 1980.

[94] J.A. Pascoe, R.C. Alderliesten, and R. Benedictus. Methods for the prediction of fatigue delamination growth in composites and adhesive bonds–a critical review. *Engineering Fracture Mechanics*, 112:72–96, 2013.

[95] L. Banks-Sills. 50th anniversary article: review on interface fracture and delamination of composites. *Strain*, 50(2):98–110, 2014.

[96] P. P. Camanho, C. G. Davila, and M.F. De Moura. Numerical simulation of mixed-mode progressive delamination in composite materials. *Journal of Composite Materials*, 37(16):1415–1438, 2003.

[97] A. Turon, P.P. Camanho, J. Costa, and J. Renart. Accurate simulation of delamination growth under mixed-mode loading using cohesive elements: definition of interlaminar strengths and elastic stiffness. *Composite Structures*, 92(8):1857–1864, 2010.

[98] M. May and S.R. Hallett. A combined model for initiation and propagation of damage under fatigue loading for cohesive interface elements. *Composites Part A: Applied Science and Manufacturing*, 41(12):1787–1796, 2010.

[99] R. Higuchi, T. Okabe, and T. Nagashima. Numerical simulation of progressive damage and failure in composite laminates using XFEM/CZM coupled approach. *Composites Part A: Applied Science and Manufacturing*, 95:197–207, 2017.

[100] G.N. Wells and L.J. Sluys. A new method for modelling cohesive cracks using finite elements. *International Journal for Numerical Methods in Engineering*, 50(12):2667–2682, 2001.

[101] N. Moës and T. Belytschko. Extended finite element method for cohesive crack growth. *Engineering Fracture Mechanics*, 69(7):813–833, 2002.

[102] J.J.C Remmers, R. de Borst, and A. Needleman. A cohesive segments method for the simulation of crack growth. *Computational Mechanics*, 31(1-2):69–77, 2003.

[103] J.H. Song, P.M.A. Areias, and T. Belytschko. A method for dynamic crack and shear band propagation with phantom nodes. *International Journal for Numerical Methods in Engineering*, 67(6):868–893, 2006.

[104] S. Maiti, D. Ghosh, and G. Subhash. A generalized cohesive element technique for arbitrary crack motion. *Finite Elements in Analysis and Design*, 45(8-9):501–510, 2009.

[105] X. Zhang, D.R. Brandyberry, and P.H. Geubelle. IGFEM-based shape sensitivity analysis of the transverse failure of a composite laminate. *Computational Mechanics*, 64(5):1455–1472, 2019.

[106] J. Zhi, B.Y. Chen, and T.E. Tay. Geometrically nonlinear analysis of matrix cracking and delamination in composites with floating node method. *Computational Mechanics*, 63(2):201–217, 2019.

[107] T. Rabczuk and G. Zi. A meshfree method based on the local partition of unity for cohesive cracks. *Computational Mechanics*, 39(6):743–760, 2007.

[108] B. Dhas, M. Rahaman, K. Akella, D. Roy, and J.N. Reddy. A phase-field damage model for orthotropic materials and delamination in composites. *Journal of Applied Mechanics*, 85(1), 2018.

[109] F.A. Denli, O. Gültekin, G.A. Holzapfel, and H. Dal. A phase-field model for fracture of unidirectional fiber-reinforced polymer matrix composites. *Computational Mechanics*, pages 1–18, 2020.

[110] X. Lu, M. Ridha, B.Y. Chen, V.B.C. Tan, and T.E. Tay. On cohesive element parameters and delamination modelling. *Engineering Fracture Mechanics*, 206:278 – 296, 2019.

[111] Y. Freed and L. Banks-Sills. A new cohesive zone model for mixed mode interface fracture in bimaterials. *Engineering Fracture Mechanics*, 75(15):4583–4593, 2008.

[112] M.G.G.V. Elices, G.V. Guinea, J. Gomez, and J. Planas. The cohesive zone model: advantages, limitations and challenges. *Engineering Fracture Mechanics*, 69(2):137–163, 2002.

[113] Q. Yang and B. Cox. Cohesive models for damage evolution in laminated composites. *International Journal of Fracture*, 133(2):107–137, 2005.

[114] T. Q. Thai, T. Rabczuk, and X. Zhuang. Numerical study for cohesive zone model in delamination analysis based on higher-order B-spline functions. *Journal of Micromechanics and Molecular Physics*, 2(01):1750004, 2017.

[115] C.G. Dávila, P.P. Camanho, and A. Turon. Effective simulation of delamination in aeronautical structures using shells and cohesive elements. *Journal of Aircraft*, 45(2):663–672, 2008.

[116] C.G. Dávila, C.A. Rose, and P.P. Camanho. A procedure for superposing linear cohesive laws to represent multiple damage mechanisms in the fracture of composites. *International Journal of Fracture*, 158(2):211–223, 2009.

[117] Q.D. Yang, X.J. Fang, J.X. Shi, and J. Lua. An improved cohesive element for shell delamination analyses. *International Journal for Numerical Methods in Engineering*, 83(5):611–641, 2010.

[118] B.C. Do, W. Liu, Q.D. Yang, and X.Y. Su. Improved cohesive stress integration

schemes for cohesive zone elements. *Engineering Fracture Mechanics*, 107:14–28, 2013.

[119] W. Cui and M.R. Wisnom. A combined stress-based and fracture-mechanics-based model for predicting delamination in composites. *Composites*, 24(6):467–474, 1993.

[120] D. Xie and A.M. Waas. Discrete cohesive zone model for mixed-mode fracture using finite element analysis. *Engineering Fracture Mechanics*, 73(13):1783–1796, 2006.

[121] Y. Wang and H. Waisman. Progressive delamination analysis of composite materials using XFEM and a discrete damage zone model. *Computational Mechanics*, 55(1):1–26, 2015.

[122] T.J. Truster and A. Masud. A discontinuous/continuous Galerkin method for modeling of interphase damage in fibrous composite systems. *Computational Mechanics*, 52(3):499–514, 2013.

[123] R. Abedi and P.L. Clarke. A computational approach to model dynamic contact and fracture mode transitions in rock. *Computers and Geotechnics*, 109:248–271, 2019.

[124] J. Mergheim, E. Kuhl, and P. Steinmann. A hybrid discontinuous Galerkin/interface method for the computational modelling of failure. *International Journal for Numerical Methods in Biomedical Engineering*, 20(7):511–519, 2004.

[125] A. Seagraves and R. Radovitzky. Large-scale 3D modeling of projectile impact damage in brittle plates. *Journal of the Mechanics and Physics of Solids*, 83:48–71, 2015.

[126] V.P. Nguyen, C.T. Nguyen, S. Bordas, and A. Heidarpour. Modelling interfacial cracking with non-matching cohesive interface elements. *Computational Mechanics*, 58(5):731–746, 2016.

[127] H. R. Bayat, S. Rezaei, T. Brepols, and S. Reese. Locking-free interface failure modeling by a cohesive discontinuous galerkin method for matching and non-matching meshes. *International Journal for Numerical Methods in Engineering*, 121(8):1762–1790, 2019.

[128] J.D. Sanders, J.E. Dolbow, and T.A. Laursen. On methods for stabilizing constraints over enriched interfaces in elasticity. *International Journal for Numerical Methods in Engineering*, 78(9):1009–1036, 2009.

[129] A. Embar, J. Dolbow, and I. Harari. Imposing Dirichlet boundary conditions with Nitsche's method and spline-based finite elements. *International Journal for Numerical Methods in Engineering*, 83(7):877–898, 2010.

[130] J.N. Reddy and A. Miravete. *Practical analysis of composite laminates*. CRC press, 2018.

[131] S. R. Hallett, B. G. Green, W.G. Jiang, and M.R. Wisnom. An experimental and numerical investigation into the damage mechanisms in notched composites. *Composites Part A: Applied Science and Manufacturing*, 40(5):613–624, 2009.

[132] A. Jenkins and D. Holland. Melting of floating ice and sea level rise. *Geophysical Research Letters*, 34(16), 2007.

[133] M.F. Meier, M.B. Dyurgerov, U.K. Rick, S. O'neel, W. T. Pfeffer, R.S. Anderson, S.P. Anderson, and A.F. Glazovsky. Glaciers dominate eustatic sea-level rise in the 21st century. *Science*, 317(5841):1064–1067, 2007.

[134] A. Shepherd, D. Wingham, D. Wallis, K. Giles, S. Laxon, and A.V. Sundal. Recent loss of floating ice and the consequent sea level contribution. *Geophysical Research Letters*, 37(13), 2010.

[135] J.C. Moore, A. Grinsted, T. Zwinger, and S. Jevrejeva. Semiempirical and process-based global sea level projections. *Reviews of Geophysics*, 51(3):484–522, 2013.

[136] M.A. Depoorter, J.L. Bamber, J.A. Griggs, J.T.M. Lenaerts, S.R.M. Ligtenberg, M.R. van den Broeke, and G. Moholdt. Calving fluxes and basal melt rates of Antarctic ice shelves. *Nature*, 502(7469):89–92, 2013.

[137] M.A. Rist, P.R. Sammonds, S.A.F. Murrell, P.G. Meredith, C.S.M. Doake, H. Oerter, and K. Matsuki. Experimental and theoretical fracture mechanics applied to Antarctic ice fracture and surface crevassing. *Journal of Geophysical Research: Solid Earth*, 104(B2):2973–2987, 1999.

[138] W. Colgan, H. Rajaram, W. Abdalati, C. McCutchan, R. Mottram, M.S. Moussavi, and S. Grigsby. Glacier crevasses: Observations, models, and mass balance implications. *Reviews of Geophysics*, 54(1):119–161, 2016.

[139] J.F. Nye. The distribution of stress and velocity in glaciers and ice-sheets. *Proceedings of the Royal Society of London. Series A. Mathematical and Physical Sciences*, 239(1216):113–133, 1957.

[140] K.C. Jezek. A modified theory of bottom crevasses used as a means for measuring the buttressing effect of ice shelves on inland ice sheets. *Journal of Geophysical Research: Solid Earth*, 89(B3):1925–1931, 1984.

[141] D.I. Benn, N.R.J. Hulton, and R.H. Mottram. ‘calving laws’,‘sliding laws’ and the stability of tidewater glaciers. *Annals of Glaciology*, 46:123–130, 2007.

[142] R.H. Mottram and D.I. Benn. Testing crevasse-depth models: a field study at breiamerkurjökull, Iceland. *Journal of Glaciology*, 55(192):746–752, 2009.

[143] F.M. Nick, C.J. Van der Veen, A. Vieli, and D.I. Benn. A physically based calving

model applied to marine outlet glaciers and implications for the glacier dynamics. *Journal of Glaciology*, 56(199):781–794, 2010.

[144] M.A. Rist, P.R. Sammonds, S.A.F. Murrell, P.G. Meredith, H. Oerter, and C.S.M. Doake. Experimental fracture and mechanical properties of antarctic ice: preliminary results. *Annals of Glaciology*, 23:284–292, 1996.

[145] R.A. Smith. The application of fracture mechanics to the problem of crevasse penetration. *Journal of Glaciology*, 17(76):223–228, 1976.

[146] J. Weertman. Can a water-filled crevasse reach the bottom surface of a glacier. *IASH publ*, 95:139–145, 1973.

[147] C.J. Van der Veen. Fracture mechanics approach to penetration of surface crevasses on glaciers. *Cold Regions Science and Technology*, 27(1):31–47, 1998.

[148] C.J. Van der Veen. Fracture mechanics approach to penetration of bottom crevasses on glaciers. *Cold Regions Science and Technology*, 27(3):213–223, 1998.

[149] C.J. Van der Veen. Crevasses on glaciers. *Polar Geography*, 23(3):213–245, 1999.

[150] S. Jimenez and R. Duddu. On the evaluation of the stress intensity factor in calving models using linear elastic fracture mechanics. *Journal of Glaciology*, 64(247):759–770, 2018.

[151] A. Pralong and M. Funk. Dynamic damage model of crevasse opening and application to glacier calving. *Journal of Geophysical Research: Solid Earth*, 110(B1), 2005.

[152] R. Duddu and H. Waisman. A temperature dependent creep damage model for polycrystalline ice. *Mechanics of Materials*, 46:23–41, 2012.

[153] C.P. Borstad, A. Khazendar, E. Larour, M. Morlighem, E. Rignot, M.P. Schodlok, and H. Seroussi. A damage mechanics assessment of the Larsen B ice shelf prior

to collapse: Toward a physically-based calving law. *Geophysical Research Letters*, 39(18), 2012.

[154] R. Duddu, J.N. Bassis, and H. Waisman. A numerical investigation of surface crevasse propagation in glaciers using nonlocal continuum damage mechanics. *Geophysical Research Letters*, 40(12):3064–3068, 2013.

[155] S. Jiménez, R. Duddu, and J. Bassis. An updated-lagrangian damage mechanics formulation for modeling the creeping flow and fracture of ice sheets. *Computer Methods in Applied Mechanics and Engineering*, 313:406–432, 2017.

[156] C.P. Borstad and D.M. McClung. Numerical modeling of tensile fracture initiation and propagation in snow slabs using nonlocal damage mechanics. *Cold Regions Science and Technology*, 69(2-3):145–155, 2011.

[157] C.P. Borstad and D.M. McClung. A higher-order method for determining quasi-brittle tensile fracture parameters governing the release of slab avalanches and a new tool for in situ indexing. *Journal of Geophysical Research: Earth Surface*, 118(2):900–912, 2013.

[158] R.C.A. Hindmarsh. A numerical comparison of approximations to the Stokes equations used in ice sheet and glacier modeling. *Journal of Geophysical Research: Earth Surface*, 109(F1), 2004.

[159] E. Le Meur, O. Gagliardini, T. Zwinger, and J. Ruokolainen. Glacier flow modelling: a comparison of the Shallow Ice Approximation and the full-Stokes solution. *Comptes Rendus Physique*, 5(7):709–722, 2004.

[160] W. Leng, L. Ju, M. Gunzburger, S. Price, and T. Ringler. A parallel high-order accurate finite element nonlinear Stokes ice sheet model and benchmark experiments. *Journal of Geophysical Research: Earth Surface*, 117(F1), 2012.

[161] J. Worthen, G. Stadler, N. Petra, M. Gurnis, and O. Ghattas. Towards adjoint-based inversion for rheological parameters in nonlinear viscous mantle flow. *Physics of the Earth and Planetary Interiors*, 234:23–34, 2014.

[162] T. Isaac, G. Stadler, and O. Ghattas. Solution of nonlinear Stokes equations discretized by high-order finite elements on nonconforming and anisotropic meshes, with application to ice sheet dynamics. *SIAM Journal on Scientific Computing*, 37(6):B804–B833, 2015.

[163] R.A. Schapery. Thermoviscoelastic constitutive equations for polycrystalline ice. *Journal of cold regions engineering*, 11(2):146–157, 1997.

[164] E.S. LeClair, R.A. Schapery, and J.P. Dempsey. A broad-spectrum constitutive modeling technique applied to saline ice. *International Journal of Fracture*, 97(1-4):209, 1999.

[165] J. Åström, T. Riikilä, T. Tallinen, T. Zwinger, D. Benn, J.C. Moore, and J. Timonen. A particle based simulation model for glacier dynamics. *Cryosphere*, 7, 2013.

[166] J.N. Bassis and S. Jacobs. Diverse calving patterns linked to glacier geometry. *Nature Geoscience*, 6(10):833–836, 2013.

[167] M. Shazly, V. Prakash, and B.A. Lerch. High strain-rate behavior of ice under uniaxial compression. *International Journal of Solids and Structures*, 46(6):1499–1515, 2009.

[168] J. Pernas-Sánchez, D.A. Pedroche, D. Varas, J. López-Puente, and R. Zaera. Numerical modeling of ice behavior under high velocity impacts. *International Journal of Solids and Structures*, 49(14):1919–1927, 2012.

[169] S. Zhang, O. El Kerdi, R.A. Khurram, and W.G. Habashi. Fem analysis of in-flight ice break-up. *Finite Elements in Analysis and Design*, 57:55–66, 2012.

[170] B. Yang, G. Zhang, Z. Huang, Z. Sun, and Z. Zong. Numerical simulation of the ice resistance in pack ice conditions. *International Journal of Computational Methods*, 17(01):1844005, 2020.

[171] V. Emetc, P. Tregoning, M. Morlighem, C. Borstad, M. Sambridge, et al. A statistical fracture model for antarctic ice shelves and glaciers. *The Cryosphere*, 12:3187–3213, 2018.

[172] M.E. Mobasher, R. Duddu, J.N. Bassis, and H. Waisman. Modeling hydraulic fracture of glaciers using continuum damage mechanics. *Journal of Glaciology*, 62(234):794–804, 2016.

[173] R. Duddu, S. Jiménez, and J. Bassis. A non-local continuum poro-damage mechanics model for hydrofracturing of surface crevasses in grounded glaciers. *Journal of Glaciology*, 66(257):415–429, 2020.

[174] T.J. Boone and A.R. Ingraffea. A numerical procedure for simulation of hydraulically-driven fracture propagation in poroelastic media. *International Journal for Numerical and Analytical Methods in Geomechanics*, 14(1):27–47, 1990.

[175] Z. Chen, A.P. Bunger, X. Zhang, and R.G. Jeffrey. Cohesive zone finite element-based modeling of hydraulic fractures. *Acta Mechanica Solida Sinica*, 22(5):443–452, 2009.

[176] J. M. Segura and I. Carol. Coupled hm analysis using zero-thickness interface elements with double nodes. Part I: Theoretical model. *International Journal for Numerical and Analytical Methods in Geomechanics*, 32(18):2083–2101, 2008.

[177] B. Carrier and S. Granet. Numerical modeling of hydraulic fracture problem in permeable medium using cohesive zone model. *Engineering Fracture Mechanics*, 79:312–328, 2012.

[178] M.C. Lobao, R. Eve, D.R.J. Owen, and E. A. de Souza Neto. Modelling of hydrofracture flow in porous media. *Engineering Computations*, 2010.

[179] E. Sarris and P. Papanastasiou. The influence of the cohesive process zone in hydraulic fracturing modelling. *International Journal of Fracture*, 167(1):33–45, 2011.

[180] M.E. Mobasher, L. Berger-Vergiat, and H. Waisman. Non-local formulation for transport and damage in porous media. *Computer Methods in Applied Mechanics and Engineering*, 324:654–688, 2017.

[181] M.A. Biot. Theory of elasticity and consolidation for a porous anisotropic solid. *Journal of Applied Physics*, 26(2):182–185, 1955.

[182] J. Christmann, C. Plate, R. Müller, and A. Humbert. Viscous and viscoelastic stress states at the calving front of Antarctic ice shelves. *Annals of Glaciology*, 57(73):10–18, 2016.

[183] K.M. Cuffey and W.S.B. Paterson. *The physics of glaciers*. Academic Press, 2010.

[184] N.K. Sinha. Rheology of columnar-grained ice. *Experimental Mechanics*, 18(12):464–470, 1978.

[185] D.G. Karr and K. Choi. A three-dimensional constitutive damage model for polycrystalline ice. *Mechanics of Materials*, 8(1):55–66, 1989.

[186] W.S.B. Paterson. *Physics of glaciers*. Butterworth-Heinemann, 1994.

[187] A. Hillerborg, M. Modéer, and P.E. Petersson. Analysis of crack formation and crack growth in concrete by means of fracture mechanics and finite elements. *Cement and Concrete Research*, 6(6):773–781, 1976.

[188] A.J. Gow and T.C. Williamson. Linear compressibility of ice. *Journal of Geophysical Research*, 77(32):6348–6352, 1972.

[189] D.R. MacAyeal. Large-scale ice flow over a viscous basal sediment: Theory and application to ice stream B, Antarctica. *Journal of Geophysical Research: Solid Earth*, 94(B4):4071–4087, 1989.

[190] B.P. Lipovsky. Ice shelf rift propagation: stability, three-dimensional effects, and the role of marginal weakening. *The Cryosphere*, 14(5):1673–1683, 2020.

[191] L.M. Cathles. *Viscosity of the Earth's Mantle*. Princeton University Press, 2015.

[192] K. Hutter. *Theoretical glaciology: material science of ice and the mechanics of glaciers and ice sheets*, volume 1. Springer, 2017.

[193] J.J. Petrovic. Review mechanical properties of ice and snow. *Journal of Materials Science*, 38(1):1–6, 2003.

[194] D.G. Vaughan. Relating the occurrence of crevasses to surface strain rates. *Journal of Glaciology*, 39(132):255–266, 1993.

[195] A.C. Ugural. *Plates and shells: theory and analysis*. CRC Press, 2017.

[196] M.A. Rist, P.R. Sammonds, H. Oerter, and C.S.M. Doake. Fracture of Antarctic shelf ice. *Journal of Geophysical Research: Solid Earth*, 107(B1):ECV–2, 2002.

[197] L. Ultee, C. Meyer, and B. Minchew. Tensile strength of glacial ice deduced from observations of the 2015 eastern Skaftá cauldron collapse, Vatnajökull ice cap, Iceland. *Journal of Glaciology*, pages 1–10, 2020.

[198] J.W. Glen. The creep of polycrystalline ice. *Proceedings of the Royal Society of London. Series A. Mathematical and Physical Sciences*, 228(1175):519–538, 1955.

[199] A.J. Gow. Relaxation of ice in deep drill cores from Antarctica. *Journal of Geophysical Research*, 76(11):2533–2541, 1971.